CAPILLARY CRYSTALLISATION FOR CRYSTAL ASSESSMENT AND FIBRE-OPTIC DEVICES.

A Thesis submitted for the degree of
Doctor of Philosophy in the
University of London

by

FARAMARZ HOSSEIN-BABAI
B.Sc., M.Sc., D.I.C.

Department of Electrical Engineering,
Imperial College of Science and Technology,
London S.W.7 2BT

March, 1978.

Capillary Crystallisation for Crystal Assessment and Fibre-Optic Devices.

By: FARAMARZ Hossein-Babai

ABSTRACT

Single crystals of organic materials have been grown within small (10-100 μm) diameter glass capillary tubes. The crystals were of sufficient length for their properties to be assessed and for their applications in fibre-optic communication systems as crystal-cored optical fibres (CCOF) to be studied.

The basic theory of light propagation in optical fibres is reviewed and a summary of the theory of anisotropic optical fibres is presented. Attention is also given to non-linear optical effects with emphasis on the utilisation of these effects in fibre-optic systems.

The preparation of crystals of the required form has presented many difficulties in the past and it has previously been possible to grow only short lengths of crystals in a defect-free condition. By studying the growth of the crystals in a specially designed heater under the microscope the mechanism of formation of many of the defects has been determined. This in turn has enabled an improved growth technique to be utilized. The results of X-ray and optical examination of the crystal products for meta-dinitrobenzene and benzil are presented.

The importance of the orientation of the crystal within the fibre is discussed in connection with its device utility and the results of an investigation for orientation control during growth are given. A technique is described which enables the growth to be initiated from a seed of desired orientation within the fibre.

The results of preliminary experiments on light propagation in crystal-cored optical fibres are presented. The propagation loss was measured and methods of cutting CCOF specimens and their connection to optical fibres were devised. Device applications in the fields of both non-linear optics and fibre-optics are discussed.

Some of the potential applications of "fibre growth" for the preparation and assessment of organic crystals are given. Finally a new method for the measurement of refractive indices and dispersion in organic solids is described. In this technique the diffraction pattern resulting from the back-scattered light from a laterally-illuminated fibre was related to the geometry and refractive indices of the fibre. Refractive indices were determined to an accuracy of 2 in 10^3 without difficulty, and it is shown that by the use of various refinements an order of magnitude improvement can be anticipated.

ACKNOWLEDGEMENTS

I would like to thank Dr. E.A.D. White for his excellent supervision and advice. My thanks are due to Dr. J. R. Cozens and Mr. R.B. Dyott who provided me with useful background knowledge of fibre-optics and for many discussions with them throughout the work from which I derived benefit.

I am also indebted to the following persons for their assistance:

Professor J.C.Anderson, for introducing me to the work,

Professor P.A.Lindsay, for making available the facilities of his optics laboratory at the Electrical Engineering Department of King's College, where the experimental work presented in Chapter 6 was carried out,

Professor D. Rogers and Dr. R. Osbon, for useful discussions and assistance in connection with X-ray studies,

Mr. J.D.C. Wood, for many helpful discussions throughout the work,

Dr. J.L. Stevenson (of Post Office Research Department), for useful discussions and advice at an early stage of the work,

Mrs. V.G. Williams for typing this thesis.

Thanks are also due to the following organisations:

The Electrical Engineering Department of King's College, for the foregoing reasons,

The Chemical Crystallography Laboratory of Imperial College, where the X-ray examinations were carried out,

The Post Office Research Establishment, for providing the zone-refined mNA and mDNB material used,

The Organic Chemistry Department of I.C. for providing all other organic materials used in this work,
The Physics Department of I.C. for the use of high power laser facilities,
The Department of Metallurgy and Materials Science at I.C. for use of spectro-photometry facilities,
The Reza Pahlavi Cultural Foundation of Iran, for financial support.

Finally, personal thanks are due to my wife for her continuous patience and encouragement.

CONTENTS

LIST OF FIGURES

Page

Page

Page

Page

Page

LIST OF TABLES

INTRODUCTION

The original objective of the work presented in this thesis was to study the crystal growth of organic optically non-linear crystals in glass capillaries of down to 10 μm diameter, for the preparation of defect-free crystal-cored optical fibres (CCOF). The preparation of CCOF had been proposed by Stevenson and Dyott (1974), and the problems involved in the process were more recently reported by Stevenson (1977). However it quickly became apparent that this method of crystal growth ("fibre growth") for the preparation and assessment of organic crystals in general was of considerable importance. Hence efforts were directed both to modify conventional property measurement methods to suit the geometry of the crystals obtained and to devise new methods.

Thus, the work can be divided into three parts:

(a) The study of the fibre growth process to identify the nature of the problems involved and to find the optimum conditions for a defect-free growth process.

(b) Experimental work concerned with the utilization of the crystals obtained as optical waveguides, to delineate promising areas for further investigation.

(c) The study of possible applications of the fibre grown crystals with respect to the characterization of organic materials in general.

The three different aspects of the work, in fact, progressed in parallel, and hence chronological presentation of the results obtained was difficult.

In the first Chapter a fundamental theory of light propagation in optical fibres is given, to provide a mathema-

tical basis for the concepts employed in Chapter 4 where fibre optic applications of fibre grown crystals are discussed. Also in this Chapter a review of the theoretical work on the propagation in anisotropic optical fibres is presented. This has been added mostly to summarise information on the new subject of CCOF, rather than for use in the following Chapters.

The second Chapter is a short introduction to non-linear optics, the contents of which have been limited to the needs of the following Chapters.

The remaining Chapters then deal with different aspects of the work, and each can be considered as being independent. In Chapter 3 fibre growth as a method of crystal growth for organic materials is studied, and the growth of void-free crystal fibres is reported. Chapters 4 and 5 deal with the applications of the crystals obtained in fibre-optics and materials preparation and assessment aspects. In these Chapters, the experimental verification of several ideas is recorded and other proposals made which are based on the recorded results. In none of the cases a complete systematic investigation has been attempted, since each aspect should in itself be the subject of relatively lengthy work both from the theoretical and experimental viewpoint.

As an example, a new method for the measurement of refractive indices of organic crystals utilizing fibre grown samples was systematically approached, to determine the practical value of the fibre grown crystals. This part of the work is the subject of Chapter 6.

Thus, in this thesis in addition to the study of capillary growth for a wide range of core diameters and applications in the field of fibre-optics, a new technique for crystal growth and property measurements on organic materials is presented, which is of general applicability and is not limited to the CCOF applications considered.

CHAPTER 1

AN INTRODUCTION TO OPTICAL COMMUNICATIONS

An optical communication system in general consists of a transmitter which emits light carrying coded information, a length of optical fibre guiding the light to a destination, and a receiver where the light is detected and the original information extracted.

In this Chapter the basic theory of light propagation in optical fibres is given and a fundamental comparison between available transmitters is made. Finally, the behaviour of light in crystal cored optical fibres is discussed.

1.1 Propagation in Optical Fibres

An axial cross-section of a step-index optical fibre is shown in Fig. 1.1. It consists of a cylindrical core with a radius and refractive index of a and n_1 respectively, surrounded by a medium (cladding) of refractive index n_2, where $n_1 > n_2$. A ray of light incident at an angle θ, the angle between the ray and the fibre axis (Fig. 1.1), will undergo successive total internal reflections and be conducted through the guide if $\theta < \theta_c$, where

$$\theta_c = \text{Arc sin } (n_1^2 - n_2^2)^{\frac{1}{2}}$$

The numerical aperture of the fibre is then defined as

$$\text{N.A.} = \sin \theta_c \qquad (1.1.1)$$

An exact knowledge of the light propagation in fibres is afforded by solution of Maxwell's equations. The boundary conditions are simplified by assuming an infinitely large cladding radius. This assumption is justified because in a well designed fibre the field intensity at the cladding-air boundary is practically zero. Also homogeneous and isotropic core and cladding will be assumed. The starting point is Maxwell's equations:

$$\nabla \times \underline{H} = \frac{\partial \underline{D}}{\partial t}$$

$$\nabla \times \underline{E} = - \frac{\partial \underline{B}}{\partial t} \qquad (1.1.2)$$

and

$\underline{D} = \varepsilon \underline{E}$ $\qquad \nabla . \underline{D} = 0$

$\underline{B} = \mu_o \underline{H}$ $\qquad \nabla . \underline{B} = 0$

Considering solutions with time and z dependence as

$$\underline{E} = \underline{E}_o (x, y) \exp.\left[i(\omega t - \beta z)\right]$$

and

$$\underline{H} = \underline{H}_o (x, y) \exp.\left[i(\omega t - \beta z)\right] ,$$

substituting in Eq. (1.1.2), and transferring the equations obtained to cylindrical co-ordinates (r, ϕ, z) results in the expressions:-

$$E_r = - \frac{i}{u^2} \left(\beta \frac{\partial E_z}{\partial r} + \omega \mu_o \frac{1}{r} \frac{\partial H_z}{\partial \phi}\right) \qquad (1.1.3)$$

$$E_\phi = - \frac{i}{u^2} \left(\beta \frac{1}{r} \frac{\partial E_z}{\partial \phi} - \omega \mu_o \frac{\partial H_z}{\partial r}\right) \qquad (1.1.4)$$

$$H_r = - \frac{i}{u^2} \left(\beta \frac{\partial H_z}{\partial r} - \omega \varepsilon \frac{1}{r} \frac{\partial E_z}{\partial \phi}\right) \qquad (1.1.5)$$

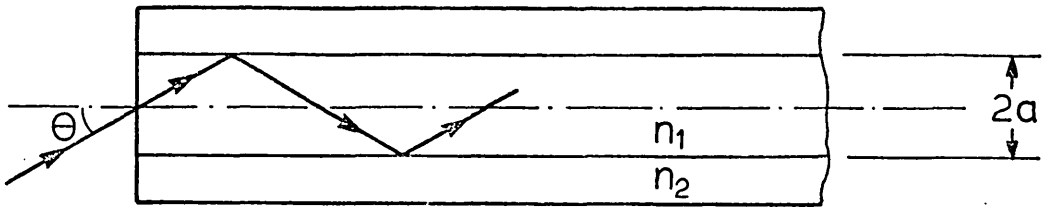

Fig. 1.1. Axial cross-section of a step-index optical fibre.

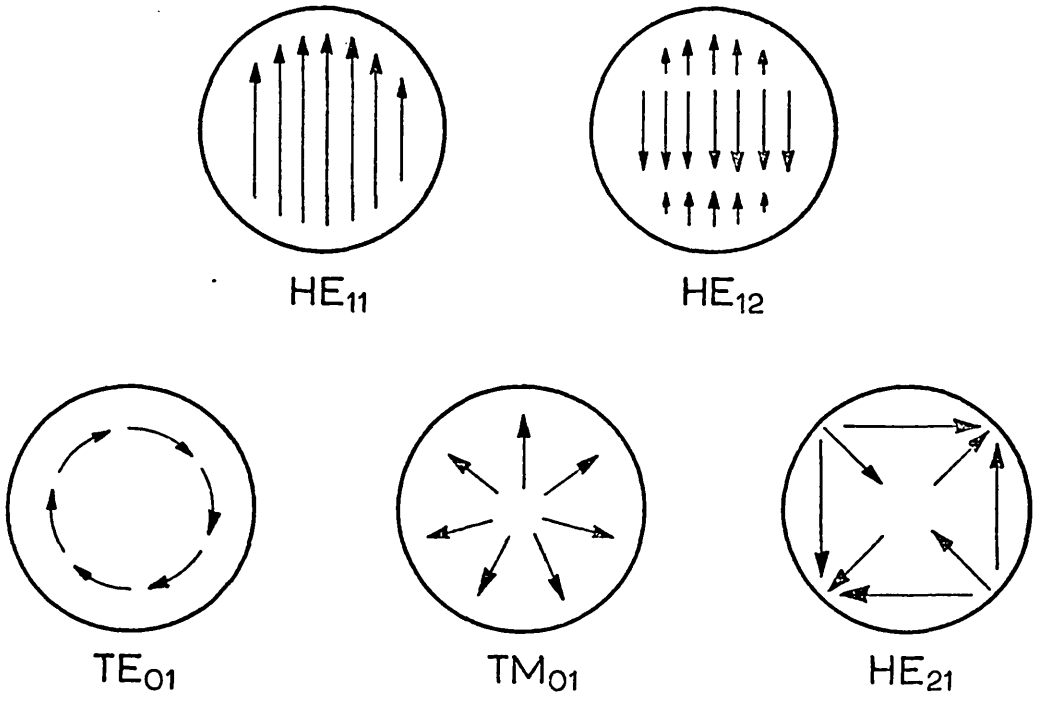

Fig. 1.2. The transverse electric field pattern for several guided modes.

$$H_\phi = - \frac{i}{u^2} \left(\beta \frac{1}{r} \frac{\partial H_z}{\partial \phi} + \omega\varepsilon \frac{\partial E_z}{\partial r}\right) \qquad (1.1.6)$$

and

$$\frac{\partial^2 E_z}{\partial r^2} + \frac{1}{r}\frac{\partial E_z}{\partial r} + \frac{1}{r^2}\frac{\partial^2 E_z}{\partial \phi^2} + u^2 E_z = 0 \qquad (1.1.7)$$

$$\frac{\partial^2 H_z}{\partial r^2} + \frac{1}{r}\frac{\partial H_z}{\partial r} + \frac{1}{r^2}\frac{\partial^2 H_z}{\partial \phi^2} + u^2 H_z = 0 \qquad (1.1.8)$$

where

$$u^2 = \omega^2 \varepsilon\mu - \beta^2 \qquad (1.1.9)$$

Substituting a trial solution as $E_z = AF(r)e^{-i\nu\phi}\, e^{i(\omega t - \beta z)}$, where ν is an integer to ensure that $E_z(r, \phi) = E_z(r, \phi + 2\Pi)$, into Eq. (1.1.7) leads to:

$$\frac{d^2F(r)}{dr^2} + \frac{1}{r}\frac{dF(r)}{dr} + \left(u^2 - \frac{\nu^2}{r^2}\right) F(r) = 0 \qquad (1.1.10)$$

Considering the physical nature of the problem, the acceptable solutions of Eq. (1.1.10) within the core ($r < a$, $\varepsilon = \varepsilon_1$) (see for example, Marcuse, 1972), are

$$E_z = A\, J_\nu(kr) e^{i\nu\phi} \qquad (1.1.11)$$

where J_ν indicates a Bessel function of νth rank and

$$k = \omega^2 \varepsilon_1 \mu_o - \beta^2 \qquad (1.1.12)$$

In a similar way H_z for $r < a$ follows as

$$H_z = B\, J_\nu(kr) e^{i\nu\phi} \qquad (1.1.13)$$

Then other field components are obtained from Eqs. (1.1.3) - (1.1.6)

$$E_r = -\frac{i}{k^2}\left[\beta k\, A\, J_\nu'(kr) + i\omega\mu_o \frac{\nu}{r} B\, J_\nu(kr)\right] e^{i\nu\phi} \qquad (1.1.14)$$

$$E_\phi = -\frac{i}{k^2}\left[i\beta \frac{\nu}{r} A\, J_\nu(kr) - k\omega\mu_o\, BJ_\nu'(kr)\right] e^{i\nu\phi} \qquad (1.1.15)$$

$$H_r = -\frac{i}{k^2}\left[-i\omega\varepsilon_1 \frac{\nu}{r} A\, J_\nu(kr) + k\beta B\, J_\nu'(kr)\right] e^{i\nu\phi} \qquad (1.1.16)$$

$$H_\phi = -\frac{i}{k^2}\left[k\omega\varepsilon_1\, A\, J_\nu'(kr) + i\beta\frac{\nu}{r} B\, J_\nu(kr)\right] e^{i\nu\phi} \qquad (1.1.17)$$

The prime indicates differentiation with respect to the argument; A and B are constants.

Solutions of Eq. (1.1.10) acceptable for $r > a$ are

$$E_z = C\, H_\nu(i\gamma r) e^{i\nu\phi} \qquad (1.1.18)$$

$$H_z = D\, H_\nu(i\gamma r) e^{i\nu\phi} \qquad (1.1.19)$$

where H_ν indicates a first kind Hankel function of νth rank and

$$\gamma^2 = \beta^2 - \omega^2\varepsilon_2\mu_o \qquad (1.1.20)$$

For other field components Eqs. (1.1.3)-(1.1.6) result in

$$E_r = -\frac{1}{\gamma^2}\left[\beta\gamma C\, H_\nu'(i\gamma r) + \omega\mu_o \frac{\nu}{r} D\, H_\nu(i\gamma r)\right] e^{i\nu\phi} \qquad (1.1.21)$$

$$E_\phi = -\frac{1}{\gamma 2}\left[\beta \frac{\nu}{r} C\, H_\nu(i\gamma r) - \gamma\omega\mu_o\, D\, H_\nu'(i\gamma r)\right] e^{i\nu\phi} \qquad (1.1.22)$$

$$H_r = -\frac{1}{\gamma^2}\left[-\omega\varepsilon_2 \frac{\nu}{r} C H_\nu (i\gamma r) + \gamma\beta D H_\nu' (i\gamma r)\right] e^{i\nu\phi} \quad (1.1.23)$$

$$H_\phi = -\frac{1}{\gamma^2}\left[\gamma\omega\varepsilon_2 C H_\nu'(i\gamma r) + \beta\frac{\nu}{r} D H_\nu (i\gamma r)\right] e^{i\nu\phi} \quad (1.1.24)$$

Again a prime indicates differentiation with respect to the argument, and C and D are constants.

The tangential components of both $\underline{E}$ and $\underline{H}$ must remain continuous at the core-cladding boundary. Equating these components (E_z, E_ϕ, H_z and H_ϕ) of the two sides of the boundary at r = a gives rise to a system of four homogeneous simultaneous equations. Thus three of the four constants present (A, B, C and D) can be determined in terms of the fourth, which remains, as expected, to be determined by the amount of power launched into the guide. However a system of homogeneous equations has meaningful solutions only if its determinant vanishes. Equating the determinant of the above-mentioned set of equations to zero provides a fifth equation which, after some tedious algebra, reduces to

$$\left(\frac{\varepsilon_1}{\varepsilon_2}\frac{a\gamma^2}{k}\frac{J_\nu'(ka)}{J_\nu(ka)} + i\gamma a\frac{H_\nu'(i\gamma a)}{H_\nu(i\gamma a)}\right)\left(\frac{a\gamma^2}{k}\frac{J_\nu'(ka)}{J_\nu(ka)} + i\gamma a\frac{H_\nu'(i\gamma a)}{H_\nu(i\gamma a)}\right)$$

$$= \left[\nu\left(\frac{\varepsilon_1}{\varepsilon_2} - 1\right)\frac{\beta\omega\sqrt{\varepsilon_2\mu_o}}{k^2}\right]^2 \quad (1.1.25)$$

Eq. (1.1.25) is called the characteristic or eigenvalue equation of the guide, by solution of which the last unknown parameter, β, in the field equations (Eqs. 1.1.11-24) is provided. Thus, through the procedure described in this section legitimate solutions of Maxwell's equations satisfying all the boundary

conditions imposed by a step-index optical fibre can be obtained.

1.2 Guided Modes

The term "mode" is defined by Marcuse (1972) as "an eigensolution of Maxwell's equations belonging to a particular eigenvalue and satisfying all the boundary conditions of the problem". Here, values of β allowed, i.e. the eigenvalues of the problem, are obtained from the solution of the characteristic equation (1.1.25) for a fibre of known parameters

$$(n_1 = \sqrt{\frac{\varepsilon_1}{\varepsilon_o}},\ n_2 = \sqrt{\frac{\varepsilon_2}{\varepsilon_o}} \text{ and } a).$$

Eqs. (1.1.11)-(1.1.24) and boundary conditions, then, provide the field components related to each β value, which are legitimate solutions of Maxwell's equations for the fibre concerned. The fields related to a β value is called a mode.

Being concerned with guided modes, i.e. those in which the power carried is somehow bound to the fibre, γ must be real. If this were not so, the magnitude of the related fields outside the core would increase exponentially with r (see Eqs. (1.1.18) - (1.1.24), having in mind that $H(x) \to e^x$ for large values of x). k also must be real in order to have oscillatory solutions inside the core. Hence regarding Eqs. (1.1.12) and (1.1.20), for a guided mode

$$\omega \sqrt{\mu_o \varepsilon_2} < \beta < \omega \sqrt{\mu_o \varepsilon_1} \qquad \text{or}$$

$$n_2\, \omega \sqrt{\mu_o \varepsilon_o} < \beta < n_1\, \omega \sqrt{\mu_o \varepsilon_o} \qquad (1.2.1)$$

Due to the oscillatory nature of Besell functions, for each value of ν there are n_ν solutions of the characteristic equation which satisfy conditions imposed by (1.2.1). For $\nu = 0$, the right hand side of Eq. (1.1.25) vanishes and setting the two left hand brackets equal to zero results in two different sets of modes. It is easy to show (Marcuse 1972) that for these modes either E_z or H_z vanishes. Thus they are called TE (transverse electric) and TH (transverse magnetic) modes respectively. Furthermore, modes are identified with subscripts ν and m where m indicates that the mode corresponds to the mth solution of the characteristic equation.

For $\nu \neq 0$ the characteristic equation, has a non-zero right hand side. This results in hybrid modes, which have non-zero values of E_z and H_z. These are designated as $HE_{\nu m}$ or $EH_{\nu m}$ modes depending on whether H_z or E_z is the dominant transverse field (Keck, 1976).

It follows from Eqs. (1.1.11) - (1.1.24) that the field patterns related to TE_{om} and TH_{om} modes are axially symmetric (no rotational dependence about the direction of propagation). Modes corresponding to larger values of m have larger numbers of radial maxima. $HE_{\nu m}$ and $EH_{\nu m}$, however, are angular dependent. ν is an indication of their angular dependence and m again is related to the number of radial maxima. The transverse electric field patterns for several guided modes are shown in Fig. 1.2.

For each mode supported in a fibre, there is a certain wavelength (cut off wavelength) at which $\beta = \omega\sqrt{\varepsilon_2\mu_o}$, resulting in $\gamma = 0$ (see Eq. (1.1.20)). The mode will cease to exist at longer wavelengths since the corresponding β will violate the condition (1.2.1). A similar argument can be made when

the wavelength is assumed constant and the fibre parameters (n_1, n_2 and a) vary. Such information on the behaviour of the modes can be obtained from Fig. 1.3, where normalized values of β, (n_{ef}), for several modes are plotted against the normalized wavelength and fibre parameters (V). n_{ef} and V are defined as

$$n_{ef} = \frac{\beta}{\omega\sqrt{\mu_o \varepsilon_o}} \qquad (1.2.2)$$

$$V = \frac{2\Pi a}{\lambda}\sqrt{n_1^2 - n_2^2} \qquad (1.2.3)$$

The cut off V value for each mode is obtained from the intersection point of the corresponding n_{ef} vs. V curve with the $n_{ef} = n_2$ line. As shown in Fig. 1.3, there is only one mode (HE_{11}) which has no cut off. It is also apparent that in a fibre of $V < 2.405$ only the HE_{11} mode can propagate. Such a fibre is called a single mode fibre. Fibres having larger V values can support many modes and are called multimode fibres. The number of modes which can be supported by a multimode fibre in principle can be obtained by counting the acceptable solutions of the characteristic equation of the fibre. However for fibres of large V values and $n_1 - n_2 \ll 1$ (this assumption is further discussed below) a good estimate of the number of modes has been shown by Gloge (1971) to be

$$N = \frac{V^2}{2}$$

Some useful information about the guided modes supported by a given fibre, such as their number, β values, phase velocities (ω/β) and group velocities ($d\omega/d\beta$), can readily be

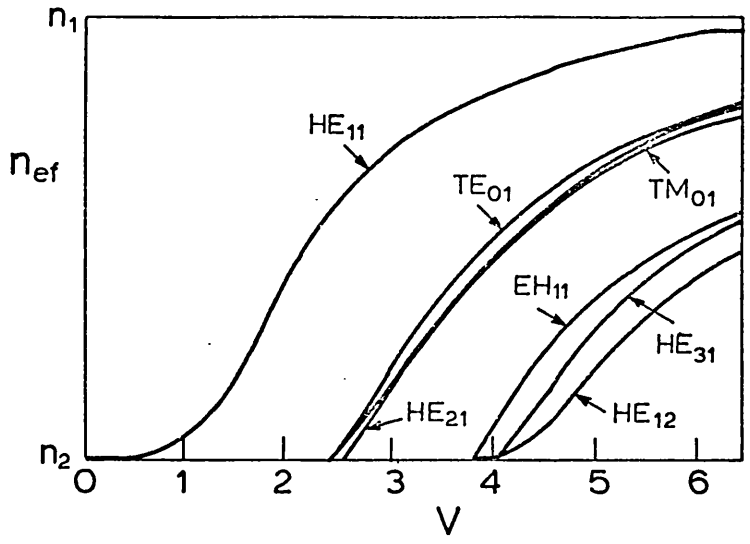

Fig. 1.3. Plots of n_{ef} Vs.V for several guided modes.

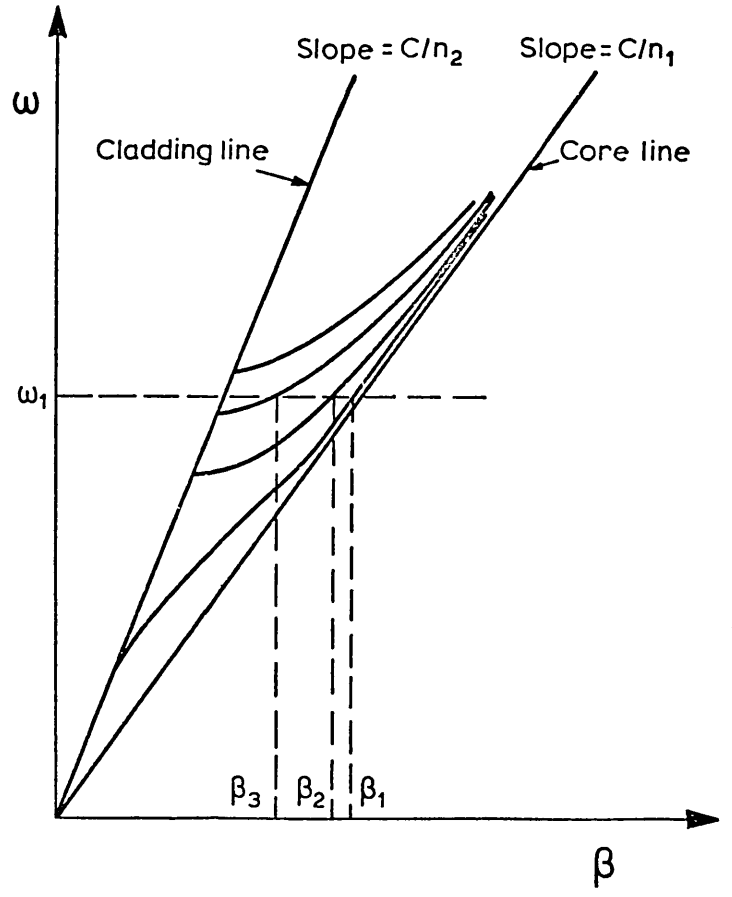

Fig. 1.4. ω-β diagram.

obtained from the ω - β diagram of the fibre (Fig. 1.4). For a fibre of given n_1, n_2 and a values the ω-β diagram is obtained numerically from its characteristic equation (1.1.25). It is important to note that for a realistic optical fibre the core and cladding lines (see Fig. 1.4) in the ω-β diagram are too close to each other to permit precise delineation so that a quantitative study is usually made from the corresponding numerical tables.

The exact modal descriptions, presented in the previous section, are mathematically complex, especially because each mode has six field components. By assuming $n_1 - n_2 << 1$ (weakly guid ing assumption) (Snyder, 1969), which is valid for all practical optical fibres, propagation in the fibre can be described by different modes, the field equations of which are much simpler. Another important feature of the new modes obtained is the fact that their transversal fields are linearly polarized (hence each mode has only 4 field components) and accordingly they are designated $LP_{\nu\mu}$, (Marcuse, 1974) where ν and μ have the same meanings as the subscripts used for labelling the previously described modes.

1.3 Radiation modes

Unlike metal waveguides which can only support a finite number of guided modes, optical fibres in addition support a continuum of unguided radiation modes. These modes are also solutions of Maxwell's equations and satisfy the boundary conditions imposed by the structure of the fibre. Light

coupled to these modes will be radiated out. This behaviour, as discussed later in this Chapter, is one of the important loss mechanisms present in optical fibres.

The mathematical analysis of radiation modes (Marcuse, 1974) is complicated and outside the scope of this work.

The propagation constants (β's) of radiation modes, unlike guided modes, provide a continuous spectrum from zero to $\omega\sqrt{\mu_o\varepsilon_2}$. The spectrum, hence, covers the area between the cladding and the $\beta = 0$ lines on the ω-β diagram (see Fig. 1.4).

1.4 Mode Coupling

Each of the guided modes of an ideal multimode waveguide (Fig. 1.1) can be excited individually (Kapany, 1967). An excited mode would propagate through the fibre and carry the total amount of the power launched for long distances if the fibre was perfect. However no perfect waveguide exists, and due to the imperfections present, modes couple to each other and exchange power. Owing to this effect, the amplitude of a mode varies as it travels through the waveguide. The rate of the change in amplitude with distance (with z) for the μth mode of a weakly guiding fibre is given by (Marcuse, 1974):

$$\frac{dC_\mu}{dz} = \sum_\nu \left\{ K_{\mu\nu}\, C_\nu \exp\left[i\,(\beta_\mu - \beta_\nu) z \right] \right\} \qquad (1.4.1)$$

where $K_{\mu\nu}$ is the coupling coefficient between μth and νth modes and C_μ and C_ν are their respective amplitudes. In Eq. (1.4.1) the effect of coupling to the modes travelling in the -z direction is neglected. Only one subscript is used

for the identification of each mode, which is a shorthand notation for the total number of characters needed to label that mode.

The coupling coefficient ($K_{\mu\nu}$) depends on the nature of the departure of the guide from ideality. For example when the core-cladding boundary varies as (Fig.1.5):

$$r(x,y,z) = a + f(z)\ \mathrm{Cos}\ \ (m\phi + \psi) \tag{1.4.2}$$

the coupling coefficient is given by (Marcuse, 1974):

$$K_{\mu\nu} = \hat{K}_{\mu\nu} f(z) \tag{1.4.3}$$

where

$$\hat{K}_{\mu\nu} \sim (n_1^2 - n_2^2) \int_0^{2\Pi} \mathcal{E}_{\mu t} \cdot \mathcal{E}_{\nu t} \cos(m\phi+\psi)\, d\phi \tag{1.4.4}$$

and $\mathcal{E}_{\mu t}$ and $\mathcal{E}_{\nu t}$ are the transverse electric fields of the μth and νth mode respectively. In arriving at Eq. (1.4.3), the longitudinal field components of the modes ($\mathcal{E}_z$) are assumed to be much smaller than the transverse components. In fact it has been shown (Marcuse, 1974) that in a weakly guiding fibre,

$$\frac{\mathcal{E}_z}{\mathcal{E}_t} \simeq \frac{(n_{ef}^2 - n_2^2)^{\frac{1}{2}}}{n_{ef}} << 1, \tag{1.4.5}$$

where n_{ef} is as defined by Eq. (1.2.2). If only the νth mode was originally excited in the disturbed guide shown in Fig. 1.5, the μth mode would gradually build up owing to the coupling. In a weak coupling case, where C_ν remains nearly

constant along the length of the fibre to be considered (L), the rate of build up follows from Eq. (1.4.1)

$$\frac{dC_\mu}{dz} = K_{\mu\nu}\, C_\nu \exp\left[i(\beta_\mu - \beta_\nu)z\right] \qquad (1.4.6)$$

Integrating both sides from zero to L,

$$C_\mu(L) = C_\nu \int_0^L K_{\mu\nu}(z) \exp\left[i(\beta_\mu - \beta_\nu)z\right] dz \qquad (1.4.7)$$

and substituting for $K_{\mu\nu}$ from Eqs. (1.4.3) and (1.4.4) results in:

$$C_\mu(L) = C_\nu F(\beta_\nu - \beta_\mu)\hat{K}_{\mu\nu} \qquad (1.4.8)$$

where

$$F(\beta_\nu - \beta_\mu) = \int_0^L f(z) \exp\left[i(\beta_\nu - \beta_\mu)z\right] dz \qquad (1.4.9)$$

$F(\beta_\nu - \beta_\mu)$ is, in fact the Fourier component of f(z) at $\beta_\nu - \beta_\mu$. It immediately follows from Eq. (1.4.8) that two modes will couple together only if the longitudinal disturbance (f(z)) has a Fourier component at $\beta_\nu - \beta_\mu$.

For a fibre in which the refractive indices depart from their ideal values the coupling coefficient is given by (Marcuse, 1974):

$$K_{\mu\nu} \sim \int_{-\infty}^{\infty}\int_{-\infty}^{\infty} (n^2 - n_o^2)\, \mathcal{E}_{\mu t} \cdot \mathcal{E}_{\nu t}\, dxdy \qquad (1.4.10)$$

where n_o (x, y) and n (x, y, z) are the refractive index

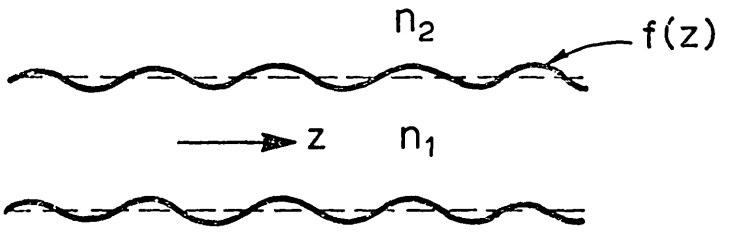

Fig. 1.5. An axial cross-section of a fibre with disturbed core–cladding boundary; dashed lines show the ideal boundary.

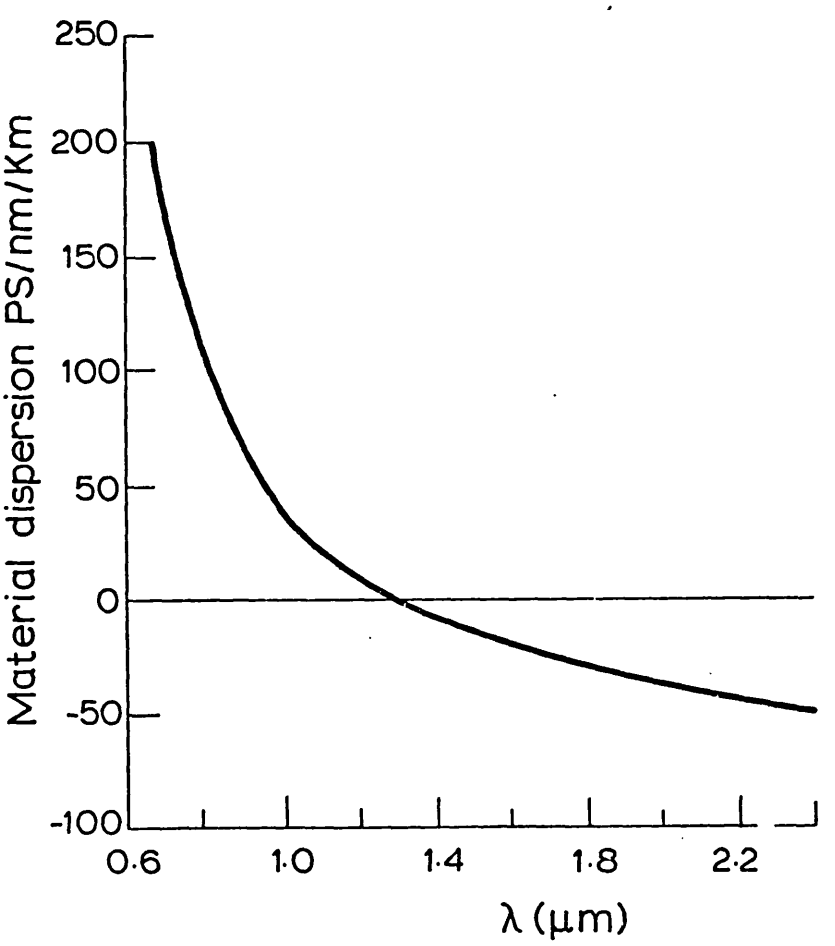

Fig. 1.6. Graph showing the variation of material dispersion with wavelength in a silica fibre.

distributions in the ideal and disturbed guides respectively. In fact, the departure of core-cladding boundary from ideal conditions, discussed earlier in this section is a special case of the latter.

Eq. (1.4.1) is also valid for the radiation modes and only the summation sign must be replaced with an integration over the continuum of radiation modes.

In a real optical fibre the existance of random disturbances in and around the fibre is unavoidable. Such disturbances, which usually have a broad spatial spectrum, will couple a guided mode both to the other guided modes and to the radiation modes supported by the fibre. The coupling of guided modes to each other not only is not harmful (at least for the present conventional applications) but also decreases the multimode dispersion (discussed later in this Chapter) of the fibre. However, the power coupled to radiation modes is lost, increasing the total attenuation of the waveguide.

1.5 Dispersion Mechanisms in Optical Fibres

In travelling through a monomode optical fibre, rays of different wavelengths travel at slightly different velocities due to the presence of both waveguide and material dispersion. Hence, pulses of light launched into the fibre broaden as they propagate, where their broadening increases directly with the spectral width of the light (Dyott and Stern, 1971). This causes overlap between two neighbouring pulses and the detector at the other end of the fibre can only

distinguish between them up to a certain level of overlaping, beyond which the authenticity of the information detected by the receiver is doubtful. Hence in any optical communications system pulses of light must have a certain time distance from each other. This limits the number of pulses per second and hence the amount of digital information transmitted by the system. To increase this capacity, it would seem desirable to decrease the spectral width of the light source used as much as possible. Although this idea is basically correct, even a hypothetically "pure" monochromatic light source will broaden in spectrum, due to the occurrence of information side bands, after modulation.

A "mode of light" propagating through a medium of $n = n(\lambda)$ (λ is the wavelength of light in the vacuum) has a phase velocity of

$$V_p = \frac{\omega}{\beta} = \frac{c}{n} \tag{1.5.1}$$

where c is the velocity of light in vacuum and $\beta=\beta(\lambda)$ is the propagation constant of the mode. Then

$$\frac{d\beta}{d\omega} = \frac{1}{c}\left(n + \omega\frac{dn}{d\omega}\right) \tag{1.5.2}$$

and the group velocity (see e.g., Everitt and Anner, 1956) of the mode follows:

$$V_g = \frac{d\omega}{d\beta} = \frac{c}{\omega\frac{dn}{d\omega} + n} = \frac{c}{f\frac{dn}{df} + n} \tag{1.5.3}$$

where f is the frequency of the light ($f = \omega/2\Pi$). A change

of variable from f to $\lambda = \frac{c}{f}$ results in:

$$V_g = \frac{c}{n - \lambda \frac{dn}{d\lambda}} \tag{1.5.4}$$

Differentiation of Eq. (1.5.4) with respect to λ then

$$\frac{dV_g}{d\lambda} = \frac{c\lambda \frac{d^2n}{d\lambda^2}}{(n - \lambda \frac{dn}{d\lambda})^2} \tag{1.5.5}$$

The time lag between λ and $\lambda + d\lambda$ after travelling one unit length of the medium will be

$$d\tau = \frac{1}{V_g + dV_g} - \frac{1}{V_g} = \frac{1}{V_g}\left(1 - \frac{1}{1 + \frac{dV_g}{V_g}}\right) \tag{1.5.6}$$

$$d\tau = \frac{1}{V_g}\left(1 - 1 + \frac{dV_g}{V_g}\right) = \frac{dV_g}{V_g^2} \tag{1.5.7}$$

or

$$dV_g = V_g^2 \, d\tau \tag{1.5.8}$$

Substituting Eq. (1.5.8) in Eq. (1.5.5) and using Eq. (1.5.4) for simplification, results in:

$$\frac{d\tau}{d\lambda} = -\left(\frac{\lambda}{c}\right) \frac{d^2n}{d\lambda^2} \tag{1.5.9}$$

Eq. (1.5.9) represents the material dispersion of an optical waveguide and is usually measured in ps/nm/km. Eq.(1.5.9) could also be used to estimate the waveguide dispersion of a single mode waveguide if n was replaced by n_{ef} for the HE_{11} mode of the guide (see Fig. 1.3).

The material dispersion for silica fibres has been given by Payne and Gambling (1975), and is reproduced here as Fig. 1.6. This shows that the material dispersion decreases towards longer wavelengths, intersecting the zero line at about 1.3 μm. The waveguide dispersion for the HE_{11} mode has also a similar behaviour and is equal to zero at a wavelength corresponding to the inflection point of the n_{ef} vs. V curve given in Fig. 1.3. Thus it is possible by working at about 1.3 μm and choosing the right V value, to adjust the conditions so that the two dispersions cancel each other, enhancing the information capacity of the transmission line. However, with light sources presently used in fibre optic communications (L.E.Ds and solid state injection lasers (see e.g., K ressel, 1976)) working at about 0.8 - 0.9 μm, the information capacity is limited by material dispersion which is an order of magnitude larger than the waveguide dispersion. This imposes a limit of about 2×10^8 b/s/km for the bit rate of a monomode fibre, when the light source is a GaAs L.E.D. (spectral width of 300 Å). The limit is twenty times higher when a GaAs laser (spectral width of 15 Å) is used.

In travelling through a multimode fibre, however the dominant dispersion mechanism is the one which originates from the difference in the group velocities of the various modes present. The effect can be best shown by drawing the $\omega=\omega_1$ line (ω_1 is the angular frequency of the source used) in the ω-β diagram (Fig. 1.4). The intersection of this line with each curve represents the operating point of the corresponding mode. The group velocity of each mode is equal

to the slope of the corresponding curve at the operating point and obviously varies between one mode and another. This effect limits the bit rate of the commercially available step-index multimode fibres to values of the order of 10^7 b/s/km. To overcome this shortcoming of multimode fibres, graded index fibres (Gloge and Marcatili, 1973) were developed. The refractive index of the core in these fibres changes as

$$n = n_o - \Delta n r^{\gamma} \qquad (1.5.10)$$

where r is the radial distance from the axis of the fibre, n_o is the axial refractive index and Δn and γ are positive constants. Theoretically, γ can be adjusted (at about $\gamma = 2$) so that the multimode dispersion decreases to very low levels (Olshansky and Keck, 1976). In practice, commercially available graded index fibres have a multimode dispersion-limited bit rate of 2.5×10^8 b/s/km; also laboratory samples of higher than 10^9 b/s/km are reported (Hazan and Bernard, 1977). This indicates that, to date, even the information capacity of the multimode optical fibres (as well as mono-mode ones) is limited by the material dispersion, when light sources of spectral widths larger than about 50 Å are used.

Thus it can be concluded that there is a lot to be gained by utilization of the light sources of narrower spectral widths and operating at about 1.3 μm.

1.6 Attenuation

Loss mechanisms present in optical fibres can be divided into two categories, absorption and scattering. Absorption occurs primarily due to the presence of impurities in the glass. For example, a concentration of 1 part in 10^9 of Fe^{2+} causes a peak loss of 1 dB/km in the fibre (Miller et al., 1973). This indicates the importance of purification of the starting materials used and the elegance of fabrication techniques for low loss fibres available today.

Scattering loss generally originates from the minor departures of the waveguide from its ideal configuration. This itself is either due to small scale intrinsic inhomogeneities of the material (Rayleigh scattering), or imperfections in the geometry of the guide. The latter can, in principle, be reduced to any arbitrary level by refinement of the preparative art, but the former imposes a lower limit for the loss which can only be reduced by changing to a different glass.

Rayleigh scattering (see for example, Maurer, 1974) occurs due to the frozen-in compositional fluctuations present in the material. Such fluctuations cause density and hence refractive index variations on a scale which is small compared to λ.

In Fig. 1.7 (after Hariguchi and Osanai, 1976) the dotted line represents the attenuation caused by Rayleigh scattering. The amount of scattered light (and thus the loss) is proportional to $1/\lambda^4$ and so rapidly increases towards shorter wavelengths. The solid line in Fig. 1.7 indicates the

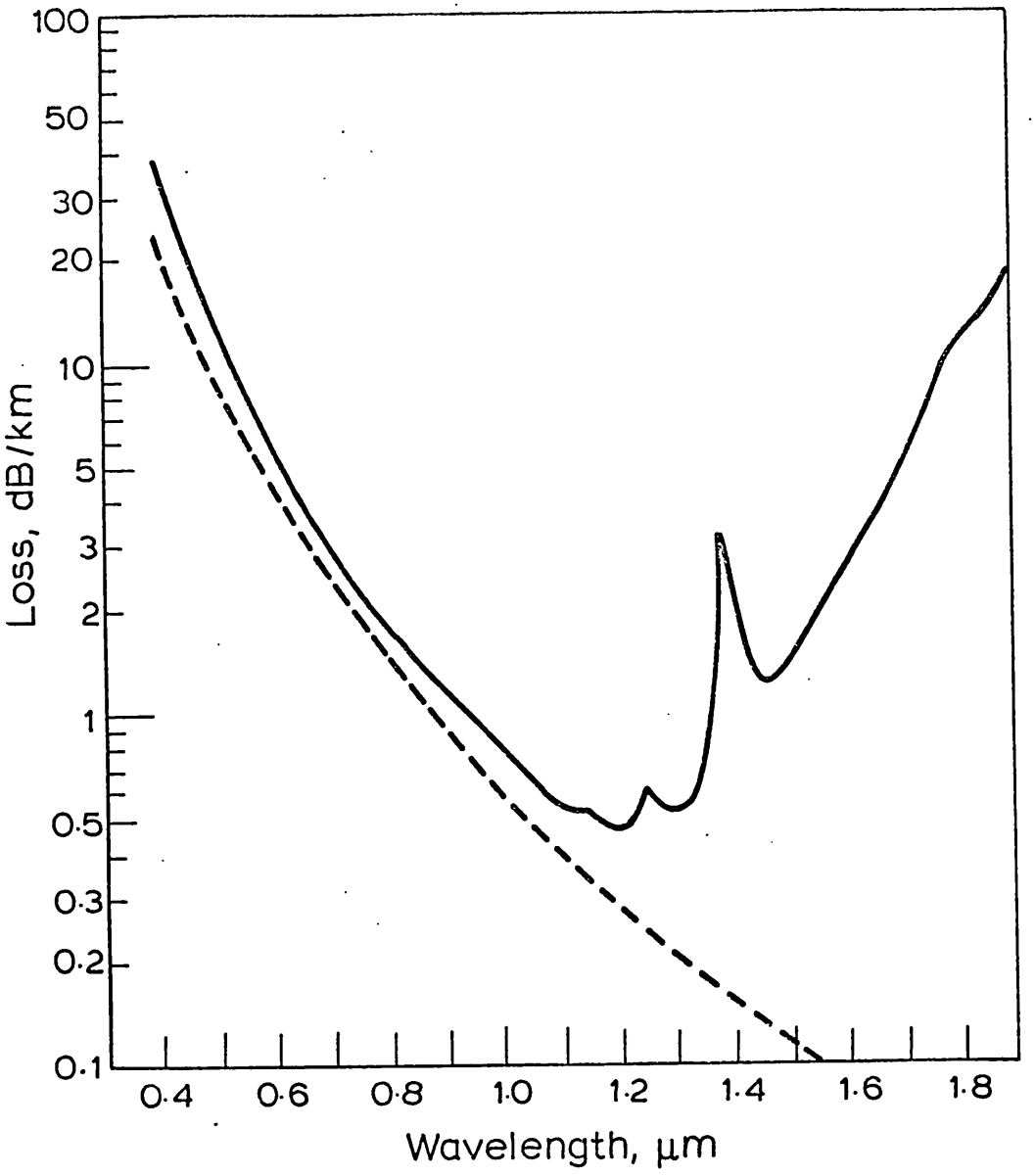

Fig. 1.7. Graph showing the variation of the total loss in an optical fibre with wavelength.

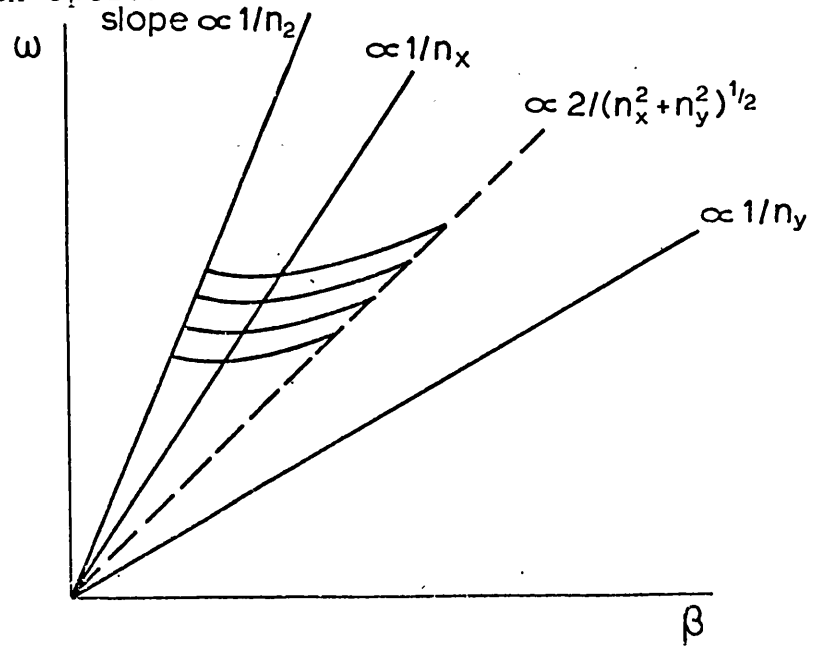

Fig. 1.8. The ω-β diagram for even modes of a biaxial crystal cored fibre.

total attenuation of the fibre as a function of λ. It is apparent that at wavelengths below 1.0 μm the attenuation is dominated by the contribution of the Rayleigh scattering indicating that it can not effectively be reduced below this level.

The total attenuation plotted in Fig. 1.7 traverses a minimum of 0.47 dB/km at about 1.3 μm. This is the lowest attenuation reported to-date (Sept. 1977).

1.7 Transmitters

The carrier generator in an optical communication system consists of a light source. It is apparent from Figs. 1.6 and 1.7 that the optimum emission wavelength for such a source is 1.2 - 1.3 μm, which is the wavelength at which zero dispersion and minimum transmission loss of the glass fortunately coincide. It is also easy to conclude from the content of Section 1.5 that spectral width of a source imposes an important limitation on its system utility. Other important technical factors to be considered when choosing a light source are:

a. Coupling efficiency between the source and the fibre.
b. Modulation technique.
c. Modulation bandwidth.
d. Linearity of the modulation characteristic.
e. Output optical power.
f. Life time.

GaAs -based laser diodes and L.E.Ds are at the moment the only sources being used in optical communication systems (see, e.g. Kressel, 1976). The wavelength range of these has

been limited to 0.75 - 0.9 μm (and 1.0 - 1.1 μm), but recently the operation of $Ga_{1-x}\ In_x\ As_{1-y}\ P_y$ electroluminescent devices in the range of 1.1 - 1.3 μm has been reported (Hsieh, 1977). Both of the mentioned sources are modulated directly, i.e. by modulation of their injection currents. Other major factors relevant to these sources are compared in Table 1.1, which indicates that laser diodes are preferred. However, an important drawback of laser diodes is their short lifetime. At present laser diodes with life times of the order of 10^3 hr. are available and considerable efforts are being made to increase this figure. It is believed that life times of the order of 10^4 - 10^5 hr. are realistic goals (Taylor, 1977).

As a potential light source for optical communication systems, major specifications of Nd:YAG laser are also quoted in Table 1.1. These indicate that, especially after demonstration of its c.w. operation at room temperature at about 1.3 μm (Burrus et al., 1976), the Nd:YAG laser is the most suitable device for the purpose mentioned. However this cannot be internally modulated and a compatible external modulator is essential for its utilization. Obvious advantages of Nd:YAG laser over electroluminescent sources put an emphasis on the importance of the search for a compatible electro-optic light modulator.

1.8 Propagation in Crystal Cored Optical Fibres (CCOF)

A CCOF is a step-index optical fibre whose core consists of a single crystal, and its cladding is made of glass. The core and the cladding are assumed to be intimately attached

TABLE 1.1. Potential Transmitters for optical communication systems

Source	LED	Semiconductor laser	Nd: YAG laser
Pump	injection current	injection current	LED (AlGaAs)
Output optical power	5 mW	~10 mW (single mode)	~2 mW (single mode)
		~50 mW (multi-mode)	~5 mW (multi-mode)
wavelength	0.75-0.9 μm	0.75-0.9 μm	1.06 μm
	(recently 1.1-1.3 μm)	(recently 1.1-1.3 μm)	(recently ~1.3 μm)
Spectral width	~300 A^o	~15 A^o	$\lesssim$ 1A^o
Coupling efficiency	$\sim n_1(n_1-n_2)$ (of the fibre used)	$\gtrsim$ 50%	~100%
modulation	internal	internal	external
modulation bandwidth	a few hundred MHz	A few GHz	that of the modulator

to each other. The making and potential applications of such a device is discussed in Chapters 3 and 4 respectively. If the crystal core were isotropic its propagation characteristics would be similar to those of glass step-index optical fibres, studied earlier in this Chapter. However, the behaviour of light on propagation through fibres of anisotropic cores would be different.

Unlike the isotropic optical waveguides which have inherited a strong background literature from the field of microwaves, little work has appeared in this field concerning propagation in anisotropic dielectric waveguides. Propagation modes of a uniaxial crystal rod were studied by Longaker and Roberts in 1963 and Rosenbaum in 1965 because of their interest in anisotropic laser cavities; and the biaxial case was studied by Cozens (1976) following the recent interest in CCOF (Stevenson and Dyott, 1974). In this Section light propagation in both uniaxial and biaxial CCOF is briefly discussed.

For a theoretical study of the problem, it is assumed that one of the principal dielectric axes of the crystal (the optic axis in the case of a uniaxial crystal) is aligned with the fibre axis (z-direction). The two other principal dielectric directions lying transversely are taken as x and y.

From Maxwell's equations (Eq. 1.1.2) it follows that

$$\nabla (\nabla . \underline{E}) - \nabla^2 \underline{E} = - \mu_o \varepsilon \frac{\partial^2 \underline{E}}{\partial t^2} \qquad (1.8.1)$$

where ε is the permittivity tensor

$$\varepsilon = \begin{vmatrix} \varepsilon_x & 0 & 0 \\ 0 & \varepsilon_z & 0 \\ 0 & 0 & \varepsilon_z \end{vmatrix} \tag{1.8.2}$$

Considering solutions with a time and z dependence as

$$\underline{E} = \underline{E}_o \exp\left[i\,(\omega t - \beta z)\right] \tag{1.8.3}$$

Eq. (1.8.1) leads to

$$\frac{\varepsilon_x}{\varepsilon_y}\frac{\partial^2 E_x}{\partial^2 x^2} + \frac{\partial^2 E_x}{\partial y^2} + (\mu_o \varepsilon_x \omega^2 - \beta^2)E_x + (1-\frac{\varepsilon_z}{\varepsilon_y})\, i\beta \frac{\partial E_z}{\partial x} = 0 \tag{1.8.4}$$

$$\frac{\partial^2 E_y}{\partial x^2} + \frac{\varepsilon_y}{\varepsilon_x}\frac{\partial^2 E_y}{\partial y^2} + (\mu_o \varepsilon_y \omega^2 - \beta^2)E_y + (1-\frac{\varepsilon_z}{\varepsilon_x})\, i\beta \frac{\partial E_z}{\partial y} = 0 \tag{1.8.5}$$

$$\frac{\partial^2 E_z}{\partial x^2} + \frac{\partial^2 E_z}{\partial y^2} + (\mu_o \varepsilon_z \omega^2 - \frac{\varepsilon_z}{\varepsilon_y}\beta^2)E_z + (1-\frac{\varepsilon_x}{\varepsilon_y})\, i\beta \frac{\partial E_x}{\partial x} = 0 \tag{1.8.6}$$

where β is the propagation constant. In a similar way the equations leading to magnetic field components are obtained:

$$\frac{\partial^2 H_x}{\partial x^2} + \frac{\partial^2 H_x}{\partial y^2} + (\mu_o \omega^2 \varepsilon_x - \frac{\varepsilon_z}{\varepsilon_y} \beta^2) H_x - (1 - \frac{\varepsilon_z}{\varepsilon_y}) i\beta \frac{\partial H_z}{\partial x} = 0 \qquad (1.8.7)$$

$$\frac{\partial^2 H_y}{\partial x^2} + \frac{\partial^2 H}{\partial y^2} + (\mu_o \omega^2 \varepsilon_z - \frac{\varepsilon_z}{\varepsilon_x} \beta^2) H_y - (1 - \frac{\varepsilon_z}{\varepsilon_x}) i\beta \frac{\partial H_z}{\partial y} = 0 \qquad (1.8.8)$$

$$\frac{\varepsilon_x}{\varepsilon_y} \frac{\partial^2 H_z}{\partial x^2} + \frac{\partial^2 H_z}{\partial y^2} + (\mu_o \omega^2 \varepsilon_z - \beta^2) H_z - (1 - \frac{\varepsilon_x}{\varepsilon_y}) i\beta \frac{\partial H_x}{\partial x} = 0 \qquad (1.8.9)$$

1.8.1 Uniaxial core

For a uniaxial crystal cored fibre, $\varepsilon_x = \varepsilon_y = \varepsilon_1 \neq \varepsilon_z$, an exact solution of the above given simultaneous equations is possible, and by a procedure similar to the one followed in Section 1.1, field components both inside and outside the core are obtained (Rosenbaum, 1965). Then applying the boundary conditions results in the characteristic equation of the guide:

$$\left(\frac{\gamma^2 a}{k_H} \frac{J_\nu'(k_H a)}{J_\nu(k_H a)} + i\gamma a \frac{H_\nu'(i\gamma a)}{H_\nu(i\gamma a)} \right) \left(\frac{(\varepsilon_1 \varepsilon_z)^{\frac{1}{2}}}{\varepsilon_2} \frac{\gamma^2 a}{k_H} \frac{J_\nu'(k_E a)}{J_\nu(k_E a)} + i\gamma a \frac{H_\nu'(i\gamma a)}{H_\nu(i\gamma a)} \right) = \left[\nu (\frac{\varepsilon_1}{\varepsilon_2} - 1) \beta \frac{\varepsilon_2 \mu_o \omega}{k_H^2} \right]^2 \qquad (1.8.10)$$

where ε_2 is the permittivity of the glass cladding,

$$k_H^2 = \mu_o \varepsilon_1 \omega^2 - \beta^2 \qquad (1.8.11)$$

and

$$k_E^2 = (\varepsilon_z/\varepsilon_1)k_H^2 \qquad (1.8.12)$$

Other symbols are as defined in Section 1.1.

Using numerical methods solutions of Eq. (1.8.10) can be obtained which are the propagation constants of the respective modes. Also a graphical method of solution has been described by Kapany and Burk (1972) which illustrates that a uniaxial CCOF, similarly to isotropic optical fibres, supports a finite number of guided modes.

When the present Chapter was being prepared another paper concerning propagation in uniaxial crystal cored fibres, by Rosenbaum and Karus (1977), appeared. In this work simplified versions of the characteristic equation and field components (E_r, E_ϕ, E_z, H_r, H_ϕ and H_z) are derived based on weakly guiding ($n_1-n_2/n_1 << 1$) and weakly anisotropic ($n_z-n_1/n_1 << 1$) approximations. This in turn has made possible the calculation of the fraction of the power carried in the core (p_c) compared to that carried in the cladding ($p_{clad.}$) for each mode. Various plots of p_c/p_c+p_{clad} vs. normalized frequency are then given for different modes in fibres of different anisotropies (n_z-n_1/n_1). These show that the behaviour of a mode in a uniaxial fibre is very much similar to the behaviour of the corresponding mode in an isotropic guide with a core index equal to the transverse index of the uniaxial CCOF. This result was expected, since as mentioned in Section 1.4, for any guided mode of a weakly guiding optical fibre the longitudinal component of the electric field is much smaller than the transverse one, and

thus the mode would approximately "see" the transverse refractive index of the guide only.

1.8.2 Biaxial Core

A biaxial CCOF ($\varepsilon_x \neq \varepsilon_y \neq \varepsilon_z$) can be considered as a perturbed uniaxial one (Cozens, 1976). Such a perturbation, unlike the one discussed as an example in section 1.4 (see Fig. 1.5) is independent of z. Kogelnik et al.(1975) have calculated the change in propagation constants of the modes when the guide is affected by a z independent small perturbation:

$$\Delta\beta = \frac{\omega}{p} \int_{-\infty}^{+\infty}\int \Delta\varepsilon \, \mathcal{E}_\nu \cdot \mathcal{E}_\nu^* \, dx \, dy \qquad (1.8.13)$$

where $\Delta\varepsilon(x, y)$ is the departure of the permittivity of the guide from its ideal value, $\mathcal{E}_\nu$ is the electric field of the mode in the ideal guide and p is the total power carried by the mode. Considering a uniaxial guide of ε_1 and ε_z as the starting ideal configuration, for a biaxial guide of ε_x, ε_y and ε_z, we have (Cozens, 1976):

$$\Delta\beta = \frac{\omega}{p} \int_0^{2\pi}\int_0^{a} (\varepsilon_x-\varepsilon_1) \, \mathcal{E}_{x\nu} \cdot \mathcal{E}_{x\nu}^* + (\varepsilon_y-\varepsilon_1) \, \mathcal{E}_{y\nu} \cdot \mathcal{E}_{y\nu}^* \, r\,dr\,d\phi \qquad (1.8.14)$$

where $\mathcal{E}_{x\nu}$ and $\mathcal{E}_{y\nu}$ are the field components of the mode in the ideal guide and ε_1 is the transverse permittivity of the uniaxial guide. Eq. (1.8.13) and thus also Eq. (1.8.14)

are valid only for the case of small perturbations, i.e.

$$\Delta\beta \ll \beta_\nu$$

where β_ν is the propagation constant of the mode in the ideal guide.

Propagation constants and dispersion characteristics of the guided modes of a biaxial CCOF can, then, numerically be calculated from Eq. (1.8.14) knowing the same information for the corresponding uniaxial one. The choice of the starting uniaxial guide is important for reducing the computational labour and precision of the result. Choosing $\varepsilon_1=(\varepsilon_x+\varepsilon_y)/2$, Eq. (1.8.14) reduces to

$$\Delta\beta = \frac{\omega}{p} \int_0^{2\Pi}\int_0^{a} (\Delta\varepsilon \; \mathcal{E}_{x\nu} \mathcal{E}^*_{x\nu} - \Delta\varepsilon \; \mathcal{E}_{y\nu} \mathcal{E}^*_{y\nu}) \; r dr d\phi \tag{1.8.15}$$

where $\Delta\varepsilon = \varepsilon_x - \varepsilon_1 = |\varepsilon_y - \varepsilon_1|$, (it is assumed that $\varepsilon_x > \varepsilon_y$).

In the case of even modes (modes corresponding to even values of ν) the symmetry of the transverse field patterns requires that

$$\int_0^{2\Pi}\int_0^{a} \mathcal{E}_{x\nu}\mathcal{E}^*_{x\nu} r dr d\phi = \int_0^{2\Pi}\int_0^{a} \mathcal{E}_{y\nu} \mathcal{E}^*_{y\nu} \; r dr d\phi$$

and hence $\Delta\beta = 0$. Thus the propagation constants of even modes in a biaxial CCOF are equal to the corresponding modes of a

uniaxial CCOF of $\varepsilon_1 = (\varepsilon_x + \varepsilon_y)/2$ and the same ε_z as the CCOF in question.

The transverse electric field of the HE_{11} mode in a weakly guiding fibre is almost linearly polarised (see Fig. 1.2.). In order to calculate the β value for HE_{11} mode of a biaxial CCOF of ε_x, ε_y and ε_z, assuming that the polarization direction is x, the starting uniaxial CCOF can be chosen so that $\varepsilon_1 = \varepsilon_x$. Thus in Eq. (1.8.14), $\varepsilon_x - \varepsilon_1$ vanishes. Also, as mentioned above, $\mathcal{E}_{y\nu} \cdot \mathcal{E}^*_{y\nu} \simeq 0$ and it follows that $\Delta\beta = 0$. If the mode considered was polarised in the y direction, for the equivalent uniaxial fibre $\varepsilon_1 = \varepsilon_y$.

There is no short cut for calculation of the propagation constants of the odd modes (modes corresponding to odd values of ν, excluding $\nu = 1$) and Eq. (1.8.14) must be numerically solved for this purpose.

Thus it can be concluded that a biaxial CCOF guide is, in fact, equivalent to a uniaxial CCOF of the same ε_z, where its ε_1 is a weighted average of ε_x and ε_y. The weighting factor is related to the field strength in the x and y directions. A qualitative ω-β diagram, based on the information presented in this Section, is given in Fig. 1.8. However, quantitative data are of prime importance for the design of fibre optic devices utilising crystal cored optical fibres. Such information has not yet been reported in the literature.

CHAPTER 2

NON-LINEAR OPTICS

2.1 Introduction

The reaction of an optically linear medium to an applied electromagnetic wave of $E(t) = E_o^{(\omega)} \cos \omega t$ is described by its polarization:

$$P(t) = \varepsilon_o \chi E(t) \qquad (2.1.1)$$

where χ is the linear suceptibility of the medium, which is also related to its refractive index through

$$n = \sqrt{\frac{\varepsilon}{\varepsilon_o}} = \sqrt{1 + \chi} \qquad (2.1.2)$$

Lorentz showed that polarization in a medium can be attributed to the oscillating dipoles present (Longhurst, 1957). In its simplest form, the model consists of a single atom with a single polarizable electron. The potential energy of the electron is given by

$$V(\dot{x}) = \frac{m}{2} \omega_o x^2 \qquad (2.1.3)$$

where

m = the electronic mass,

ω_o = the natural (resonance or absorption) frequency of the dipole, and

x = the electron's displacement from its equilibrium position.

The equation of motion ($fr = m \frac{d^2x}{dt^2}$) for such an electron has the form of

$$\frac{d^2x(t)}{dt^2} + \sigma\frac{dx(t)}{dt} + \omega_o^2 x(t) = -\frac{eE^{(\omega)}}{m} \text{Cos } \omega t \qquad (2.1.4)$$

where e is the electronic charge and $m\sigma \frac{dx(t)}{dt}$ is the frictional force present. This results in

$$x(t) = q_1 \text{ Cos } \omega t \qquad (2.1.5)$$

where

$$q_1 = \frac{-eE^{(\omega)}/m}{(\omega_o^2 - \omega^2) + i\omega\sigma}$$

The polarization of the medium is related to the displacement of electrons by:-

$$P(t) = Nex(t) \qquad (2.1.6)$$

where N is the electron density. Substituting for x(t) from Eq. (2.1.5) results in

$$P(t) = \frac{Ne^2/m}{(\omega_o^2 - \omega^2) + i\omega\sigma} E_o^{(\omega)} \text{ Cos } \omega t \qquad (2.1.7)$$

and comparing with Eq. (2.1.1), it follows that

$$\chi = \frac{Ne^2}{m\varepsilon_o(\omega_o^2 - \omega^2 + i\sigma\omega)} \qquad (2.1.8)$$

Also, using Eq. (2.1.2), the refractive index of the medium is given by

$$n = \left[1 + \frac{Ne^2}{m\varepsilon_o(\omega_o^2 - \omega^2 + i\sigma\omega)} \right]^{\frac{1}{2}} \qquad (2.1.9)$$

which successfully predicts the Sellmier dispersion of the refractive index (see e.g., Born and Wolf, 1975).

The observation of optical harmonic generation in a quarz crystal by Franken et al. (1961), started an intense study of the non-linear optical properties of materials. This was followed by the discovery of related phenomena such as sum-and-difference-frequency generation. All of these effects can be described by the nonlinearity of the polarization of the medium with respect to the applied field. Their discovery had been delayed until the advent of the laser due to the high light intensities necessary for revealing these non-linear effects. However other effects, which do not require high light intensities for their observation, but are properly classified in the area of non-linear optics, had long been known (e.g. the electro-optic or Kerr effect).

An understanding of the non-linear effects mentioned and the link between them is afforded by allowing for a small departure from linearity in the Lorentz model discussed above. Then the potential energy of the oscillating electron is generalized by introducing anharmonic terms

$$V(x) = \frac{m\omega_o^2}{2} x^2 + \frac{m}{3} Dx^3 + \frac{m}{4} Bx^4 + \ldots \qquad (2.1.10)$$

where D and B are constants. In a crystalline medium the potential energy allocated to an electron must reflect the

symmetry of the crystal (Neumann's principle; Nye, 1957). The presence of a centre of symmetry, then, requires

$$V(x) = V(-x)$$

and as a result, terms containing odd powers of x in V(x) vanish.

In a non-centrosymmetric crystal, and considering only the first two terms, the potential energy is given by

$$V(x) = \frac{m\omega_o^2}{2} x^2 + \frac{m}{3} Dx^3 \qquad (2.1.11)$$

The equation of the motion of the electron then obtains the form:

$$\frac{d^2x(t)}{dt^2} + \sigma\frac{dx(t)}{dt} + \omega_o^2 x(t) + Dx^2(t) = -\frac{eE_o^{(\omega)}}{m} \text{Cos } \omega t \qquad (2.1.12)$$

which has only an anharmonic term ($Dx^2(t)$) added to the left hand side, when compared with Eq. (2.1.4). Its solution results in:-

$$x(t) = q_1 \text{ Cos } \omega t + q_2 \text{ Cos } 2\omega t \qquad (2.1.13)$$

with q_1 as given in Eq. (2.1.5) and

$$q_2 = \frac{-De^2 \; E^{(\omega)^2}}{2m(\omega_o^2 - \omega^2 + i\omega\sigma)^2(\omega_o^2 - 4\omega^2 + 2i\sigma\omega)} \; .$$

The polarization of the medium is then obtained by substituting x(t) from Eq. (2.1.13) in Eq. (2.1.6):

$$P(t) = \varepsilon_o \chi E_o^{(\omega)} \text{ Cos } \omega t + dE_o^{(\omega)2} \text{ Cos } 2\omega t \qquad (2.1.14)$$

where χ is given by Eq. (2.1.8) and

$$d = \frac{DNe^3}{2m^2(\omega_o^2 - \omega^2 + i\omega\sigma)^2(\omega_o^2 - 4\omega^2 + 2i\omega\sigma)}$$

Eq. (2.1.14) shows that for a driving field at ω the medium obtains an additional polarization at 2ω:

$$P^{(2\omega)}(t) = P_o^{(2\omega)} \text{ Cos } 2\omega t \qquad (2.1.15)$$

and from Eq. (2.1.14)

$$P_o^{(2\omega)} = d \cdot E_o^{(\omega)^2} \qquad (2.1.16)$$

showing that the non-linear optical coefficient, d, is the ratio of the induced non-linear polarization to the square of the fundamental electric field. In reality Eq. (2.1.16) is a tensorial one, and relates the second harmonic polarization of the material in each direction (x, y and z) to the driving electric field components:

$$P_i^{(2\omega)} = d_{ijk} E_j^{(\omega)} E_k^{(\omega)} \qquad (2.1.17)$$

with i, j and k varying from 1 to 3 (1, 2 and 3 refer to the x, y and z directions, respectively); Einstein's convention is used for omitting the summation sign; this convention is employed throughout the present Chapter.

Until now, a single frequency driving field was assumed. In a more general case two alternative electric fields, with angular frequencies β and γ respectively, are applied. Through a similar procedure it can be shown that additional polarizations at sum and difference frequencies occur. Using the nomenclature due to Bloembergen (1965) the induced polarization at the angular frequence $\alpha = \beta + \gamma$ is given by:

$$P_i^{(\alpha)} = d_{ijk}^{(\alpha,\beta,\gamma)} E_j^{(\beta)} E_k^{(\gamma)} \qquad (2.1.18)$$

Then for second harmonic polarization, where $\beta = \omega$, $\gamma = \omega$ and $\alpha = 2\omega$:

$$P_i^{(2\omega)} = d_{ijk}^{(2\omega,\ \omega,\omega)} E_j^{(\omega)} E_k^{(\omega)} \quad ; \qquad (2.1.19)$$

for sum and difference frequency generation where $\beta = \omega_1$, $\gamma = \pm\omega_2$ and $\alpha = \omega_1 \pm \omega_2$:

$$P_i^{(\omega_1 \pm \omega_2)} = d_{ijk}^{(\omega_1 \pm \omega_2, \omega_1, \omega_2)} E_i^{(\omega_1)} E_k^{(\omega_2)} \qquad (2.1.20)$$

and for the electro-optic effect, where $\beta = \omega$, $\gamma = 0$ and $\alpha = \omega$:

$$P_i^{(\omega)} = d_{ijk}^{(\omega,\ \omega,\ o)} E_j^{(\omega)} E_k^{(o)} \qquad (2.1.21)$$

2.2 Second Harmonic Generation (SHG)

A study of the electromagnetic wave propagation in a non-linear medium shows that due to the induced second harmonic polarization, a second harmonic electromagentic wave will be generated. The amplitude of the generated wave increases as both waves travel through the medium, indicating that power is gradually transferred from the fundamental to the second harmonic wave. The rate of this amplitude build up, in a loss-less medium with a non-linear polarization as in Eq. (2.1.16), is given by (see, e.g. Yariv, 1976)

$$\frac{dE^{(2\omega)}(z)}{dz} = - i\omega\sqrt{\frac{\mu}{\epsilon}}\, d\left[E^{(\omega)}(z)\right]^2 e^{i(\Delta k)z} \qquad (2.2.1)$$

with

$$z = \text{direction of propagation, and}$$
$$\Delta k = k^{(2\omega)} - 2k^{(\omega)} \qquad (2.2.2)$$

where

$$k^{(\omega)} = \frac{\omega n^{(\omega)}}{c} \quad \text{and} \quad k^{(2\omega)} = \frac{2\omega n^{(2\omega)}}{c} \quad .$$

$n^{(\omega)}$ and $n^{(2\omega)}$ are the refractive indices of the medium at ω and 2ω, respectively. The amplitude of the second harmonic wave, after travelling a distance equal to ℓ in the medium, can be obtained by integrating Eq. (2.2.1) from 0 to ℓ. This integration is particularly easy when the power depletion of the fundamental wave due to SHG is negligible. In this case $E^{(\omega)}(z)$ can be assumed constant; the integration leads to

$$E^{(2\omega)}(\ell) = -i\omega\sqrt{\frac{\mu}{\varepsilon}}\; d\,[E^{(\omega)}]^2\; \frac{e^{i\Delta k \ell}-1}{i\Delta k} \quad . \qquad (2.2.3)$$

The intensities (power per unit area) of the fundamental and second harmonic waves are related to their field amplitudes by

$$I^{(2\omega)} = \frac{P^{(2\omega)}}{A} = \frac{1}{2}\sqrt{\frac{\varepsilon}{\mu}}\; |E^{(2\omega)}|^2 \qquad (2.2.4)$$

and

$$I^{(\omega)} = \frac{P^{(\omega)}}{A} = \frac{1}{2}\sqrt{\frac{\varepsilon}{\mu}}\; |E^{(\omega)}|^2 \qquad (2.2.5)$$

respectively, where $P^{(\omega)}$ and $P^{(2\omega)}$ are the total power in the fundamental and second harmonic waves respectively, and A is the cross-section of the beam. Using Eqs. (2.2.3-5) the efficiency of power conversion from ω to 2ω follows:

$$\eta_{SHG} = \frac{P^{(2\omega)}}{P^{(\omega)}} = 2\left(\frac{\mu}{\varepsilon_o}\right)^{3/2} \frac{\omega^2 d^2 \ell^2}{n^3} \frac{\sin^2(\Delta k \ell/2)}{(\Delta k\, \ell/2)^2} \frac{P^{(\omega)}}{A} \qquad (2.2.6)$$

The efficiency of SHG, then, is critically dependent on Δk. The maximum efficiency corresponds to $\Delta k = 0$, and given by

$$\eta_{SHG,m} = 2\left(\frac{\mu}{\varepsilon_o}\right)^{3/2} \frac{\omega^2 d^2 \ell^2}{n^3} \frac{P^{(\omega)}}{A} \qquad (2.2.7)$$

The SHG coefficient d was considered a scalar above, but as given by Eq. (2.1.19), it is a third rank tensor ($d_{ijk}^{2\omega,\omega,\omega}$) and has 27 elements. In Eq. (2.1.19), d_{ijk} is multiplied to $E_j^{(\omega)}\, E_k^{(\omega)}$ which is insensitive to replacement of the subscripts, and it follows that $d_{ijk} = d_{ikj}$.

This reduces the number of independent elements to 18. This number is further reduced by taking into account the symmetry of the crystalline medium. For example there is only one independent element in the SHG tensor of a crystal belonging to symmetry class $\bar{4}3$ m.

It immediately follows from (2.2.6 and 7) that for a given total power of the fundamental wave, the SHG efficiency can be increased by concentrating the power into a smaller area. Conventionally, this is done by optimum focussing of the fundamental beam within the crystal (see, Zernike and Midwinter, 1973), but this cannot be maintained for long distances and the beam gradually diverges. In a waveguide, however, it is possible to confine the condensed beam for very long lengths, which thus constitutes one of the main advantages of carrying out non-linear interactions within optical waveguides made of optically non-linear crystals.

2.2 Phase matching in SHG

It was shown in the previous section that the SHG efficiency critically depends on Δk, and for an efficient process Δk must, practically, vanish:

$$\Delta k = k^{(2\omega)} - 2k^{(\omega)} = \frac{2\omega}{c} (n^{(2\omega)} - n^{(\omega)}) = 0 \qquad (2.3.1)$$

Then phase matching ($\Delta k = 0$) would be achieved when

$$n^{(2\omega)} = n^{(\omega)} \qquad (2.3.2)$$

However, as shown before (Eq. 2.1.9), the refractive index of a medium is a function of ω and usually increases with it. Therefore, in ordinary circumstances the phase matching condition (Eq. 2.3.2) is not satisfied. This decreases the maximum effective length of the crystal for SHG, from an infinite length in the phase-matched case, to the "coherence length" (see, Zernike and Midwinter, 1973):

$$l_c = \frac{2\pi}{\Delta k} = \frac{\lambda}{2(n^{(2\omega)} - n^{(\omega)})} \qquad (2.3.3)$$

It follows from Eq. (2.2.6) that when the interaction length in the crystal increases beyond $l_c/2$ the SHG efficiency actually decreases; i.e. beyond $l_c/2$ the direction of power conversion reverses. Coherence lengths of most of the useful non-linear optical materials are of the order 10 μm. Eq. (2.2.6) clearly shows that for such interaction lengths no significant conversion efficiency can be expected. Also it follows from the same equation that if by the means of a phase matching technique the coherence length of a crystal could be increased to the order of cm, the SHG efficiency would increase by a factor of 10^6.

Various phase matching techniques have been discussed by Zernike and Midwinter (1973). In the most widely used method, namely the "angular phase matching", the natural birefringence of the crystal is employed to compensate for its refractive index dispersion. For this, the direction of

propagation within the crystal is chosen so that the two interacting waves (fundamental and second harmonic) each propagate as a different type of ray from the other (ordinary and extraordinary) and "see" equal refractive indices. The method is applicable to materials which have sufficiently strong birefringence to allow for this compensation of dispersion. Unfortunately the most suitable materials for SHG, are isotropic (e.g. GaAs) and some other have only weak birefringence (e.g. benzil; Jerphagnan, 1971) so that angular phase matching cannot be applied in these cases.

Although only phase matching for SHG was discussed here, other non-linear wave interactions, e.g. sum-and-difference-frequency generation, also require the phase matching condition in order for the interaction to be efficient. For instance the phase matching condition for the mentioned example is:

$$\Delta k = k^{(\omega_1 \pm \omega_2)} - (k^{(\omega_1)} \pm k^{(\omega_2)}) = 0$$

The phase matching techniques used are similar in principal to the case for SHG.

It was shown in Chapter 1 that different modes supported by an optical waveguide have different phase velocities. Therefore in an optical waveguide made of an optically non-linear material, phase matching of the interacting waves can be achieved by utilizing the waveguide modal dispersion to overcome the refractive index dispersion of the material. (Anderson and Boyd, 1971). Theoretical and experimental work on thin film waveguides indicate that long coherence lengths can be achieved in this way (discussed in Chapter 4). By

making crystal cored optical fibres, it is hoped that similar work can be carried out in cylindrical geometry, which would have the main advantage of optical fibre compatibility.

2.4. Electro-Optic Effect

This effect is the result of interaction of a light wave with a static electric field in a non-linear medium. The interaction is summarized by Eq. (2.1.21).

For a physical understanding of the effect, Kurtz and Robinson (1967) reconsidered the electron motion equation (Eq. 2.1.8) as

$$\frac{d^2x(t)}{dt^2} + \sigma\frac{dx(t)}{dt} + \omega_o\, x(t) + Dx^2(t) = e/m \left[E(\omega, t) + \beta E(0) \right] \qquad (2.4.1)$$

where $E(\omega, t)$ is the electric field of the light wave with radian frequency ω, $E(0)$ is the external d.c. field and β is a local field correction factor. The natural oscillation (resonant or absorption) frequency obtained for the electron from Eq. (2.4.1) is

$$\omega'^2_o = \omega_o^2 + \frac{2De\beta E(0)}{m\omega_o^2} \qquad (2.4.2)$$

The refractive index of the medium is related to ω_o through Eq. (2.1.9). When the static electric field is applied ω_o shifts to ω'_o and this alters the refractive index of the material "seen" by the light wave.

An alternative way to describe the effect is through Eq. (2.1.21). This indicates that due to the interaction of the light wave at frequency ω and the static electric field, a non-linear polarization at ω (in addition to the linear polarization at ω) is produced. A study of the wave propagation in this condition shows that another wave at ω is generated which is 90^{o} out of phase with respect to the fundamental wave. Adding the generated wave to the fundamental, alters the phase of the output, which can also be described in terms of a change in the refractive index of the medium. With this comparison the relationship between $d_{ijk}^{\omega,\omega,0}$ (Eq. 2.1.21) and r_{ijk} (defined below) can be obtained (see, Zernike and Midwinter, 1973).

The refractive index ellipsoid of a medium referred to its principal axes (x_1, x_2 and x_3) is

$$n_i^{-2} \; x_i^2 = 1 \qquad (2.4.3)$$

where i varies from 1 to 3. An applied electric field modifies the ellipsoid to become:

$$n_i^{-2} \; x_i^2 + r_{ijk} \; x_i \; x_j \; E_k = 1 \qquad (2.4.4)$$

where E_k is the component of the electric field in kth direction and r_{ijk} is a third rank tensor and has 27 elements, but as in the case of the SHG tensor, we have

$$r_{ijk} = r_{jik} \quad , \qquad (2.4.6)$$

so the following contraction of indices can be adopted, $ij \longleftrightarrow m$ with:

$$11 \longleftrightarrow 1 \quad , \quad 22 \longleftrightarrow 2 \quad , \quad 33 \longleftrightarrow 3$$
$$23 \longleftrightarrow 4 \quad , \quad 13 \longleftrightarrow 5 \quad , \quad 12 \longleftrightarrow 6$$

This reduces the elector-optic tensor to r_{mk} where m varies from 1 to 6 and k from 1 to 3, making the number of independent coefficients equal to 18. Then, by taking into account the symmetry of the crystal, as in the case of the SHG tensor, this number is further reduced. The forms of the electro-otpic tensors for all symmetry classes are given in most of the relevant text-books (see e.g. Yariv, 1976). As examples, the electro-optic tensors for the mm2 and 32 classes have the forms of

$$\begin{bmatrix} 0 & 0 & r_{13} \\ 0 & 0 & r_{23} \\ 0 & 0 & r_{33} \\ 0 & r_{42} & 0 \\ 0 & 0 & r_{51} \\ 0 & 0 & 0 \end{bmatrix} \quad \text{and} \quad \begin{bmatrix} r_{11} & 0 & 0 \\ -r_{11} & 0 & 0 \\ 0 & 0 & 0 \\ r_{41} & 0 & 0 \\ 0 & -r_{41} & 0 \\ 0 & -r_{11} & 0 \end{bmatrix} \quad \text{respectively.}$$

The linear electro-optic effect, as for SHG, originates from the existance of a third power term in the potential energy of the electrons in the model discussed. If D = 0 in Eq. (2.4.1), there would have been no shift in ω_o (see Eq. 2.4.2), and as a result, no electro-optic effect. Since D = 0 for centrosymmetric crystals, the effect only occurs in non-centrosymmetric structures.

2.5 Half-wave voltage

A beam of light passing through a bulk electro-optic crystal will undergo a retardation due to the change in the refractive index of the medium when an electric field is applied. This phase retardation, in radians, is given by

$$\Gamma = \frac{2\pi \ell}{\lambda_o} (n' - n) = \frac{2\pi 1}{\lambda_o} \Delta n \qquad (2.5.1)$$

where ℓ is the length of the light path through the crystal, λ_o is wavelength in vacuo and n' is the refractive index when the electric field is applied. Obviously Γ in a given crystal depends on both directions of light propagation and polarisation, and also depends on the direction of the applied field.

In the case of a crystal of point group mm2 (see previous Section for its electro-optic tensor), for example, when light is polarised parallel to x_1, and the electric field is applied parallel to x_3, the change in refractive index is obtained from a comparison between Eqs. (2.4.3) and (2.4.4):

$$\Delta n_1 = (n'_1 - n_1) = - \frac{n_1^3}{2} r_{13} E_3 \quad , \qquad (2.5.2)$$

and so

$$\Gamma = \frac{\pi \ell}{\lambda_o} n_1^3 \, r_{13} E_3 \qquad (2.5.3)$$

where the beam of light is also crossing the crystal parallel to x_3, $E = V/\ell$, where V is the voltage applied between the two

parallel electrodes. Then, substitution for E in Eq. (2.5.3) results in

$$\Gamma = -\frac{\Pi}{\lambda_o} n_1^3 r_{13} V. \qquad (2.5.4)$$

The voltage which would result in a phase retardation equal to Π (the half-wave voltage) is then given by

$$V_{\lambda/2} = -\frac{\lambda_o}{n_1^3 r_{13}} , \qquad (2.5.5)$$

which is a property of the crystal and can be used for its characterization.

However, when the direction of light propagation differs from the direction of the field applied, the half-wave voltage of the device can be different from that of the material utilized. For instance, for a device comprising a crystal of length ℓ parallel to y (direction of propagation) and thickness t parallel to z (direction of applied field), the half-wave voltage would differ from that given by Eq. (2.5.5) by a factor of t/ℓ. Half-wave voltages of the crystals used are usually of the order of kilovolts, but production of such voltages at higher frequencies becomes increasingly costly and difficult. This indicates the importance of using optical waveguide modulators in optical communication systems where modulation bands of the order of 10^9Hz are required. For instance, using a crystal waveguide of t = 20 μm and ℓ = 2 cm, the half-wave voltage of the device would be 10^3 times less than that of the material used.

In the examples considered, the electric field was assumed to be parallel to z-direction (c-axis of the crystal).

It is easy to show that virtually no effect would result from applying an electric field in the x or y direction in a crystal of e.g. mm2 class. Hence it is essential that the geometry of the crystal used should allow efficient application of an electric field in this orientation without difficulty. Exmaples of particular interest here are crystals such as meta-nitroaniline (mNA) and meta-dinitrobenzene (mDNB) grown within fibres (see next Chapter) for making CCOF's. The c-axis in these cases aligns with the fibre axis, making application of the field in this orientation difficult. Ideally, the c-axis of the crystal should be oriented perpendicular to the fibre axis.

However, it can be concluded from a comparison between the electro-optic tensor forms for mm2 and 32 symmetry classes (Section 2.4) that the field should be applied in the x-direction (a-axis of the crystal) if a crystal of 32 class is utilized. Then, if such a crystal grew with its c-axis parallel with the fibre axis, the a-axis would be transverse, facilitating an efficient field application in this orientation.

2.6 Linear Electro-chromic Effect

Eq. (2.4.2) shows that the natural frequency of the dipoles present in the material changes linearly with the application of a static electric field. This alters the absorption coefficient of the crystal in particular at angular frequencies near to ω_o.

Direct evidence of a linear shift in ω_o with the electric field applied was found in mNA crystal (Stevenson et al., 1973). The magnitude of the effect was, however, small.

At present this effect is not regarded as being useful for device applications unless materials are discovered which show a more intense effect.

2.7 Organic Crystals for Electro-optic Light Modulation

It follows from Eq. (2.5.3) that a beam of light passing through a bulk electro-optic crystal is phase modulated by the applied electric field. Amplitude modulation, which is preferred in optical communications, is achieved by using the difference in electro-optic phase retardation between two polarisation directions (e.g. x and y) to rotate the polarisation of the output light. This rotation is then converted to amplitude variation using a polariser.

Inorganic materials, such as potassium dihydrogen phosphate (KDP) and its isomorphs, have been used in the past for electro-optic light modulation. However the relatively recent discovery of the useful electro-optic properties of mNA (Ayers et al., 1972; Stevenson, 1973 II) indicated the potential of the organic crystals for electro-optic device applications. This material combines advantages such as low permittivity, large electro-optic coefficients, easy growth into large single crystals and low cost, a combination which is lacking in many competing inorganic crystals. Subsequently another organic crystal, formyl-nitrophenylhydrazine (FNPH) was found to exhibit an intense electro-optic effect (Owen and White, 1977) which, however, presented difficulties in crystal growth. Many other organic crystals are known which potentially should exhibit strong electro-optic effects (Owen and White, 1976) and each may present a different

combination of properties, increasing the number of choices for device engineering.

Organic crystals, however, suffer from other problems which stem from their mechanical weakness. Difficulties encountered in handling, cutting and polishing for optical quality faces are examples (see, Owen, 1975). Furthermore the quality of the polished faces gradually deteriorates in air in some organic crystals. It is anticipated that the fabrication of crystal cored fibres (described in the next Chapter) will be useful in minimising most of the disadvantages mentioned.

Exhaustive discussions on the optical properties of organic crystals and the correlation with molecular and crystal structure have been made by Stevenson (1973) and Owen (1975) which texts are recommended to the interested reader.

CHAPTER 3

CRYSTAL GROWTH OF ORGANIC MATERIALS IN GLASS CAPILLARIES ("FIBRE GROWTH")

Crystallization of organic optically non-linear materials within glass capillaries with internal diameters of the order of 10 μm was proposed by Stevenson and Dyott (1974) for making crystal cored optical fibres (Section 1.8 and Chapter 4). From another standpoint, this techique of crystal growth was found useful as a means of evaluating organic optical materials generally (Chapters 5 and 6).

The following major problems were reported (Stevenson, 1977) to be encountered in fibre growth using the original methods. All of these problems had also been observed in our pilot experiments, and are further discussed later in this Chapter.

(a) The existence of voids lying between the crystal and the glass wall,

(b) The separations of short segments of crystal within the fibre,

(c) formation of polycrystalline segments,

(d) a very low yield of acceptable CCOF (even by accepting some of the voids quoted in (a) this was below 1%),

(e) and unfavourable orientation of the crystal for device applications.

The results of our investigations for the identification of the origins of these defects and for the solution of the problems, are presented in this Chapter.

3.1 Preliminary Growth Experiments I

The growth of organic materials in glass capillaries down to c. 1mm internal diameter has been used in the past for the measurement of growth rates (the work has been reviewed by Strickland-Constable, 1968), but little information has been given concerning the quality of the crystals grown and the voids present. Therefore our preliminary experiments in capillaries of 10 - 100 μm i.d. were based solely on the information in the original experiments for preparing CCOF (Stevenson and Dyott, 1974) gained through private communications by J.L. Sevenson and R.B. Dyott.

In these experiments crystals of meta-nitroaniline (mNA) had been grown in hollow glass fibres of about 20 μm i.d. using a progressive freezing technique. In order to repeat these experiments a similar apparatus (with some modifications) to the one used in the original experiments was made; a schematic diagram of which is shown in Fig. 3.1. The device consisted of two concentric glass tubes; the outer tube had been covered with a thin film of tin oxide which was divided into two sections which acted as the upper and lower heaters of the furnace. (This was provided by the Post Office Research Station, to whom thanks are due.) The inner tube was closed at one end and connected to a vacuum pump at the other. Inside this tube a hook had been made from which a small reservoir containing the organic material (Fig. 3.1.b) could be suspended.

The hollow fibres used in our experiments were made from pyrex glass and had internal diameters in the range

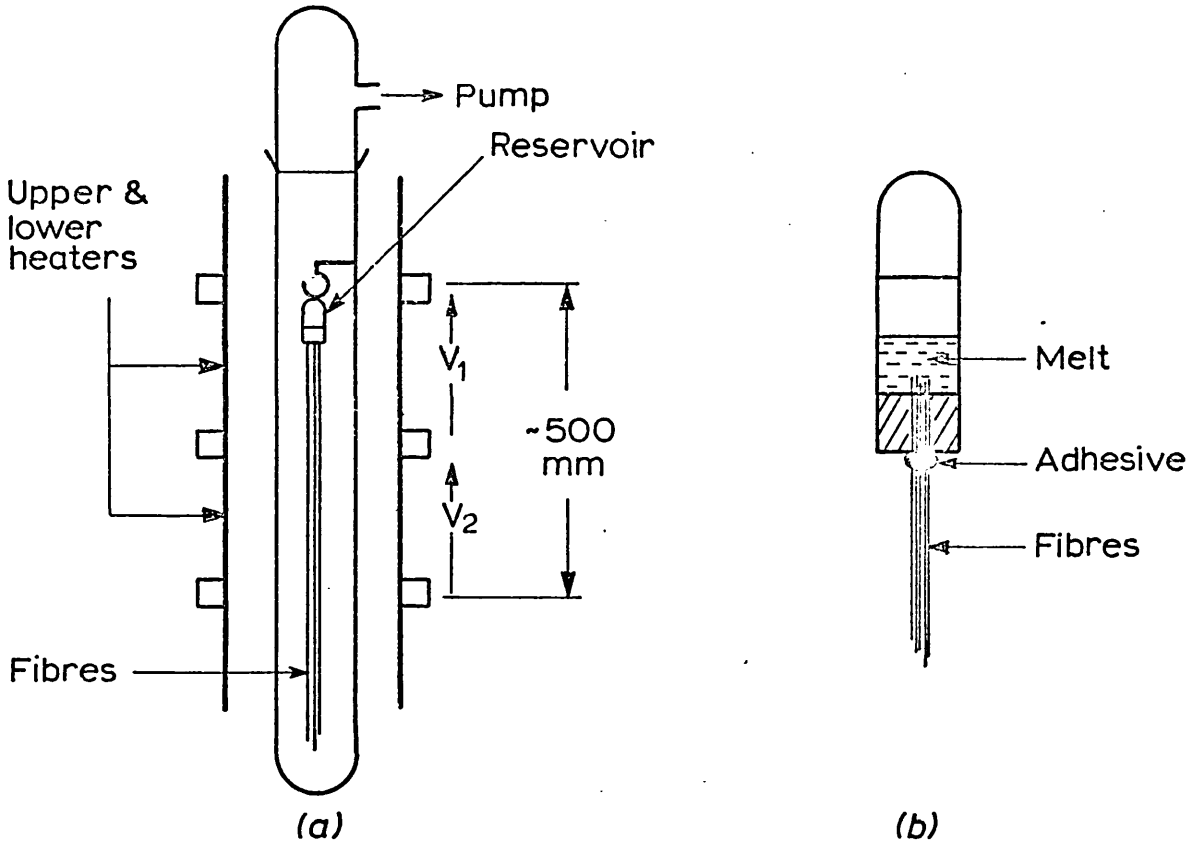

Fig. 3.1. Schematic diagram of the apparatus used for preliminary experiments I.

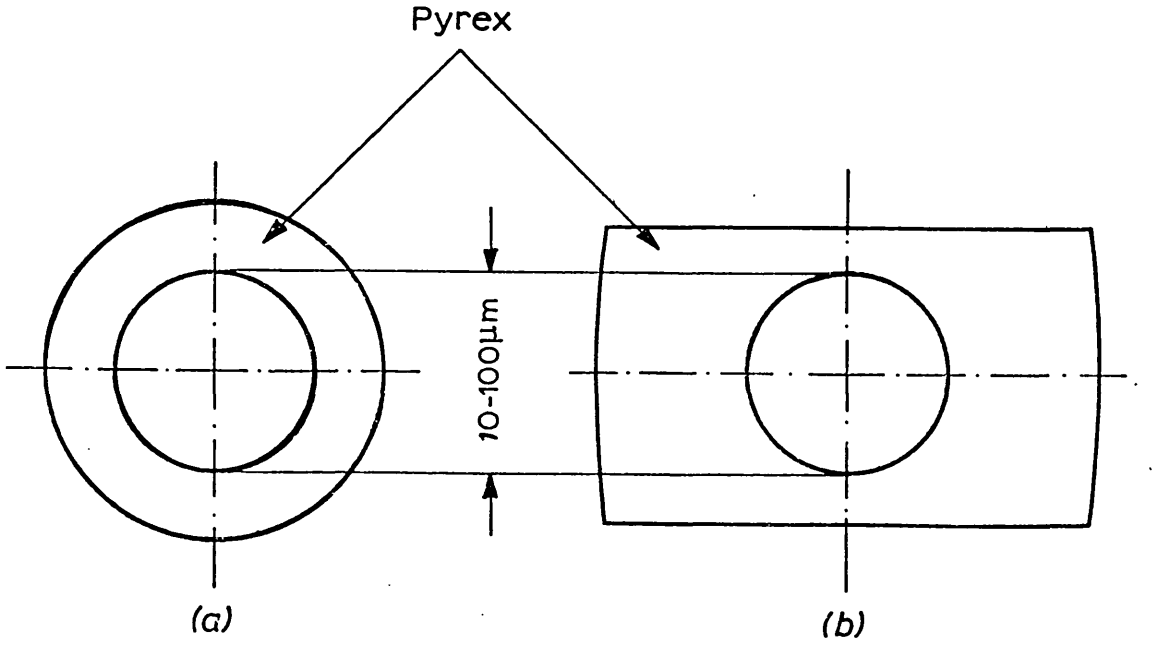

Fig. 3.2. Cross-sectional view of the fibres used.

of 10-100 μm. The hollow core in all cases was circular - or nearly so - but the external geometry was circular for some and rectangular for others (Fig. 3.2). These fibres were pulled down from Pyrex tubes of a various wall thickness. For the rectangular sectioned fibres, pyrex capillary tubes were ground and lapped to give preforms of the desired external geometry.

The first set of growth experiments were carried out on mNA. In each experiment a bundle of 10-20 fibres of about 50 cm length was used. These were inserted into the hole at the bottom of the reservoir and cemented there with Araldite. About 1 g of zone-refined mNA was placed in the reservoir, and the fibre bundle was suspended from the hook provided within the apparatus. After evacuation, upper and lower heaters were switched on. Preliminary to the growth experiments the temperature profiles of the furnace for various applied voltages to the heaters had been measured and the necessary voltages for producing the desired temperatures established. Also the suspension length of the reservoir had been adjusted so that it was located at the hottest point of the furnace when suspended from the hook. The temperature at the bottom ends of the fibres was always about room temperature.

Equal voltages were applied on the upper and lower heaters, so that the temperature near the reservoir was about 10°C above the melting point of the material (112°C for mNA). By melting the material, filling of the empty fibres automatically started by capillary attraction and the gravitational force present. Completion of filling process could be observed from a detectable colour change near to the lower ends of the

fibres (the colour of mNA is orange).

The temperature of the liquid decreased as it travelled downwards within the fibre, and eventually solidification was initiated somewhere near to the lower end where the liquid became supercooled. Solidification then progressed upwards upto the point where the temperature of the furnace was equal to the melting point of the material. Such a point was usually 10-20 cm away from the end of the fibre.

When filling was completed, the voltage on the lower heater was gradually decreased according to a predetermined program. The program was continued till the lower furnace was switched off. Then a similar cooling program used on the upper heater. Growth was completed when crystallization progressed from the top of the fibres into the reservoir. The freezing program was varied from 0.5 to 3 hours in different runs, resulting in different growth rates. After freezing, the reservoir and fibres were taken out of the apparatus, and the fibres cut from the bottom of the reservoir for examination.

A problem which became apparent even from the first run was the reaction between the material to be grown and the glue used for cementing the fibres to the reservoir; even though the reservoir had been designed to minimise this contact. Different kinds of commercially available glues and silicone rubber were tried, with similar results. As a result of the reaction, bubbles were generated which travelled through the liquid in the reservoir, and rapid darkening of the colour of the melt was observed.

The evacuation of the furnace during the growth process caused a relatively rapid evaporation of the melt in

the reservoir, and also appeared to accelerate the reaction between the melt and the glue. Since no detectable change in the colour of molten mNA was observed when the liquid was kept in a test tube in air for about half an hour, and since filling of the fibres took only about three minutes, after a few growth runs it was decided to abandon the evacuation of the furnace and later experiments were carried out in air.

The fibres produced were examined under a microscope. Starting from the lower end, there usually was a length of about 10 cm of polycrystalline material. This was due to the growth from the highly supercooled liquid in the lower region of the furnace. Near to the top end of the polycrystalline section the crystals were of larger grain size, indicating a decrease in the degree of supercooling, and finally they became single crystals. Unfortunately this general pattern was frequently interrupted by different kinds of voids. Some of the common kinds of these voids are shown in Fig. 3.3. A long empty section separating two filled parts is shown in Fig. 3.4a, length of which varied from a few core diamters to about 10 cm. The material at the top of such voids was polycrystalline for a long length, indicating that the liquid in this part became supercooled due to lack of contact with the solid at the other end of the void. The existance of this type of void was attributed to discontinuous filling caused by bubbles present in the liquid or the non-availability of the liquid due to the gradual melting of the solid in the reservoir. Some short examples of this type of void (of the order of a core diameter, Fig.3.3b) showed

single-crystalline material at both ends, showing that there has been some kind of contact between these two parts which has prevented the upper part from supercooling. Such a contact was not observable under microscope. Single crystal sections of the core were generally separated from the glass walls by long voids as shown in Fig. 3.3c the radial extent of which varied from point to point. Many spherical voids (referred to as bubbles hereafter) of various size were also present as shown in Fig. 3.3d. The two latter types of voids were the subject of further investigations and their formation mechanisms are discussed later in this Chapter.

Only short lengths of single crystalline sections were found which were free from all of the above mentioned voids. These lengths were longer in fibres of smaller core diameter but in none of the cases did they exceed 1 mm for core diameters in the approximate range of 30-60 μm. However, accepting the above mentioned separations (voids) between the crystal and its glass cladding single crystalline sections of about 1 cm in length could be selected. The yield of such sections was low and estimated to be below 1%. This was higher in fibres of rectangular cross-section compared to circular sectioned fibres.

Before considering changing the method of growth, one other material was investigated to ensure that the observed difficulties were not specific to mNA. Meta-dinitrobenzene (mDNB) was chosen for this purpose. Some of the optical and non-linear optical properties of this material were reported by Southgate and Hall (1972). The main reasons for the choice were:

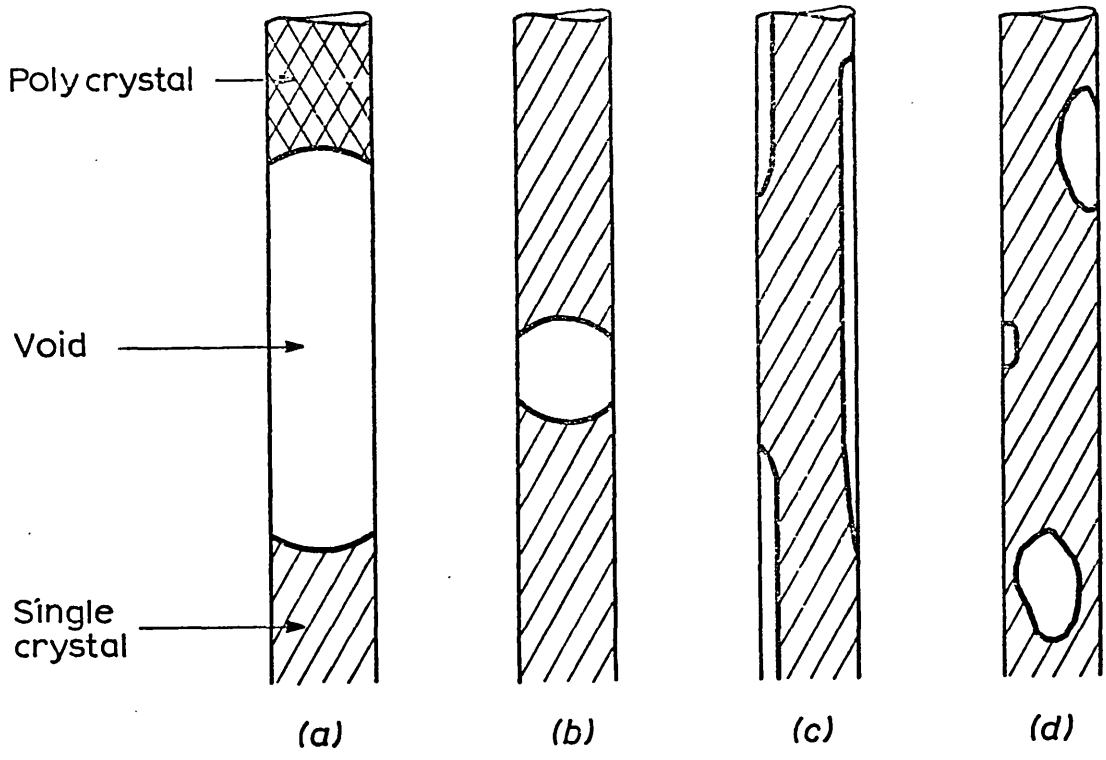

Fig. 3.3. Schematic illustration of the voids present in crystals grown.

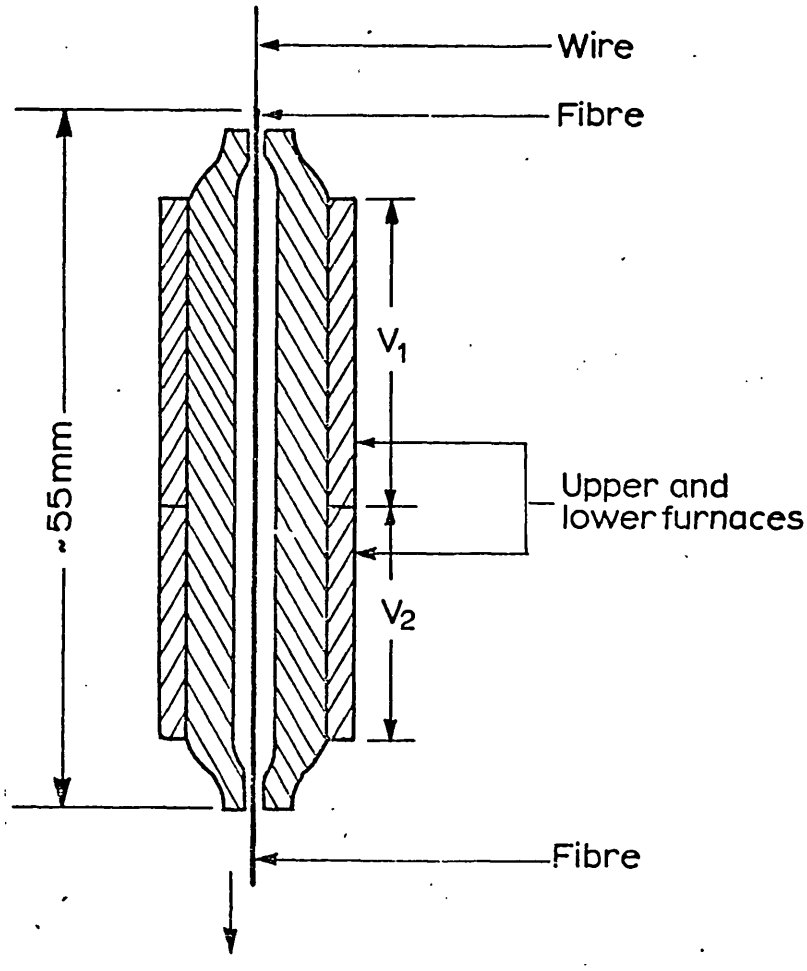

Fig. 3.4. Schematic diagram of the apparatus used for re-crystallization of filled fibres.

a. One of its refractive indices (n_z) is very near to the refractive index of the glass used and this, as shown in Section 3.2, would facilitate the detection of the orientation of the crystal within the fibre.

b. Southgate and Hall (1972) reported the quality of mDNB crystals grown from various solutions to be the poorest of the five materials studied by them. Our attempts to grow bulk crystals of this material from the melt using a conventional Bridgman method also failed (it had been intended to measure the electro-optic coefficients on bulk crystals). Also the vapour growth of this material was later found to be difficult and to result in poor optical quality crystals (S. Al Shookri, private communication). Finally, one of the reasons for the interest in the fibre growth technique was to study the possible advantages it could afford for the growth of organic materials which are intractable by conventional growth methods. Thus mDNB was a suitable candidate in this respect.

Fibre growth experiments were carried out on zone refined mDNB. This material could supercool down to room temperature without initiation of crystallisation. Thus it was necessary to initiate growth by introducing a seed in some manner. This was achieved by the following procedure: the heaters were switched off when filling was completed; after the furnace cooled about 20°C below the melting point a small piece of solid mDNB was dropped into the reservoir; the liquid in the reservoir and in the fibres solidified. Then heaters were switched on again and the growth was carried out as in the case of mNA. When the temperature of the furnace rose above the melting point of mDNB (92°C) the solid

in the reservoir and in the fibres remelted but a few centimeters from the bottom end of the fibres remained unmelted. This section of solid acted as a seed during the growth program.

The microscopic examination of the crystals obtained revealed that the existing voids were very similar to those for mNA. A significant difference was that, the voids between mDNB crystal and the glass cladding were, in general, radially shallower compared with those for mNA. The yield of single-crystal cored segments was lower in the case of mDNB, since growth within the fibre, when interrupted with a long void (Fig. 3.3a), failed to continue further ahead and the rest of the fibre remained as supercooled liquid. More than 80% of the fibres were filled with polycrystalline or liquid material when taken out of the apparatus.

Although the crystals obtained with the method described were unsatisfactory for the applications in mind, their examination revealed the main problems involved in the growth. These, together with the technical difficulties encountered in these experiments were the basis for the design of more refined growth techniques. Furthermore, two significant pieces of information were gained from these experiments: (a) The voids between crystal core and the glass cladding were shallower in the case of mDNB, which encouraged the investigation of other materials. (b) Neglecting these voids, a few mm lengths of fibre-grown mDNB crystals could be separated, which were very clear and evidently of good optical quality. This indicated that a material such as mDNB which is, as mentioned above, difficult to grow with conventional techniques, can be grown as good quality crystals within fibres.

3.2 Preliminary Growth Experiments II

To obtain a greater degree of contol over the growth process, the stages of filling and crystallisation were carried out separately. Also, since none of the possible applications for the fibre grown crystals required lengths greater than about one centimeter the fibres used were reduced to about 10 cm in length compared with 50 cm in the previous experiments.

To fill the fibres, a small quantity (about 0.5 g) of the organic material was placed at the bottom of a glass test tube and heated in a furnace to about 10^{o}C above the melting point of the material. When the melting was completed, several hollow fibres of about 10 cm length were introduced and vertical filling occured by capillary attraction. After solidification of the melt, the fibres filled with poly-crystalline material were removed by breaking the tube.

A diagram of the furnace used for recrystallization is shown in Fig. 3.4. The furnace had a small cross-sectional area and was made from a thick-walled glass tube pulled down at the ends to form a guide for the fibre at the entrance and exit. The recrystallization process was carried out for only one filled fibre at a time. The fibre was cemented to thin wires from both ends, care being taken not to block the upper end, to ensure free movement of the liquid within the fibre. The combination of the wires and the fibre was then threaded through the furnace.

Effectively growth was achieved by the Bridgman technique; that is, material within the fibre was first melted, and then recrystallized progressively. The filled

fibre was placed in the furnace so that at least a few mm from its lower end was out of the furnace. This ensured that some of the crystal remained unmelted to act as seed for crystallization. The temperatures of the upper and lower regions of the furnace were raised to about $5^{o}C$ above and $10^{o}C$ below the melting point respectively. The fibre was pulled downwards through the furnace at rates of 25-50 $mmhr^{-1}$. After preliminary experiments it was found that the use of two heaters was unnecessary; better results were obtained when two heaters acted as one and the solid-liquid interface was brought down near to the bottom of the furnace.

Microscopic examination of the samples obtained with mDNB showed that the voids present were mainly of the types shown in Figs. 3.3c and d only. Other types of defects (Fig. 3.3 a & b) were rare. However, the density of the voids between crystal and its cladding was not much improved. Accepting the presence of the latter type of void (these voids in fact were outside the crystal rather than inside, but as is shown in the following Chapters, they are detrimental for some of the applications of fibre grown crystals) good quality crystals of upto 30 mm length were obtained in fibres of rectangular cladding. The lengths of such crystals were limited by the occurence of bubbles (Fig. 3.3d), which also interefered with the reproducibility of long crystals. In circularly clad fibres, however, the presence of cracks were the main limiting features, which reduced the length of acceptable fibres to the order of mm. In these experiments fibres with internal diameters of about 40 μm were used.

The difference between crystals obtained in the two different types of fibres was attributed to the geometry of the cladding.

In the case of a rectangularly clad fibre it was apparent that, due to the variation in thermal capacity of the fibre cladding in various directions, transverse temperature gradients were set up which helped to determine the alignment of the crystal in the cross-sectional plane. In order to enhance the conditions of growth in circular cross-section fibres which were needed for some applications (Chapter 6), the furnace was modified to impose a small transverse temperature gradient on circular fibres. This was done by sticking an aluminium sheet of about 5x8 cm 180^{o} around the furnace, which acted as heat sink and produced a temperature difference between the two sides of the furnace. Using the modified furnace, the number of cracks was reduced and the length and quality of the single crystals obtained was increased.

This method of growth was used for two additional materials: (a), 2-bromo 4-nitroaniline (BNA), which was also one of the five materials studied by Southgate and Hall (1972). The material was purified by successive crystalizations from ethanol solutions, since zone refining was found not to be suitable for this material owing to decomposition. Using the technique described above, results similar to those for mDNB were obtained. (b) Formyl nitrophynyl hydrazine (FNPH), which has been studied by Owen and White (1977) who reported that it was difficult to crystallize by conventional methods due to its gradual decomposition either in solution or in melt. The material had been synthesized in our

laboratories and was available in a purified form. This material showed a higher tendency for the formation of different types of void, especially in the form of bubbles. It was later observed that the viscosity of the melt in this material rapidly increases with decreasing temperature, and it was easily possible to keep the material in a glass-like state by rapid cooling. It is shown in Section 3.8.1 that such materials are not suitable for the growth of void-free fibres, because of the tendency for bubble formation to increase with the viscosity of the melt.

Samples obtained for all of the above materials showed a total extinction when aligned parallel with the direction of polarization, viewed under a polarizing microscope with crossed polarizers. This indicated that all of the three materials studied (mDNB, BNA and FNPH) grew within the fibres with one of their principal dielectric axes aligned with the axis of the fibre. Deviations of upto 5^{o} from this alignment were observed occasionally in some samples. In the case of mDNB the identification of this axis was easily achieved. Refractive indices of mDNB at λ = 589 nm are n_x = 1.74, n_y = 1.71 and n_z = 1.49, whereas the refractive index of the cladding glass at this wavelength was measured by Abbe refractometer to be 1.478. When the direction of polarization of the illuminating light was parallel to the c-axis of the crystal the contrast between the core and cladding was much lower than with other polarization directions (Fig. 3.5). Accordingly, the c-axis of the crystal was found to align with the fibre axis. A similar result had already been reported for mNA by Stevenson and Dyott (1974).

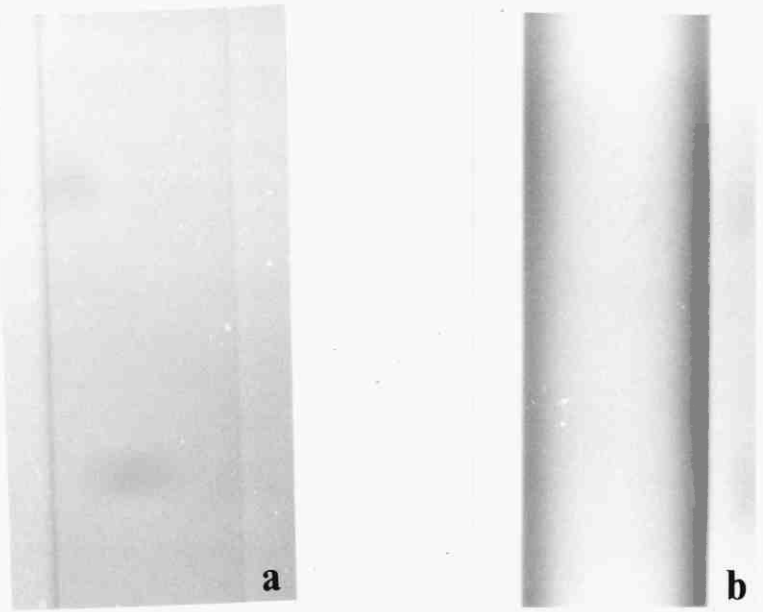

Fig. 3.5. Photographs of a mDNB-Pyrex fibre when illuminated by light polarized (a) parallel to the fibre axis, (b) perpendicular to the fibre axis.

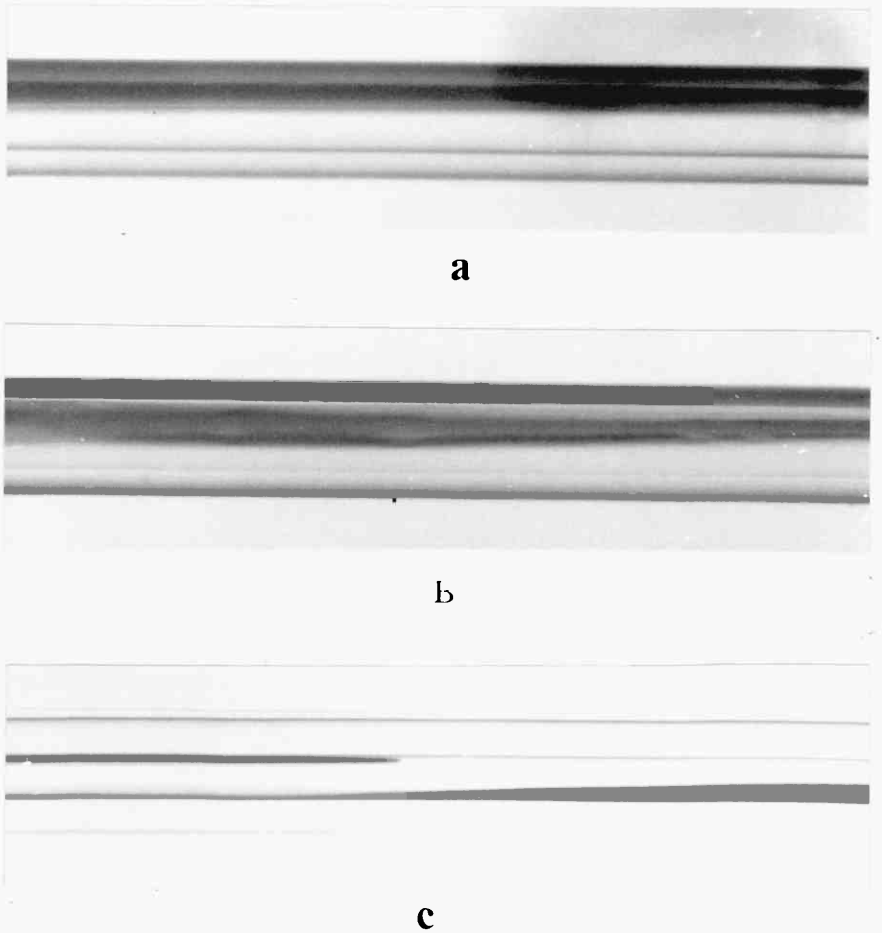

Fig. 3.6. Various shapes of the voids occurring between the crystal core and glass cladding (mDNB).

In this section, a method for the fibre growth was described which solved many of the problems mentioned in the previous section. As a result, long lengths of good quality crystals were obtained in materials which were known to be intractable with conventional methods. However the two kinds of voids shown in Fig. 3.3c and d remained almost unaffected compared with the results of the previous method. Clearly, for any further improvement in growth, the formation mechanisms of these voids should be determined.

3.3 Voids

Separation between the glass cladding and the crystal core tended to occur in both of the preparation methods described, and various shapes of the resulting cavities are shown in Fig. 3.6 a-c.

In order to study the mechanisms involved in the formation of these voids a miniature furnace was made which allowed direct observation of the crystal growth within the fibre under a microscope. A schematic diagram of the device is shown in Fig. 3.7. The device itself was made of two glass slides between which a small heater had been constructed. The hot and cold regions were separated with a thin sheet metal (baffle) which had a small hole (D ≈ 0.3 mm) in the middle for the fibre to pass through. In order to keep the fibre in a straight line, support brackets were provided in both sides of the baffle. A constant pulling rate was provided by a micromanipulator geared to a small electric motor. By disengaging the motor, pulling could be carried out manually by rotation of the micromanipulator. Two different

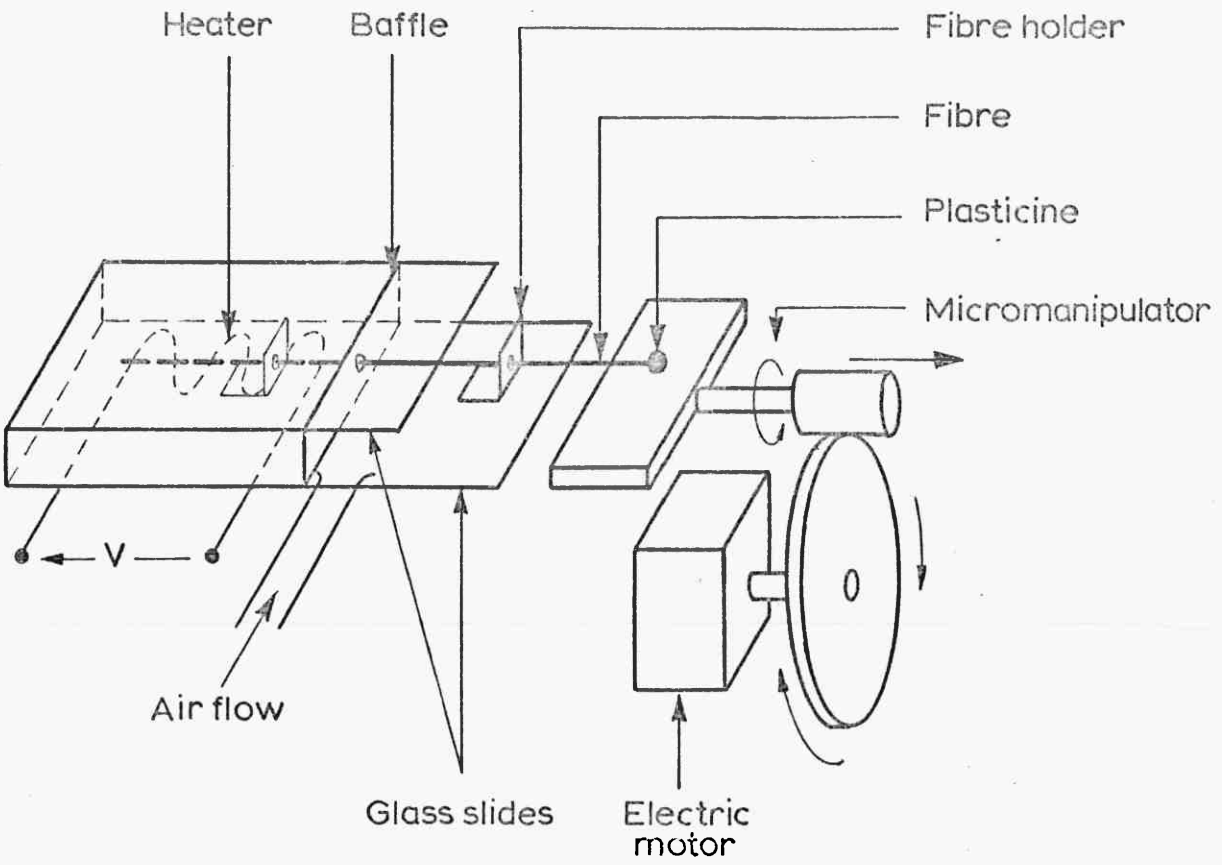

Fig. 3.7. Schematic diagram of the miniature furnace used for direct observation of the growth process.

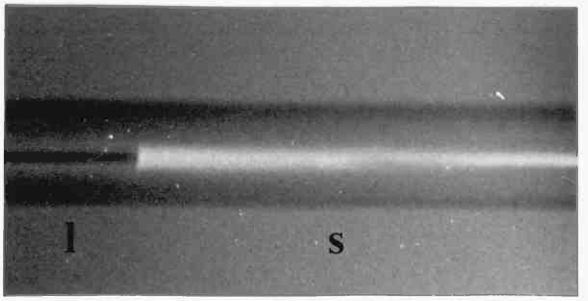

Fig. 3.8. Photograph of the solid-liquid interface observed using a polarizing microscope with crossed polars.

versions of this furnace were built, one that could be operated under a low magnification steroscopic microscope, and the other suitable for use with a polarizing microscope. Photographs of both versions of the furnace are shown in the Appendix.

The temperature gradient near the baffle was measured to be about $20^{o}C\ cm^{-1}$. The temperature of the hot region (measured at the centre) was raised to about $10^{o}C$ above the melting point of the material and a fibre, filled in the manner described in Section 3.2, was pulled axially parallel to the direction of the temperature gradient. In these experiments, fibres with internal diameters in the range of 30-100 μm were used; larger diameter fibres provided better observation of the process. A well defined solid-liquid interface was observed (Fig. 3.8), beyond which the crystal was clear and in intimate contact with the glass cladding; but the position of the interface was not fixed due to the sensitivity of the fibre to temperature fluctuations. However, some distance away from the interface (c a. 5 mm) the crystal separated from the glass and the point of separation propagated towards the interface, producing an elongated void. In smaller diameter fibres and for slower pulling rates the point of void formation was generally further from the interface.

Similar effects were observed for mNA, BNA, mDNB, m-dihydroxybenzene (mDHB) and benzil. The latter materials have been investigated for their non-linear optical properties by Southgate and Hall (1972) and Gott (1971) respectively. mDHB underwent a temperature-sensitive structure change,

(Robertson, 1936; Robertson and Ubbelohde, 1938) which did not, however, destructively affect the resulting crystal.

Having observed that the void formation initiates some distance away (compared with the diameter of the cyrstal) from the solid-liquid interface it was logical to think that the density of the voids would decrease if this could take place as near to the interface as possible (see Section 3.9.1). This obviously could be achieved by the use of larger temperature gradients near the solid liquid interface. For this purpose an air flow was established in the cold region of the device, as shown in Fig. 3.7. The rate of the flow was controlled and stabilized by using a gas regulator.

A considerable decrease in the void density, compared with that in the previously grown fibres, was observed. Also changes in the shape of the voids were noticed, which are discussed in Section 3.6. Furthermore by increasing the temperature gradient the instability in the position of the solid-liquid interface observed previously, disappeared. It was thought that the application of an air flow might have enhanced the interface fluctuations but it was observed that the increased temperature gradient stabilized the position of the solid-liquid interface.

It was concluded that an apparatus should be designed for fibre growth which could provide as large a temperature gradient as possible near the interface. The design and construction of such an apparatus is the subject of the next section.

Other observations of the growth process and the study of formation mechanisms for other types of voids were

carried out using the miniature furnaces. The results obtained are given in appropriate places in the present Chapter.

3.4 Preliminary Experiments III

After demonstrating that increasing the temperature gradient within the furnace decreases the void density, a Bridgman furnace was designed to obtain larger temperature gradients. A schematic diagram of the furnace is shown in Fig. 3.9b. The pitch of the wiring of the upper heater was higher near the cold region and the two regions were separated by a metal baffle. The baffle had a long narrow slit at the middle through which a glass slide could travel. The lower heater was used only for growth studies in lower temperature gradients, and was normally shut off during the growth process.

Several filled fibres were stuck to a glass slide as shown in Fig. 3.9a and located within the furnace so that a few mm of the fibres and the slide were within the cold region. The furnace was then switched on to raise the temperature of the hot region to about 10^{o}C above the melting point of the material. The fibres were, then, lowered at a constant rate through the baffle.

The temperature profile of the apparatus was measured by pulling a thermocouple along the furnace (Fig. 3.9c). It was found that due to the low melting points of the materials used (around 100^{o}C) it was difficult to establish temperature gradients greater than 15^{o}C cm^{-1} (the maximum measured value). However, this apparatus

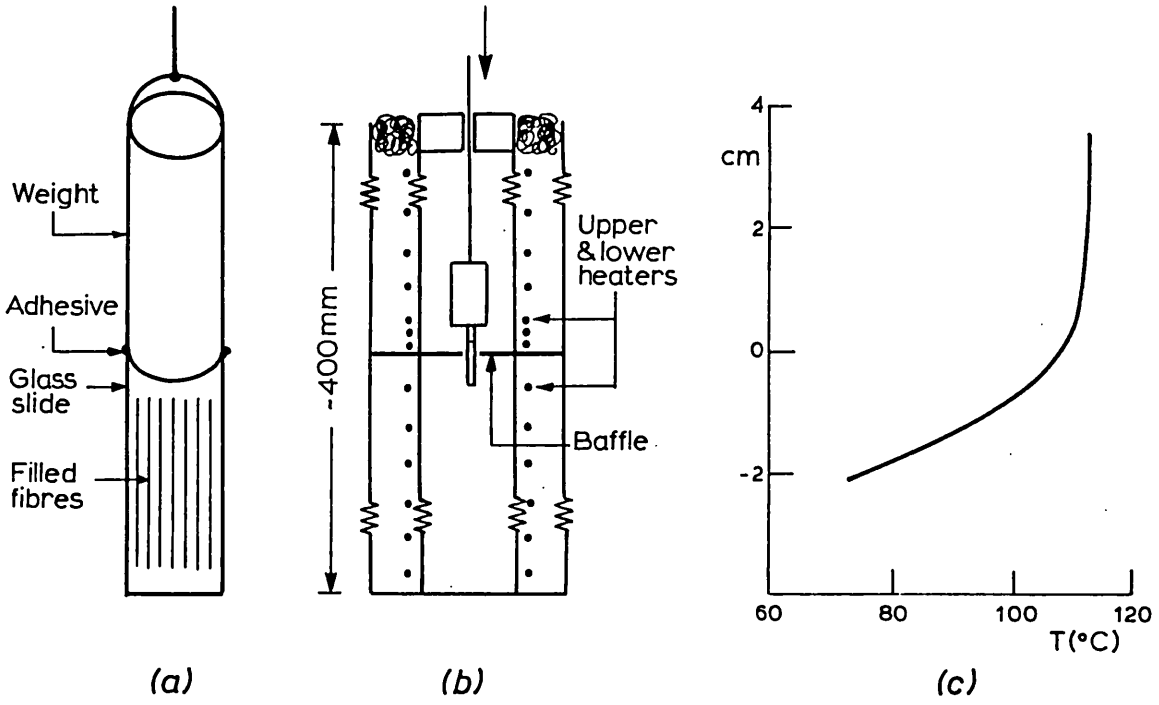

Fig. 3.9. Schematic diagram of the apparatus used in preliminary experiments III.

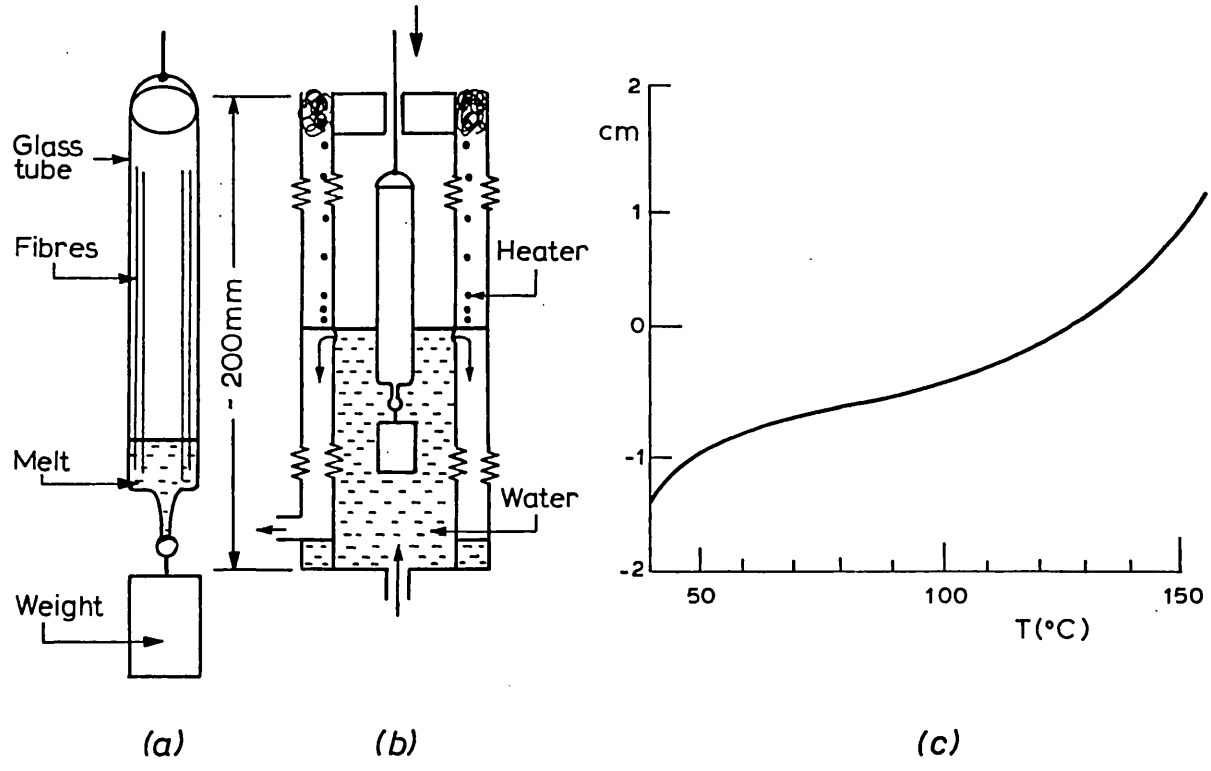

Fig. 3.10. Schematic diagram of the apparatus used for void-free growth.

allowed a study to be made of the void denisty against temperature gradient in the limited range of 0-15^{o}C cm^{-1}. This showed, in agreement with previous results, that the tendency for void formation decreased as the temperature gradient increased. These experiments were carried out on mDNB within fibres of 15-10 μm i.d.

As in the previous results (Section 3.2), there were bubbles present within the crystal products, in addition to the voids between the crystal and glass cladding. The occurrence of these bubbles remained virtually unaffected when the temperature gradient was varied.

3.5 Apparatus and Growth Process

The problem of establishing a large temperature gradient for the bulk growth of organic crystals by the Bridgeman technique had already been solved by Guilland et al. (1970) who used a mercury bath as the cold region in the apparatus. For fibre growth a simplified version of this apparatus was constructed in which the cold region consisted of a volume of slowly flowing cold water, the level of which was defined by holes made in an inner glass jacket (Fig. 3.10). It was found to be beneficial to stabilize the water level by inserting short lengths of wire through the holes, which assisted a smooth, continuous flow. The inner surface of the water tube was coated with a thin layer of high melting point wax to minimize the effects of surface tension. The rate of water flow and the water temperature were kept constant.

In order to measure the temperature profile a thermocouple was placed in a thin-walled glass tube and

lowered through the apparatus at 40 $mmhr^{-1}$. A schematic diagram of the apparatus and the temperature profile is shown in Fig. 3.10. Temperature gradients up to $120^{o}C\ cm^{-1}$ were measured, but the actual temperature gradient should be larger owing to the errors caused by heat conduction through the thermocouple and the glass tube.

In the search for the origin of the bubbles within the crystals, remelting of the filled fibres (polycrystalline) was studied under the microscope using the miniature furnace. It was observed that many micro-bubbles were released from the polycrystalline core during its remelting. Some of these bubbles joined together and gave rise to larger bubbles, some as large as the cross-section of the fibre. The small bubbles tended to disappear gradually when the fibre was heated to $30^{o}C$ above the melting point of the material, but the larger ones were quite stable. It is not possible, at present, to clarify the nature of these bubbles. It was concluded that for better results filling and crystallization should be carried out in one step.

A small amount of material (about 0.5g) was placed in the bottom of a narrow thin walled test tube which was tapered at the bottom (Fig. 3.10a) and the outer surface coated with a thin layer of high melting point wax. It was placed in the heater and the temperature raised to about $25^{o}C$ above the melting point. No decomposition was observed (mDNB and Benzil) at this temperature during the process which was about 1.5 hr in duration. When the material had melted any small air bubbles trapped in the melt were eliminated by gentle shaking for a few minutes. The hollow fibres were then introduced and filling occurred by capillary attraction.

For benzil a bundle of about 10 fibres, cemented to each other by a small epoxy-resin contact near to the top end, was used. The cemented point was far from the material at the bottom of the tube. In the case of mDNB, for which a small transverse gradient relative to the fibre axis was found to enhance growth, a few separate fibres were introduced. These adhered to the wall of the tube by surface tension, and thus experienced a small transverse gradient due to heat conduction through the tube wall. In both cases the tube containing the filled fibres was lowered through the heater. When the tube had travelled to the colder region, the heater was switched off, the tube taken out and the fibres extracted by breaking the tube.

The hollow fibres used in these experiments had circular cross-sections and various core to cladding ratios. Some fibres of rectangular external geometry (Fig. 3.2b) were used for photographic purposes since they allowed better observation of the core. In the case of circularly-cladded fibres good visibility into the core was obtained by immersion in a refractive index matching liquid.

Growth experiments were carried out for mDNB and benzil. Only one experiment was made with mDHB which resulted in an adequate number of samples for refractive index measurements (Chapter 6).

3.6 Results

3.6.1 Growth Conditions and Void Formation

Crystallization of both mDNB and benzil was studied to find the optimum growth conditions. The following factors

were found to be important in void formation:

(a) The nature of the organic material - void density was found to depend on some of the physical and chemical properties of the material under the growth conditions (discussed in Section 3.9.1). To compare different materials from the viewpoint of void formation, crystals of mNA, mDNB, BNA, mDHB and benzil were grown in similar growth conditions, using the miniature furnace (without air flow). Benzil was found to give the lowest void content; mDHB and mDNB were second in rank; BNA was third; and mNA had the highest tendency for void formation. It was concluded from the results reported in Section 3.2 that FNPH also produces a high void density, similar to, if not higher than, mNA. (Strangely enough, the second harmonic generation reported in the literature for these materials varies in the same order! (see, Gott (1971), Southgate and Hall (1972), and Owen and White (1976)).

(b) The temperature gradient near to the solid-liquid interface: The void density decreased with increasing temperature gradient. The shapes of the voids also changed; for very small gradients the voids were wide in circumferential spread and ran for long distances along the fibre without interruption (Fig. 3.6 a & b). By increasing the gradient the voids appeared as isolated, long wedge shaped cavities with the thicker end of the wedge pointing towards growth direction (Fig. 3.6 c). By a further increase, their number and length decreased (Fig. 3.11), and finally the number decreased to such a level that long lengths of voidless fibres could be obtained. In the case of benzil, however, by increasing the gradient, the voids appeared as long and narrow grooves (Fig. 3.12) parallel with the fibre axes,

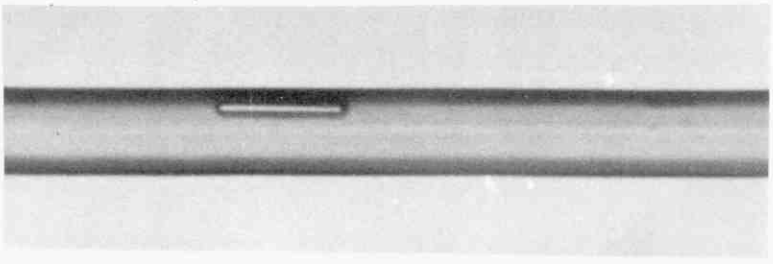

Fig. 3.11. Photograph of a typical void occuring in crystals grown using large temperature gradients.

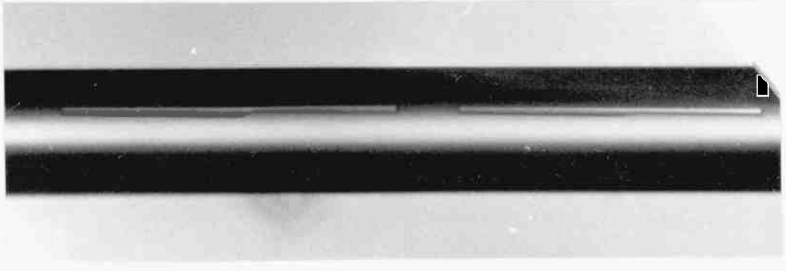

Fig. 3.12. A photograph of the voids observed in benzil crystals.

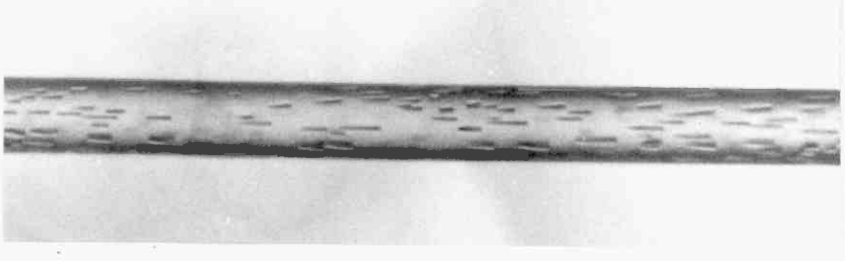

Fig. 3.13. Photograph of the microvoids, forming a "cloud" around the crystal (mDNB).

and on further increase in gradient their depth, length and number decreased and finally were eliminated. In some rare cases two grooves parallel with each other were observed.

(c) Fibre cross-section:- Growth in fibres of large internal diameter resulted in a high level of voids (compared with growth in small fibres under similar conditions), and a correspondingly larger interface temperature gradient was needed to eliminate them. However there was a maximum internal diameter for each material beyond which no totally voidless sample could be produced in the apparatus employed.

(d) Pulling rate:- The effect of pulling rate on voids was difficult to establish, since their occurrence was not reproducible. However a general view was obtained from the examination of many samples grown at different pulling rates by the apparatus described in Section 3.4 and 5, and also by direct observation of the growth process, using the miniature furnace with manual pulling. In general, the pulling rate was found to influence the shape and number of voids. For high pulling rates (> 10 $cmhr^{-1}$) there was a tendency for voids to spread circumferentially giving a crescent shaped cross-section extending up to half way round the fibre. At low pulling rates (1 cm hr^{-1}), and particularly for mDNB in large sectioned fibres (>60 μm i.d.), the voids tended to occur as a cloud of very small shallow voids around the crystal-glass interface (Fig. 3.13).

In general the void density seemed to be smaller for lower pulling rates. Also subsequent light propagation studies (see Chapter 4) revealed that the continuous scattering of light from the guide is considerable in fibres grown using very high pulling rates. This was attributed to a residual stress in these fibres.

The study of factors (a), (b) and (c) was carried out using a pulling rate of 4 cm hr^{-1}. Using the apparatus described in Section 3.5 void-free crystals of lengths upto 4.5 cm (the limit for the apparatus) were produced in fibres of upto 50 and 35 μm i.d. for benzil and mDNB, respectively. The reproducibility of void-free growth in such length was limited by the occurrence of a short length of void (Fig.3.11), or by the formation of voids of a different type, which are described below. For larger diameter fibres some voids appeared, but shorter lengths of void-free fibres were obtainable.

The second type of void observed was of a totally different shape (Fig. 3.14). These occurred in a regular row along a limited length of the sample,ended in some cases by the occurrence of a bubble within the crystal, and were much deeper but shorter than the voids already described. Direct observation of their formation during growth (using the miniature furnace) showed that they originated from bubbles present initially in the liquid, which became trapped at the solid-liquid interface. The bubble moved with the interface and at intervals formed a "tail" which became isolated from the main bubble by progress of the interface. The process continued until the bubble was completely consumed. For smaller fibres (<20 μm) such bubbles completely blocked the core, dividing the crystal into two separate regions, as illustrated in Fig. 3.3b.

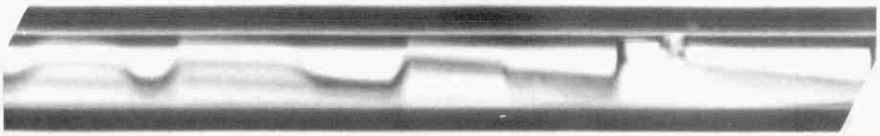

Fig. 3.14. Photograph of bubble-derived voids.

Table 3.1. Refractive indices at 633 nm

	benzil	mDNB	mDHB
n_x	1.651	1.738	1.574
n_y	1.651	1.707	1.619
$n_{\bar{x}}$	1.674	1.485	1.621

The number of voids of this second type was much higher in samples produced by the method of separate filling since many small bubbles were produced during remelting, as described in Section 3.5. By combining these stages of the process in the apparatus described in section 3.5 and taking precautions to prevent the introduction of bubbles into the fibre during filling, the number of bubbles was drastically decreased. However, at high pulling rates, and particularly for small diameter fibres (<20 μm) bubbles could be generated in the liquid adjacent to the interface during growth. This occurs due to the decrease in the volume of the material on solidification which is to be compensated for by the flow of liquid towards the interface. If such a flow is not of a sufficient rate, the volume decrease is compensated for by bubble generation.

Although bubbles and bubble-derived voids were rare in large diameter fibres, they caused a serious problem for fibres of <15 μm i.d., presenting a lower size limit for the preparation of the defect-free filled fibres.

3.6.2 Optical Examination

The obtained crystals were examined under a microscope at various magnifications. Void-free crystals obtained were totally clear and no optical defects were detected either within the crystal or at the crystal-glass interface. (The maximum magnification used in these examinations was x 300.)

The optical quality of the crystal cores was also assessed by examining the continuity of their birefringence fringes (mDNB), or the continuity of the interference colours

when illuminated by white light (benzil) (see, e.g. Bloss, 1961). The birefringence of mDNB is high (Table 3.1) and many fringes were apparent even for the smallest diameter fibres studied. On the other hand benzil is weakly birefringent (Table 3.1) and showed low-order colours in the fibre size range studied, but did not show sufficient fringes to allow assessment. Fig. 3.15 a and b show the fringes in a specimen of mDNB at λ = 548 nm and interference colours in a specimen of benzil, respectively.

The fibres were also assessed by observation of light scattering from voids or defects, either within the crystal or at the crystal-glass interface, using a He-Ne laser beam launched into the core. Good quality void-free single crystal filled fibres allowed transmission with no major scattering points (Chapter 4).

3.6.3 X-Ray Examination

Crystal cored fibres of both mDNB and benzil were examined by X-ray diffraction in a Weissenberg camera (see, e.g. Stout and Jensen, 1968). Suitable lengths of fibres were cut and mounted, using a high core to cladding ratio to reduce absorption and diffuse scattering by the glass. The scattering intensity is proportional to the volume of material and

$$\frac{V_{glass}}{V_{crystal}} = \frac{a^2 - b^2}{b^2} = \left(\frac{a}{b}\right)^2 - 1$$

where a and b are the outer and inner diameters respectively.

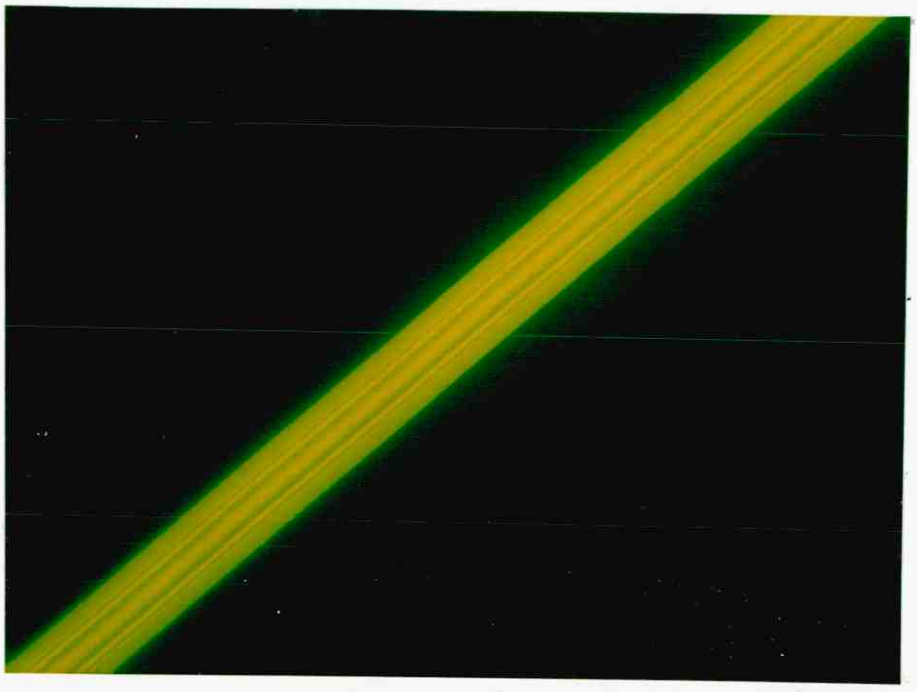

a

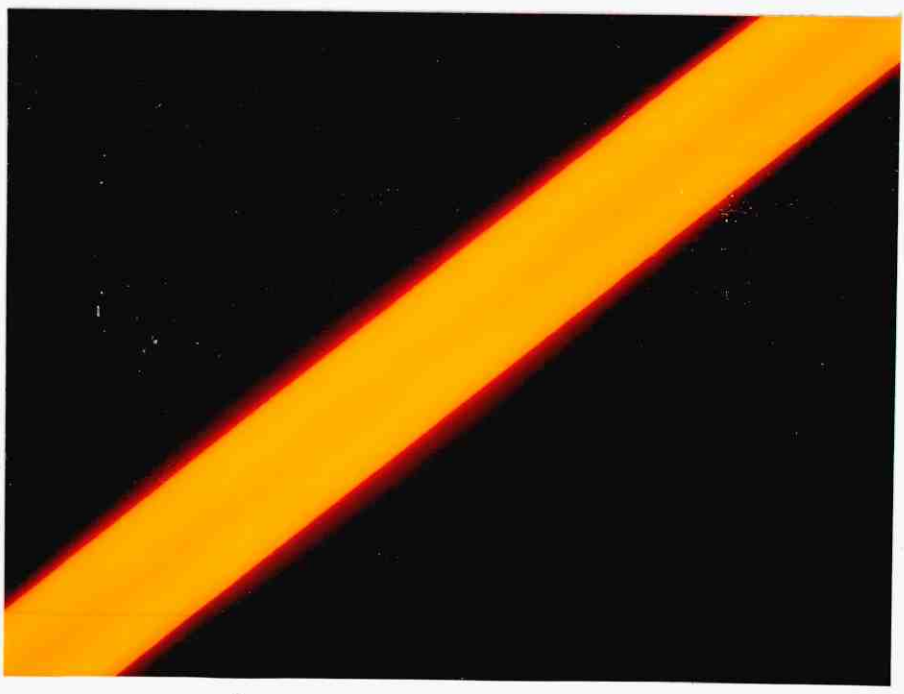

b

Fig. 3.15. (a) Photograph of birefringence fringes of mDNB at λ=548nm. (b) Benzil crystal observed between crossed polars, illuminated by white light.

b/a = 0.65 and 0.50 for mDNB and benzil samples used respectively, and hence the respective $V_{glass}/V_{crystal}$ ratios were 1.3 and 3.0.

Initially the mDNB fibre was aligned with the camera axis and it was found that the crystal orientation was inclined about 1^{o} from the fibre axis. The oscillation photograph for the corrected orientation is shown in Fig. 3.16. This enabled the crystal axis aligned with the camera axis to be identified as the c-axis. The diffuse bands near the centre result from the glass cladding.

The diameter of the X-ray beam was about 1 mm which was nearly 20 times larger than the diameter of the crystal. Hence the sharpness of the spots on the scattering pattern is also an indication of the good quality of the crystals.

A similar examination was carried out on a specimen of benzil in which the preferred growth orientation (c-axis) was inclined about 30^{o} from the fibre axis. The purpose of the experiment was to reveal possible stresses in the crystal due to the unusual growth orientation. The diameter of the crystal was 40 μm; it had been grown by the apparatus described in Section 3.5 using a pulling rate of 40 mm hr^{-1} and the fibre appeared totally void-less under the microscope. The diffraction spots of the X-ray pattern were even sharper than those in Fig. 3.16. Indicating that the crystal was free from major stresses.

3.7 Orientation of Fibre Grown Crystals

Using a polarizing microscope, it was possible to establish that one of the principal dielectric axes of fibre

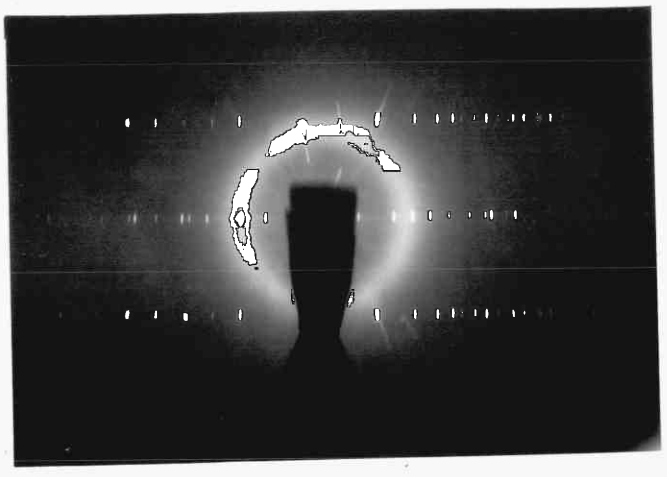

Fig. 3.16. X-ray, oscillation photograph obtained for a mDNB-Pyrex fibre.

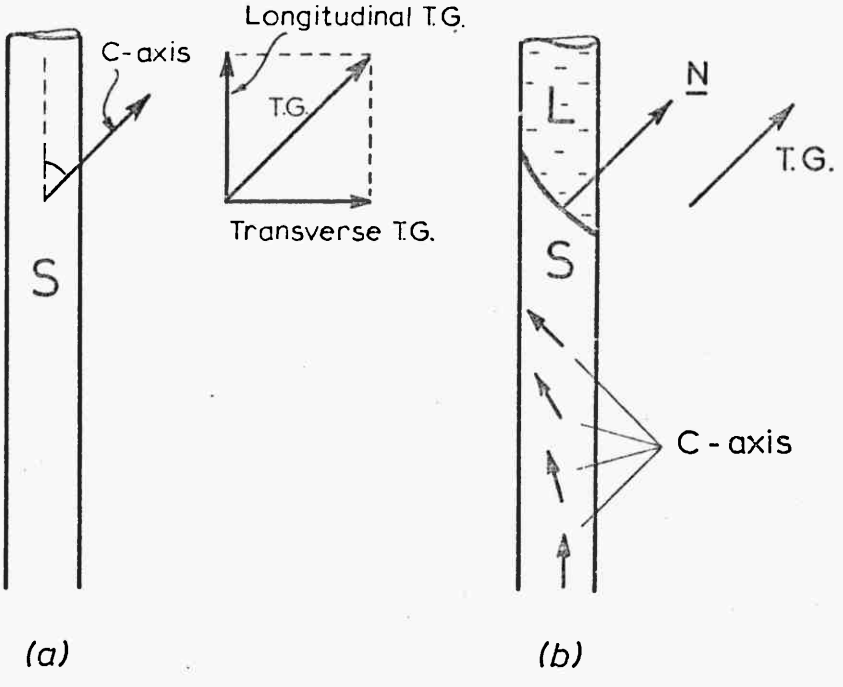

Fig. 3.17. Schematic illustration of the relation between crystal orientations and temperature gradient.

grown crystals was aligned with the fibre axis. In the case of mDNB the axis aligned with the fibre axis was identified as z (c-axis) by both optical and X-ray examinations of the fibres. In benzil and mDHB also the c-axis of the crystal was found to be aligned with the fibre axis by the measurement of the refractive index of the crystal in this direction using the method described in Chapter 6. A similar result had also been reported for mNA by Stevenson and Dyott (1974). For FNPH and BNA the alignment remained unidentified.

The orientation of nearly 100 samples of fibre grown mDNB was determined. The c-axis was usually parallel to the fibre axis to within 5^{o}. Deviations of about 15^{o} were rare and only observed in a few specimens of < 20 μm diameter. No deterioration in the quality of these unusually oriented specimens was apparent from microscopic examination.

Conversely, the orientation of benzil specimens was not so consistent and although in the majority of the samples the z axes (also the optic axis of the crystal) was parallel to the fibre axis, or nearly so, deviations of upto 30^{o} were observed in many samples.

The orientations of the two other principal dielectric axes lying in the cross-sectional plane were not determined. However, it has been reported by Stevenson (1977) that x and y axes of mNA have always a constant alignment on the cross-sectional plane of a rectangularly clad fibre. It was also demonstrated that a thermal asymmetry in the furnace or in the fibre cladding enhanced the conditions for the growth of good quality crystals (Section 3.2).

The above experimental results on the autoalignment of the crystals within the fibres could be explained with the

following model: In growth from the melt there is a problem of transferring the liberated latent heat from the solid-liquid interface. Heat-transfer would be enhanced if the crystal grew so that its maximum thermal conductivity direction were aligned with the direction of the temperature gradient present. The preference for such an orientation, would be more pronounced in the case of a material with a marked anisotropy in thermal conductivity. If spontaneous nucleation is used to initiate the growth then the orientation of the crystal formed is usually in this preferred direction.

Since both the permittivity and the thermal conductivity can be described by second rank tensors, for crystals of orthorohmbic symmetry system (all materials studied in this work with the exception of benzil belong to this class) one of the principal dielectric axes of the crystal will coincide with the direction of the highest thermal conductivity. Hence the material will crystallize with one of its principal dielectric axes aligned with the temperature gradient (fibre axis).

It can similarly be argued that if there is a small component of the temperature gradient perpendicular to the fibre axis it will assist the alignment of the two other crystal axes on the cross-sectional plane.

Although the model explains the previous experimental results, it is not in agreement with the result of a further experiment described in Section 3.8.1. Furthermore, considering that the thermal conductivity of the glass is higher than that for most of the organic materials, heat-transfer from the interface, in a capillary of the diameter range

studied, is most likely to be through the cladding rather than the crystal, and hence anisotropy in crystal thermal conductivity is not likely to have a dominant role in determining the crystal orientation.

It is shown in Chapters 2 and 4 that the natural alignment of the crystals within the fibres is unfavourable for electro-optic device applications, owing to the difficulties involved in the establishing an electric field along the fibre axis. To overcome this problem two approaches were made:

(a) To search for a material whose form of electro-optic tensor permits application of an electric field in a direction other than the z-axis. The material chosen in this respect was benzil which belongs to 32 symmetry class and it can be seen from the related electro-optic tensor that the favourable electric field direction is parallel to the x-axis of the crystal (Chapter 2). The fibre growth of this material was studied, the results of which were presented earlier in this Chapter. Apart from the orientational advantage, benzil was found to be the most suitable material of those studied for the preparation of defect-free crystal fibres. However, although the electro-optic coefficients of this material have not yet been measured, it can be inferred from the published second harmonic generation coefficients (Gott, 1971) that the electro-optic effect in benzil would be considerably weaker than that in mNA (Ayers et al., 1972) or FNPH (Owen and White, 1977).

(b) To control and alter the alignment of crystals such as mDNB during the growth process. The results are presented in the following Section.

3.8 Control of the Crystal Alignment within the Fibres

3.8.1 By temperature gradient orientation

It follows from the above explanation for the autoalignment of the fibre grown crystals, that by establishing a large tranverse temperature gradient the direction of the highest thermal conductivity (evidently the z-axis) should tend to be oriented at an angle to the fibre axis as shown in Fig. 3.17a.

The first attempt at orientation control was to cement ribbons of aluminium foil (1x50 mm) on one side of mDNB filled fibres and pull them through a longitudinal temperature gradient provided by the apparatus shown in Fig. 3.9 or Fig. 3.10. A relatively large transverse temperature gradient was expected to be established due to the high rate of thermal conduction through the metal sheet. However, the result was negative, i.e. no rotation of the alignment of the fibre was detected in the specimens grown.

In another attempt fibres were pulled through the apparatus shown in Fig. 3.9 while the axis of the fibres made an angle of 45^{o} with the axis of the apparatus. Again no change in the orientation of the crystal was observed.

These experiments were also repeated for mDHB, since its optical anisotropy is much lower than that of mDNB and it was thought to be a more suitable material for change of orientation. However, the result was negative in this case too.

Finally, large transverse temperature gradients were obtained by a further modification of the miniature furnace. A schematic diagram of the apparatus is shown in Fig. 3.18.

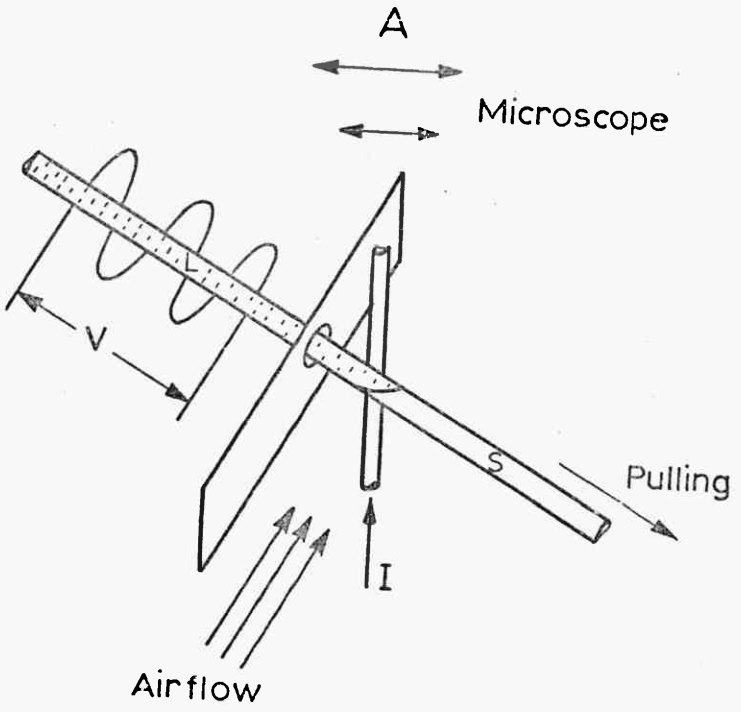

Fig. 3.18. Schematic diagram of the miniature furnace modified to produce large transverse temperature gradients.

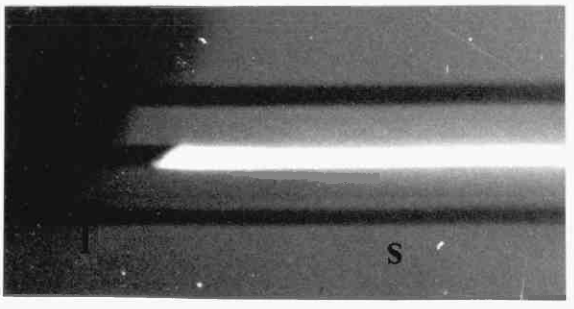

Fig. 3.19. Photograph of the solid-liquid interface obtained using the apparatus shown in Fig. 3.18, observed between crossed polars.

The heater consisted of a thin (D ≃ 100 μm) tungsten wire, located vertically between two glass slides. The fibre was in contact with the wire from one side of its cross-section and was pulled horizontally with a pulling apparatus similar to that shown in Fig. 3.7. By passing an electric current through the wire, the fibre was heated from one side and was cooled by a continuous flow of air from the opposite side (Fig. 3.18). In this experiment, unlike the previous ones, the direction of the resultant temperature gradient could be found by observing the shape of the solid-liquid interface. (Under equilibrium conditions the interface is perpendicular to the temperature gradient.) A photograph of the resultant solid-liquid interface is shown in Fig. 3.19. The shape of the interface was readily adjustable by changing both the rate of the air flow and the heating current. In this way the angle between the normal to the interface, under equilibrium conditions, and the fibre axis, could be varied in the approximate range of 0-60^{o}.

A mDNB filled fibre was melted a few centimeters from one end, and recrystallization was carried out under the conditions described above. It was observed that as the growth proceeded the z-axis of the crystal gradually tilted from the axis of the fibre. The gradual change of orientation in a typical specimen is schematically shown in Fig. 3.17b. In this way the orientation of the z-axis of mDNB was tilted upto 40^{o}. This angle varied with the growth conditions used, as described below. However, it was found that the tilting direction was opposite to that predicted by the model presented in Section 3.7 (compare Fig.3.17 a and b).

The experiment was repeated about 20 times under different conditions and the tilting direction was found to be the same in all cases.

The pulling rate was found to be the most important factor in determining the tilting angle. For a constant temperature gradient, tilting increased at higher pulling rates. At very low pulling rates (10 mm hr^{-1}), the rotation was zero or only a few degrees within the full course of pulling ($\simeq$ 2cm). Tilting angles of upto 40^{o} were achieved with manual pulling at an approximate rate of 10 mm min^{-1}. It was also observed that tilting angle at low pulling rates was enhanced by a very fast pulling of the fibre for a short distance ($\simeq$ 1mm), at the beginning of the process.

The shape of the interface also changed with pulling rate. As illustrated in Fig. 3.20 a-c, the interface became more inclined when higher pulling rates were employed.

Similar experiments were carried out for benzil, and the results were mainly similar to the case of mDNB. However it appeared that a higher average manual pulling rate was needed for benzil to be tilted in orientation as much as a mDNB specimen. In both cases the effect was much more pronounced in fibres of larger diameter; virtually no rotation effect was observed in fibres of <20 μm i.d.

Thus it was concluded that it is possible to alter the naturally preferred orientation of a fibre grown crystal by controlling the direction of the temperature gradient at the interface. However, since the rotation of the orientation took place gradually along the specimen, the crystals obtained

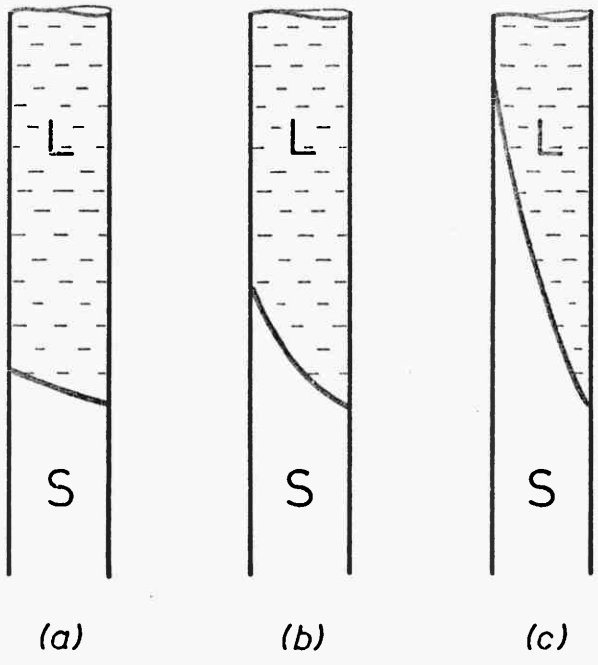

Fig. 3.20. Illustration of the variation in the shape of interface with pulling rate. Pulling rate increases from a-c.

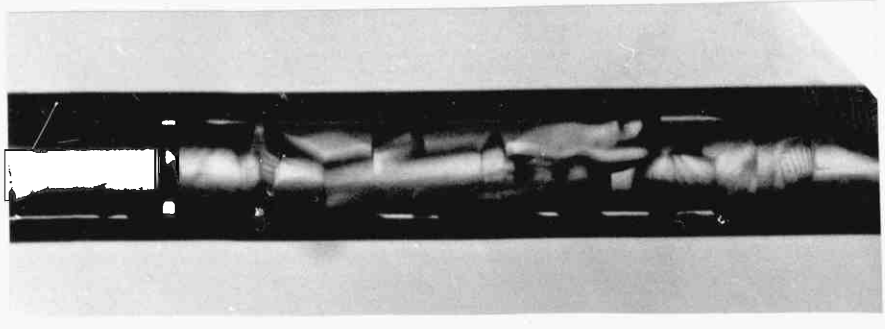

Fig. 3.21. Photograph of a coarse-grain polycrystalline fibre.

were of poor optical quality owing to the presence of many micro-cracks. Although little attempt was made to enhance the optical quality of these crystals (such as designing a furnace with a longer pulling capability), it follows from the mechanism presented in Section 3.9.2 that it should be difficult to obtain crystals of acceptable quality by this method.

3.8.2 Control of the crystal alignment by seeding

In conventional methods of crystal growth, to obtain a crystal of desired orientation, the growth is usually initiated on a seed of the required orientation. A similar seed introduction in fibre growth is difficult, but benefitting from the direct observation of the growth process, this became possible using the following simple technique. It was mentioned in Section 3.1 that crystallization of a highly supercooled liquid results in a fine-grain polycrystalline solid. The size of the grains increase by decreasing the degree of supercooling, and it was possible to obtain grain sizes comparable with the internal diameter of the fibre (Fig. 3.21).

A mDNB fibre crystallised with coarse grains was placed in the miniature furnace operating on the stage of a polarizing microscope. The fibre was melted a few cm from one end and the microscope was focussed on the solid-liquid interface. The orientation of the grains near to the interface were examined by checking the extinction angles by rotation of the stage. In this way, a grain of the desired orientation could be chosen and the interface

moved until it was adjacent to this grain. The position of the interface could be controlled by manual manipulation of the pulling apparatus. Normal pulling was then started, and the crystal adopted the orientation of the chosen "seed" grain. With this technique crystals of mDNB with their z-axis inclined upto 60^{o} with respect to the fibre axis could be obtained. The growth conditions are described below.

The technique was also applied to mNA and mDHB and the results in both cases were better than that for mDNB. In fact, the orientation of mDHB could be altered upto 80^{o} in this way.

The progress of the interface was carefully studied during the growth. In all of the materials used, the maximum achievable rate for good quality growth sharply decreased as the orientation of the c-axis of the crystal differed more from the fibre axis. This was more pronounced in the case of mDNB where a decrease from 10 mm min^{-1} to 10 mm h^{-1} was determined for an orientation difference of about 45^{o}. If a higher pulling rate was used the interface lagged behind, and the supercooling of the adjacent liquid was enough to allow spontaneous nucleation in a more favourable orientation. This nucleation always occured on the solid liquid interface, and the crystal then grew rapidly until the new solid-liquid interface reached its equilibrium position.

When the orientation of the seed was more than 70^{o} from the preferred one (mDNB), the crystal grew only for a length comparable with the cross-section of the fibre and then the growth rate dropped, practically, to zero.

The decrease in the permitted growth rate of mDHB on change of crystal orientation was not so prominent, and

even for 80^{o} orientation changes growth rates upto about 5 mm hr^{-1} were achievable. Considering also that the growth rate of mDHB in its preferred direction was evidently lower than that for mDNB under similar conditions, it can be concluded that the anisotropy of the growth rate in mDHB for a given supercooling is much smaller than that for mDNB (so is its optical anisotropies, see Table 3.1).

Conditions for the growth of a crystal with a non-preferred orientation were improved by decreasing the internal diameter of the fibre. For a constant departure from the preferred orientation, a crystal could be "forced" to grow at a higher rate in a smaller diameter fibre, without the occurrence of spontaneous nucleation at the solid-liquid interface. This can be explained by considering that the probability of nucleation is proportional to the area of the interface.

In these experiments the temperature gradient was parallel with the fibre axis or nearly so. Thus the normal to the solid-liquid interface was also expected to align with this direction in all cases. However, this was only true if the crystal was growing in its preferred orientation. Otherwise, the normal to the interface rapidly became tilted and assumed an angle δ with respect to the fibre axis when pulling was started. The transition of the interface shape is schematically shown in Fig. 3.22 a-d. The interface could maintain any of the shapes 3.22 b-d depending on the pulling rate and the deviation of the crystal from its preferred orientation. When pulling was stopped the original equilibrium shape of the interface (Fig. 3.22a) was regained within a period of time which varied from seconds to more than half an hour depending on the orientation of the growing crystal.

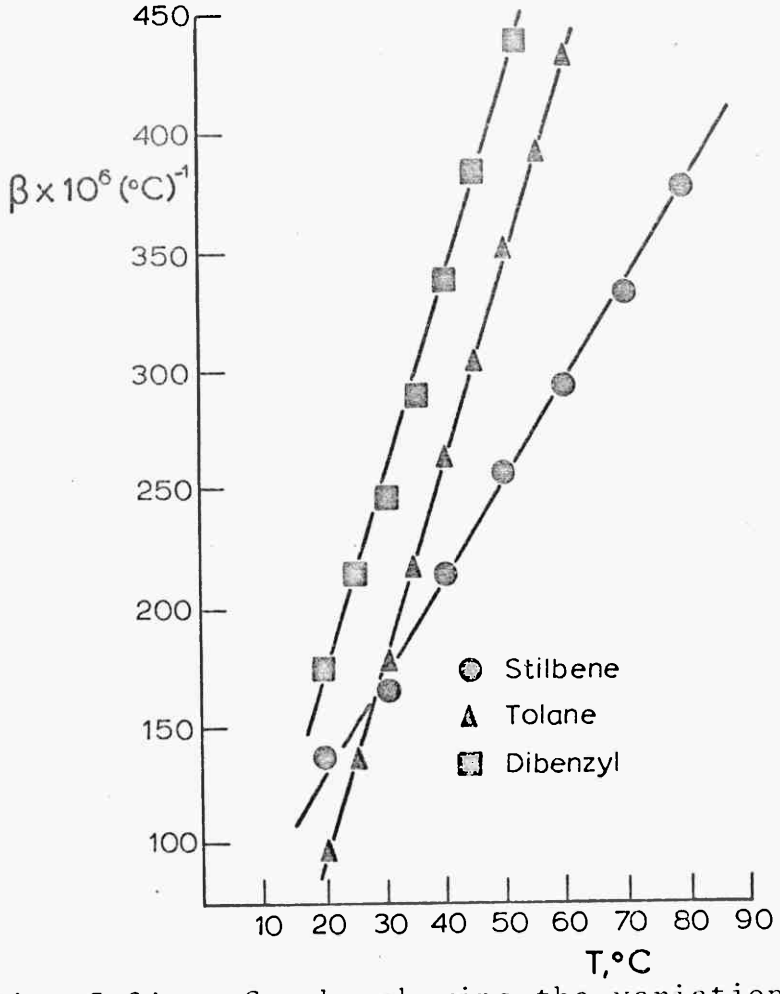

Fig. 3.24. Graphs showing the variation of volume expansion coefficient with temperature in three organic crystals.

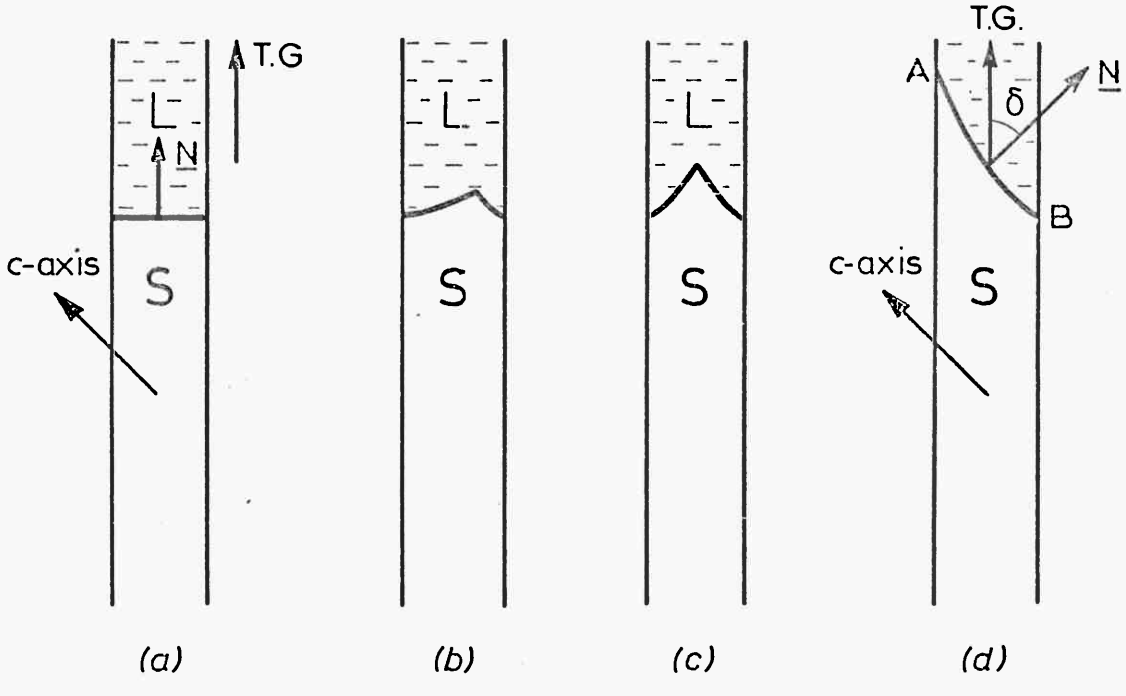

Fig. 3.22. Illustration of the change observed in the interface shape at the start of growth; c-axis of crystal inclined to fibre axis.

From a qualitative comparison between Fig. 3.17b and Fig. 3.22d it can be concluded that the relative positions of the z-axis of the crystal, the fibre axis, and the normal to the interface is the same in both cases. Hence, although the experiments described in Sections 3.8.1 and 3.8.2 were essentially different in nature, it seems reasonable to argue that the observed phenomena may well be related in origin. That is to say, in the former set of experiments a rotation of the interface plane altered the orientation of the crystal and in the latter, vice versa; in summary:

$$\text{crystal orientation} \underset{\longleftarrow}{\xrightarrow{\text{growth conditions}}} \text{interface shape}$$

Thus, a single mechanism appears to exist based on which the above reaction could be explained in both directions. This is further discussed in the following Section in connection with anisotropy of the growth rate of the crystal.

The main purpose in these experiments was to study the growth mechanism, and no attempt was made to grow crystals longer than ~ 1 mm. However it was apparent that the method could yield good quality crystals of different orientations. For this purpose the furnace would need to be redesigned, and in particular a pulling apparatus capable of adjustment over a wide speed range provided.

3.9 Discussion

The experimental progress in fibre growth presented in this Chapter, was mainly based on the observations carried out using the miniature furnace. In this Section, attempts are made to explain the observed phenomena in terms of the various properties of the materials grown, and the experimental conditions used.

3.9.1 The occurrence of the voids

The observed mechanism of formation for the separation between crystal and the glass cladding was described in Section 3.3, and is schematically illustrated in Fig. 3.23. The fact that these voids occured well beyond the interface (for small temperature gradients) indicates that the volume decrease on solidification had no significant role in their formation. Thus it is more likely that the volume contraction of the solid from melting point to room temperature is responsible. However, the thermal expansion coefficients of the materials used were not large enough to explain the occurrence of voids as large as those shown in Fig. 3.6 a-c. For example, the coefficients for mNA are given as (Ayers et al., 1972):

$$a_{11} = -40\times10^{-6}$$
$$a_{22} = 150\times10^{-6} \qquad (^{o}C)^{-1}$$
$$a_{33} = 108\times10^{-6}$$

Assuming that the thermal expansion coefficients are independent of temperature, the volume contraction of solid

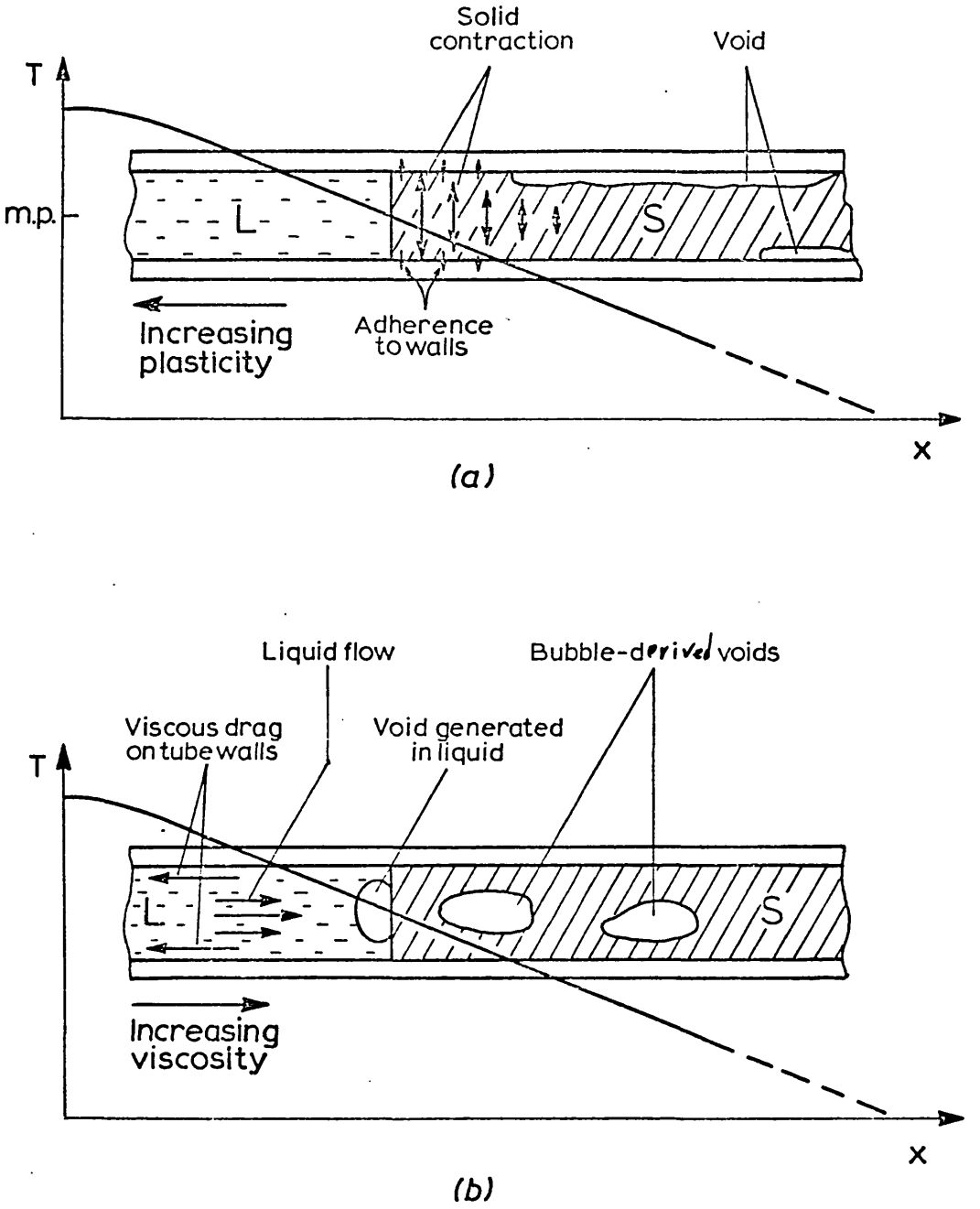

Fig. 3.23. Illustration of the dominant void formation mechanisms, (a) between the crystal and cladding, (b) bubble-derived voids.

mNA from the melting point (112°) to room temperature is, then about 2.0%. For comparison, the volume density of the voids reported to be about 10% in mNA filled fibres (Stevenson, 1977). It can also be deduced from Figs. 3.6 a-c that the void density is higher than 2% even in mDNB, which showed a lower tendency to void formation than mNA.

Thermal expansion coefficients of benzil at room temperature are reported (Winchell, 1954) to be 9.5 and 5 times of that of platinum in the z- and the x- and y-directions respectively. That is to say

$$a_{11} = 85 \times 10^{-6} \qquad (^{o}C)^{-1}$$
$$a_{22} = a_{33} = 45 \times 10^{-6}$$

The predicted volume decrease from melting point (95°) to room temperature is ~1.3% which is close to that obtained for mNA and hence does not explain the large difference observed in the void density between these two materials.

Furthermore, voids occurred when the solid was not more than 15°C below the melting point, and the void density then did not alter appreciably on further cooling. Also the shape and irregular distribution of voids along the fibre (Fig. 3.6 a-c) suggests that they mainly occurred when the solid had been highly plastic.

It seems that the only explanation of the above observations is that in the materials used the volume expansion coefficient at or near to the melting point is upto an order of magnitude (mNA) higher than that at room temperature. Unfortunately, the necessary data were not available. However, variation of the volume-expansion

coefficients of stilbene, tolane and dibenzyl (melting points of 124.2, 63.5 and 52.2°C respectively) have been studied by Koreshkov (1965). The results given are plotted in Fig. 3.24, showing that the volume expansion coefficient of tolane, for example, at its melting point is ~5 times higher than that at room temperature. Another example is succinic acid (m.p. = 188°C) whose thermal expansion coefficient (a_{11}) measured in the temperature range of 20-130°C is 6 times higher than that measured in the range of -180-20°C (Amoros et. al., 1965). Furthermore, Fig. 3.24 shows that, although at room temperature the expansion coefficient of stilbene is ~2 times higher than that of tolane, at higher temperatures the situation reverses. Thus the volume contractions calculated for mNA and benzil cannot even comparatively represent their tendency for void formation.

The formation mechanism for bubble-derived voids was described in Section 3.6.1. The bubble itself was generated at the solid-liquid interface when the liquid flow towards the interface was insufficient to compensate for the volume contraction which occurred on solidification.

It can be argued that if all of the volume shrinkage occurred at the interface no voids would form since liquid would move towards the interface to compensate for the volume contraction. In practice, a temperature/distance step function cannot be achieved and for small temperature gradients it is clear that the liquid will increase in viscosity as the interface is approached, and that the thermal contraction in the solid will increase with distance from the interface (see Fig. 3.23 a & b). Each of these conditions will lead to the formation of voids of the appropriate types described above.

By increasing the temperature gradient at the interface to as large a value as is practically possible, the formation of both types of void would be reduced, since in one case the total viscous drag in the liquid would be minimized, and in the solid the thickness of the region where the material is still plastic is also minimized and the strain caused by thermal contraction is more likely to be relieved by slip processes.

It was shown that the volume shrinkage substantially occurs at about the melting point. The materials used were found to be very soft in this temperature region; for example, in two cases movement of large bubbles was observed within lengths of solid at about $5^{o}C$ below the melting point (mDNB), and subsequent examination of these crystals revealed no sign of optical imperfection due to these incidents. Hence if the thickness of this region beyond the interface is short enough, thermal contraction in all orientations is likely to be compensated for by slip processes.

The stress caused by volume contraction occurring in the soft region beyond the interface can be relieved either by separation from the glass wall (void formation) or by slip processes. When separation occurs, the driving force for slip vanishes; but, the resisting force against this separation is the adherence of the material to the glass wall. When the adherence is catastrophically overcome at a point on the wall, the separation propagates for a long distance, as described in Section 3.3. The later the separation occurs, the more time is available for slip processes to compensate for the volume contraction, and the smaller the resulting cavity will be. This clearly explains

the wedge shape of the long voids (Fig. 3.6. c) where the thicker end of the wedge points towards the growth direction.

By decreasing the temperature (i.e. going further from the interface) the plasticity of the solid decreased while the contraction of the solid continuously increased, and it seems that eventually separation must occur. However if this was delayed until the solid was hard enough to maintain its cylindrical shape, the conditions of void formation would be totally different. The radial depth of the resulting cavity can easily be calculated by considering two concentric cylinders of different thermal expansion coefficients. As an example, in the case of benzil and pyrex glass we have:

$$\Delta r = (a_{22} - a_{pyrex}) \cdot \Delta T \cdot D$$

where

Δr = radial depth of the cavity;

a_{22} = average thermal expansion coefficient of benzil in x and y directions, in the temperature range quoted below;

a_{pyrex} = thermal expansion coefficient of pyrex glass;

ΔT ≃ from 15 degrees below melting point to room temperature;

and D = internal diameter of the fibre.

Assuming, for the sake of argument, that the average value of the thermal expansion in this temperature range is equal to that at room temperature, results in:

$$\Delta r \simeq (45 \times 10^{-6} - 3.3 \times 10^{-6})\ 60 \times D$$

Hence for a fibre of 30 μm i.e.

$$\Delta r \simeq 7.4 \times 10^{-2}.\mu m$$

Such a separation could not be optically detected, and also could further be minimized by using more suitable glasses as cladding. Therefore, it seems that the effects caused by thermal contraction in the temperature range mentioned will not produce unacceptable alterations in the configuration of the device.

From the above considerations it is concluded that in favourable growth conditions, the void free "fibre grown" crystals are free from any major stresses. This is in agreement with the X-ray examination results.

Furthermore, it has been reported by Morris et al. (1968) , that the dislocation density of phenyl-2-hydroxybenzene (salol) crystal drastically decreases as it grows along capillary tubes with diameters of the order of 1 mm, and it has been explained that dislocations grow out to the walls as growth proceeds. It can also be deduced from the given data that the effect should be more pronounced in smaller diameter fibres. Although the reported growth conditions are different from the ones employed in the present work, the much smaller diameter tubes used, suggest that the fibre grown crystals obtained were of low dislocation density, if not dislocation free.

It should be possible to relate a probability to the occurrence of the catastrophic separations (discussed above) - under each set of conditions; this should relate to the randomness of the distribution of the voids along the fibre. It is obvious that this probability will be proportional to the area of attachment, just as the probability of nucleation increases with increasing surface area. Hence the separation is more likely to occur in larger diameter

fibres, in which the wall area per unit length is larger; and furthermore, the resulting cavity should be larger due to the larger volume/surface ratios.

It follows that the tendency for formation of the voids originating from thermal contraction of the solid, is higher in fibres of larger internal diameters. On the other hand bubble generation at the interface will clearly be enhanced in very small capillaries where the viscous drag will hinder flow towards the interface. Thus, depending on the the viscosity of the liquid under the growth conditions used, on the variation of the thermal expansion coefficient and plasticity of the solid at temperatures between the melting point and room temperature, and on the adherence of the solid to the glass wall and its variation with temperature, there is likely to be both an upper and lower limit to the size of the fibres that can be filled in a void-free condition for a given temperature distribution along the fibre.

Both processes of void formation are less likely to occur if the growth is slow and more time is allowed for viscous flow and plastic deformation to relieve strain conditions arising in the liquid and solid regions. On the other hand it can be argued that by allowing longer times (i.e. lower pulling rates), the probability of the initiation of a solid-glass separation by environmental influences (e.g. vibration) will increase, resulting in more voids. Experimentally, a decrease in the tendency for bubble generation in the liquid by decreasing the pulling rate was apparent, but no firm idea of the variation of the density of the crystal-glass separations with pulling rates was obtained.

3.9.2 Auto-alignment of the fibre grown crystals

At an earlier stage of this work attempts were made to describe the auto-alignment of the crystal obtained with regard to the anisotropy in thermal conduction of the respective materials (Section 3.7). Although the model, at the time, could explain the experimental observations, it was later found to be in disagreement with the results of further experiments (Section 3.8.1).

In this Section an attempt is made to explain the observed effects by the anisotropy in the growth rate, that is, by considering the large difference which exists between the growth rates for different crystal orientations under similar growth conditions.

If crystal growth within a fibre was started from a highly polycrystalline seed or by spontaneous nucleation, obviously the orientation adopted by the crystal after a short length should be that which allows the growth rate to equal the pulling rate. Otherwise if an orientation of a lower growth rate formed, the solid liquid interface would lag behind and the supercooling in front of the interface would eventually become sufficient to cause nucleation in a more favourable orientation (see Fig. 3.25). This effect was observed and was reproducible (Section 3.8.2). However if the orientation adopted was the maximum growth rate direction of the crystal, no improvement can result from re-orientation. If the growth rate is too large, supercooling in front of the interface can still result in polycrystalline growth.

Thus, at lower pulling rates there is a chance of survival for crystals with orientations other than the preferred one. This would depend on the degree of the growth rate anisotropy, the pulling rate and the diameter of the fibre. Using a constant pulling rate, in a material of low growth rate anisotropy, crystals with a large inclination to the preferred orientation can be grown. Also in smaller diameters the chance of survival for a non-preferred orientation would increase since the probability of renucleation will be proportional to the area of the interface.

All of these considerations are in agreement with the experimental results: crystals of mDNB were persistant in adopting their preferred orientation, and large deviations from this orientation were only observed in very small diameter fibres. The achievable growth rate of this crystal parallel to its c-axis proved to be very much higher than the two other principal orientations. Benzil on the other hand showed large deviations from the preferred orientation and showed a much smaller difference in growth rate between the various orientations.

Considering the experimental results presented in Section 3.8.2, let a length of fibre grown crystal with an arbitrary orientation be placed in a furnace where it experiences a temperature gradient parallel to its axis. At zero pulling rate and equilibrium conditions, the normal to the solid-liquid interface ($\underline{N}$) is parallel with the fibre axis (Fig. 3.22a). On starting to pull, however, the crystal will tend to grow in its maximum growth rate orientation, inclined to the fibre axis (Fig. 3.22b and c) and hence the shape of the interface and the direction of $\underline{N}$ will

generally change (Fig. 3.22d). Thus $\underline{N}$ would be parallel to the fibre axis only if the c-axis of the crystal is also aligned with this direction.

Considering the experimental results presented in Section 3.8.1, let a fibre grown crystal, whose preferred orientation is aligned with the fibre axis, be exposed to an inclined temperature gradient as shown in Fig. 3.26 (e.g. using the hot wire and air flow method). At zero pulling rate $\underline{N}$ is parallel with the temperature gradient and hence inclined to the fibre axis. On starting to pull it was observed that $\underline{N}$ further inclines, and this effect increases with pulling rate (Fig. 3.20). This can readily be explained considering the mechanism of the apparatus: As the pulling rate is increased the exposure time of each section of fibre to the heating wire and cooling air flow decreases, and hence these effects become more localized on the opposite sides of the fibre. Thus the actual temperature gradient experienced by the material inside the tube becomes more inclined to the aixs. This effect would obviously be weaker in fibres of smaller diameters, which have smaller thermal capacity.

The transition in the interface shape is shown in Fig. 3.20 a-c; also in Fig. 3.26 planes A and B are the approximate interface shapes before and after the start of pulling respectively, thus the crystal must grow and fill the space between A and B during the transition time. It may be deduced from the earlier discussions, that in filling this cavity, the maximum growth direction of the crystal will tend towards the cold wall of the fibre. To clarify the matter, let the pulling start with a sudden jump; the volume between A and B is then filled with supercooled liquid.

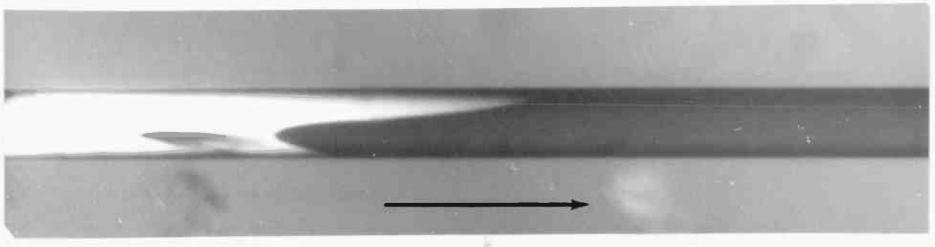

Fig. 3.25. Photograph, showing the change of crystal orientation to a preferred direction (benzil); observed between nearly crossed polars.

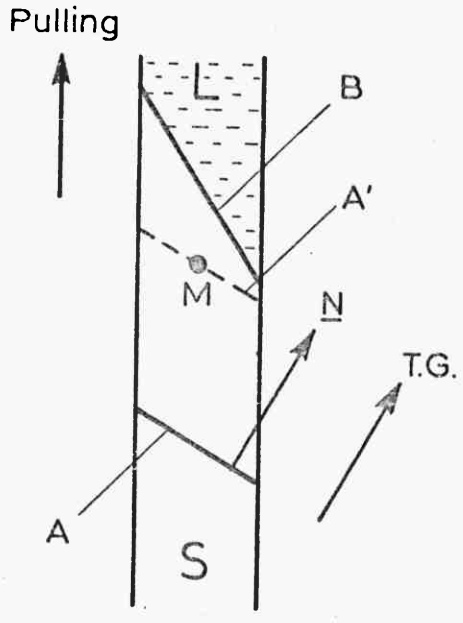

Fig. 3.26. Illustration of the mechanism altering the growth orientation due to a temperature gradient inclined to fibre axis.

Considering the transition of the interface from A to B in two steps, say from A to A' and from A' to B, it is apparent that at a point on A', say M (Fig. 3.26) there will be a tendency for growth towards the colder wall. This tendency should excite the creation of low angle grain boundaries, where in the new grain the c-axis is more inclined from the fibre axis.

It is easy to understand that if this transition of the interface takes place slowly, i.e. the pulling rate is increased gradually from zero to its final value, it is unlikely to cause any rotation of the crystal orientation. At the other extreme, if pulling was done in successive sudden jerks, at each step the mechanism discussed would operate and the resulting deviations will be additive. This is in agreement with the observed results: The maximum deviations were obtained when the pulling was done by hand and in discrete jumps. However, although no orientational rotation is predicted for the case of continuous pulling, small deviations were observed experimentally. From the above proposed mechanism, the crystals grown in this way should be highly stressed; and in fact none of the crystals obtained with this method were of acceptable optical quality (Section 3.8.1).

3.10 Conclusion

A qualitative study of the fibre growth technique was presented in this Chapter. It was shown that by optimization of the growth conditions, the main problems encountered with the preparation of defect-free crystal cored fibres can

be solved, and the preparation of long lengths (up to 4.5 cm) of void-free fibres was reported.

A miniature apparatus was designed which allowed direct and detailed observation of the growth, and in this way mechanisms of void formation were formulated and related to the conditions of growth and the properties of the materials.

CHAPTER 4

CRYSTAL CORED OPTICAL FIBRE (CCOF)

4.1 Light Propagation in CCOF

The most important feature of a CCOF is, of course, light guidance. It is of primary importance for any device application that a CCOF should provide light transmission without major scattering and with a low level of attenuation for lengths upto 1 cm.

The theoretical study of the light propagation in a CCOF was presented in Chapter 1. The experimental work in this respect was carried out with benzil-Pyrex CCOF. According to Section 1.8.1 and using Table 3.1, for such a fibre at 633 nm:

$$n_x = n_y = n_1 = 1.651,$$
$$n_z = 1.674 \quad \text{and}$$
$$n_2 = 1.471$$

Conditions for validity of weakly guiding and weakly anisotropic approximations are (Section 1.8.1) $(n_1-n_2)/n_1 \ll 1$ and $(n_z-n_1)/n_1 \ll 1$, respectively. Substituting the abovementioned values yields:

$$\frac{n_1-n_2}{n_1} = 0.11 \qquad \text{and}$$

$$\frac{n_z-n_1}{n_1} = 0.014$$

Thus according to Section 1.8.1 the propagation characteristic of such a fibre is approximately similar to that of an isotropic

optical fibre with a core refractive index n_1. Then the V value can be calculated from Eq. (1.2.3)

$$V = \frac{2\pi a}{\lambda}\sqrt{n_1^2 - n_2^2} \simeq 150$$

where the internal diameter (2a) of the fibre used was ~40 μm. The number of guided modes which can be supported by the guide is then (Section 1.2.)

$$N = \frac{V^2}{2} = 1.1 \times 10^4$$

and hence the fibre in question is highly multimode.

Regarding the connection of a CCOF to a fibre-optic system, it is advantageous to design a CCOF so that its V value is about the same as the optical fibre used. The difference between core and cladding refractive indices in commercial multimode optical fibres is of the order of 0.01 and hence their V values (assuming the same core diameter) are proportionately less than that for benzil-Pyrex CCOF. This situation can be enhanced by using a glass of higher refractive index for cladding.

For observation of light propagation in a benzil-Pyrex CCOF, an ~4 cm length was cut and suitable ends were prepared (see next Section). The fibre was then placed on a glass slide of ~ 3 cm length so that ~ 0.5 cm of the fibre from each end was off the slide; and then immersed in a liquid of higher refractive index than cladding by spreading a small amount of the liquid on the slide. This was then mounted on a three dimensional micromanipulator on an optical bench where light from a 1 mW He-Ne laser could be launched

into the core from one end of the fibre using a x30 objective lense. A microscope was positioned vertically on the bench so that it provided a transverse view of the fibrewith a x50 magnification.

The light scattered by the imperfections of the guide (Section 1.3) was observable through the microscope when observations were carried out in a dark room. By examination of different fibres with various kinds of imperfections it was concluded that any optically detectable void causes scattering and hence interferes with propagation. Other imperfections such as cracks or grain boundaries also caused scattering. It was observed that the presence of a point of imperfection not only causes scattering at that point but also increases the level of scattering for some distance. (comparable with the diameter of the fibre) beyond this point. This is very likely to be due to the coupling (Section 1.3) to the leaky modes (Marcuse, 1974) caused by the presence of the void. Also, a continuous scattering all along the fibre was observable which was of a higher level in fibres grown by faster pulling rates. In void-free fibres grown by the method described in Section 3.5 using pulling rates of 4 cm hr^{-1}, the scattering was minimal so that the core was hardly observable under the microscope. In Fig. 4.1 propagation in a fibre with a low void density is compared with that in a void-free fibre.

Attenuation of optical fibres is usually measured using long lengths of fibre (a few km), which allows cutting the fibre in steps without disturbing the launching conditions. With lengths of only upto 4.5 cm, the attenuation of CCOF could not be measured in this way since on each cutting both the launching conditions and quality of the end changed.

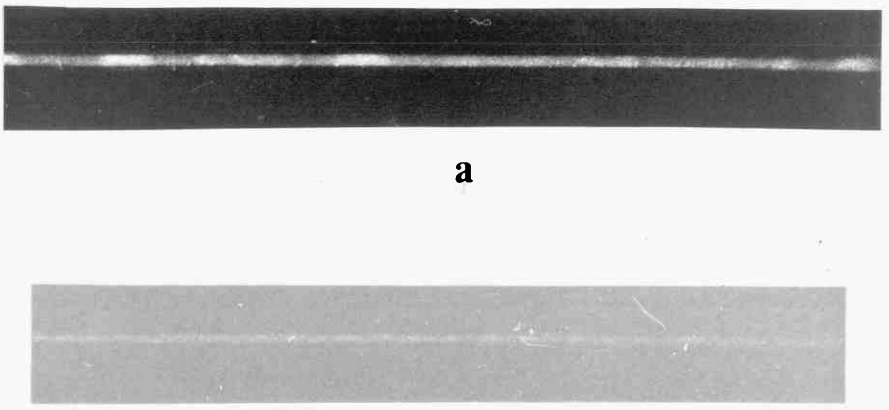

Fig. 4.1. Light Propagation in, (a) a low void density CCOF, (b) a void-free CCOF (benzil-Pyrex)

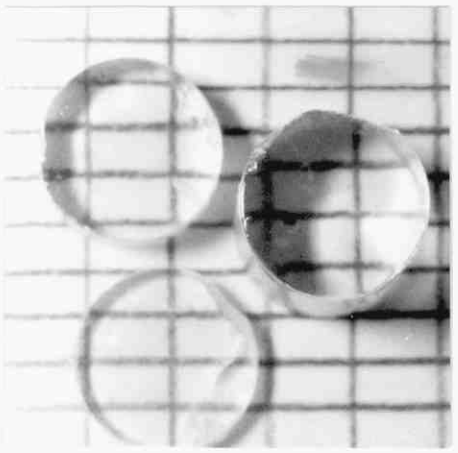

Fig. 4.2. Benzil crystals used for attenuation measurements.

However, it was shown above that scattering losses in a void-free fibre were minimal, thus according to Section 1.6, the attenuation of the fibre should be nearly equal to the absorption of the crystal core. In order to measure the latter, a bulk single crystal of benzil was grown by Bridgman technique (growth conditions: T_1 = 110°C, T_2 = 60°C and pulling rate = 2mm hr^{-1}). The crystal obtained had a diameter of 1 cm and length of ~10 cm. This was extracted from the container and cut into 4 pieces of different lengths with a wet string saw. Optical faces for each sample were prepared by conventional techniques. A photograph of the samples obtained is shown in Fig. 4.2. Although it is reported (Chandrasekhar, 1954) that crystals of benzil grown by Bridgman technique usually are oriented with their c-axis parallel to the growth direction, unfortunately,in the crystal grown the c-axis was inclined ~50° to the growth direction. The c-axis was identified by the perfect cleavage presented by the crystal perpendicular to this orientation (Winchell,1954).

The transmission spectrum of the material was recorded by a spectrophotometer (Perkin Elmer, Model 237) using a sample of 3.9 mm thickness. The result, in the wavelength range of interest, is shown in Fig. 4.3, which indicates that the minimum attenuation of the crystal occurs at 1.2-1.3 μm which is, as shown in Chapter 1, the optimum wavelength range for optical communications.

The absolute value of attenuation, however, was measured at 633 nm only. For this purpose light from a 1 mW He-Ne laser was passed through 4 samples of different thicknesses

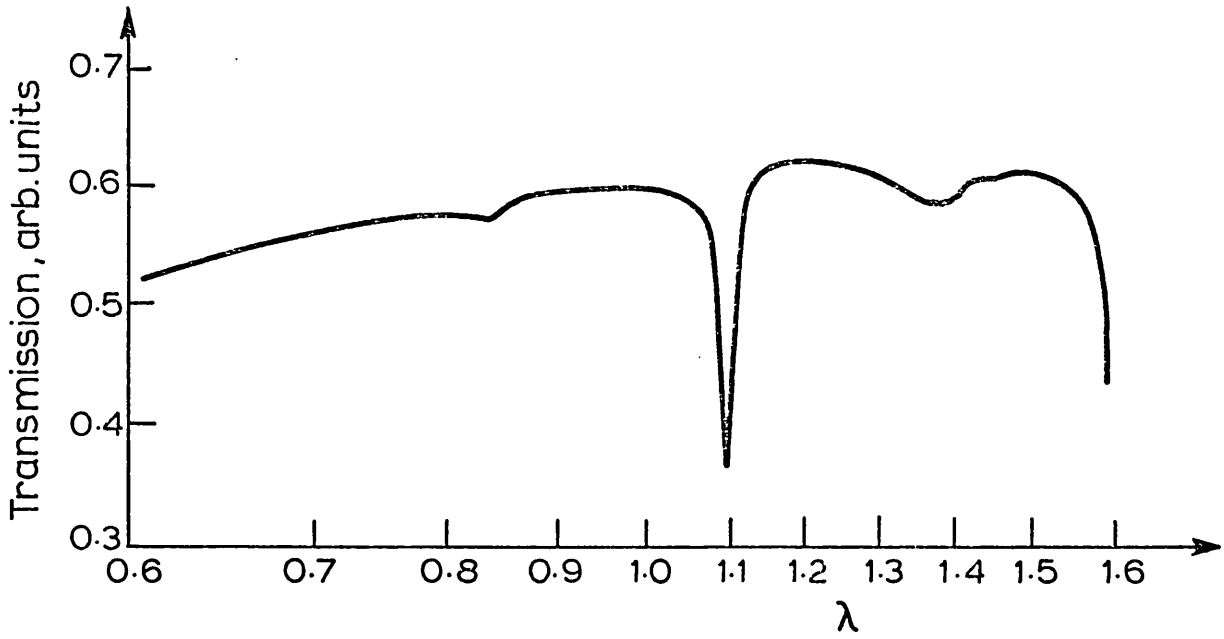

Fig. 4.3. Transmission spectrum of benzil.

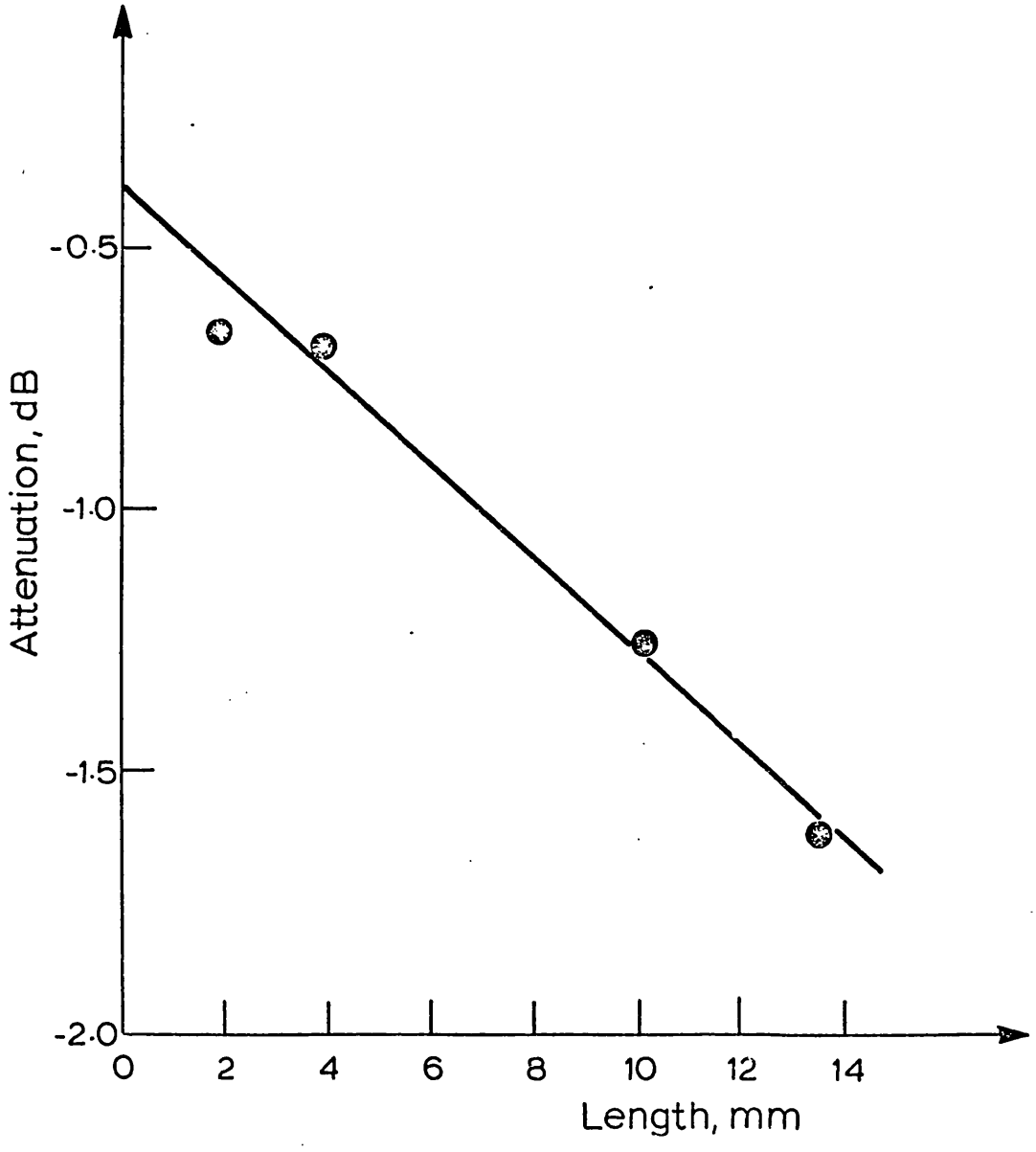

Fig. 4.4. Plot of total loss vs. length of the sample (benzil).

(1.91, 3.93, 10.24 and 13.50 mm respectively) and the transmitted light was measured by a light meter (Laser Associates Ltd., Model 43). Results are given in Fig. 4.4 where the attenuation in dB is plotted against the length of the sample. From the slope of the line, the value of 0.89 dB cm^{-1} is obtained for the attenuation of the crystal which is to a good approximation, the attenuation of the related CCOF. It is clear from Fig. 4.3 that lower values should be obtained for the range of 12-13 μm. This level of attenuation is well below the attenuation of the waveguides widely used in integrated optics, for instance that of a $LiNbO_3$ - $LiTaO_3$ slab waveguide is ~3 dB cm^{-1} (Kaminow, 1975). This presents an additional advantage for CCOF over waveguides employed in the field of integrated optics.

4.2. End Preparation and Jointing to Optical Fibres

One of the obvious difficulties encountered with the experimental utlization of CCOF stemmed from the fact that no good quality fibre ends could be prepared by the cutting methods well known in the fibre optic field. A typical pair of ends usually obtained for mDNB-cored fibres is schematically shown in Fig. 4.5a. The situation was somewhat better in benzil owing to its cleavage in the plane perpendicular to its c-axis.

Eventually good quality ends were obtained by the method schematically illustrated in Figs. 4.5 b-d. The fibre was vertically mounted on the stage of a low magnification stereoscopic microscope. A small fragment of material

(dimensions smaller than the fibre cross-section) was placed on the top end of the fibre. Then a fine wire (heated by passage of a large electric current) was introduced from above. Conditions were carefully controlled, by observation through the microscope, so that the piece of material and only a short length of the crystal core were melted. The molten material filled the empty section at the fibre end, and on slowly lifting the heater, was crystallized assuming the orientation of the crystal core. The end was then lapped and polished using a polishing paper wetted by a water-ethanol mixture. The process was then repeated for the opposite end of the fibre. Good fibre ends resulted from this technique. The quality of the ends obtained in the case of mDNB deteriorated in air within days but no major deterioration was detected in benzil.

The following method was used for making permanent connections between a glass fibre and a CCOF of the same diameter. An as-cut CCOF was aligned with a glass fibre on three pieces of glass slides arranged as shown in Fig. 4.6, on a microscope stage. A relatively large fragment of the material (dimensions of ~1 mm) was placed at the joint which was melted as the heater gradually approached from the glass fibre side. The melt filled the cavity formed between the fibres and formed a droplet on the joint. On removing the heater crystallization was started from the crystal core, and hence the crystal adopted the orientation of the core. A single crystal was formed within the cavity between two fibres, but the rest of the droplet polycrystallized. Thus the joint was surrounded by polycrystalline material, protecting it from environmental influences. The arrangement

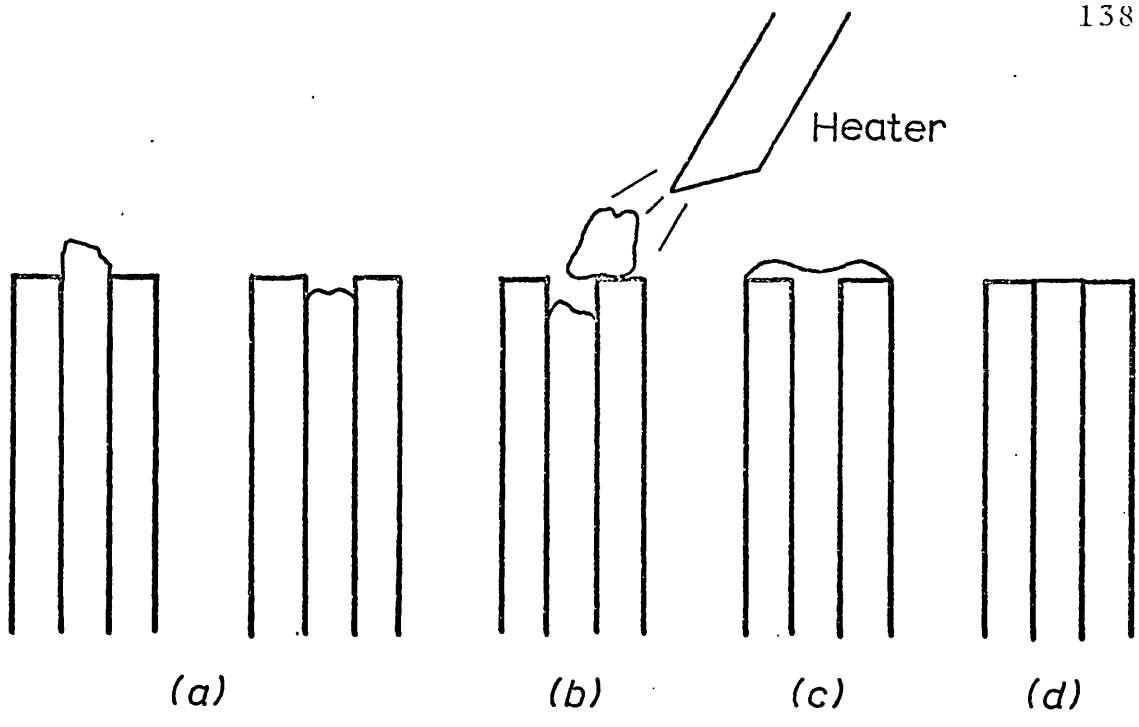

Fig. 4.5. Illustration of the method used for end preparation.

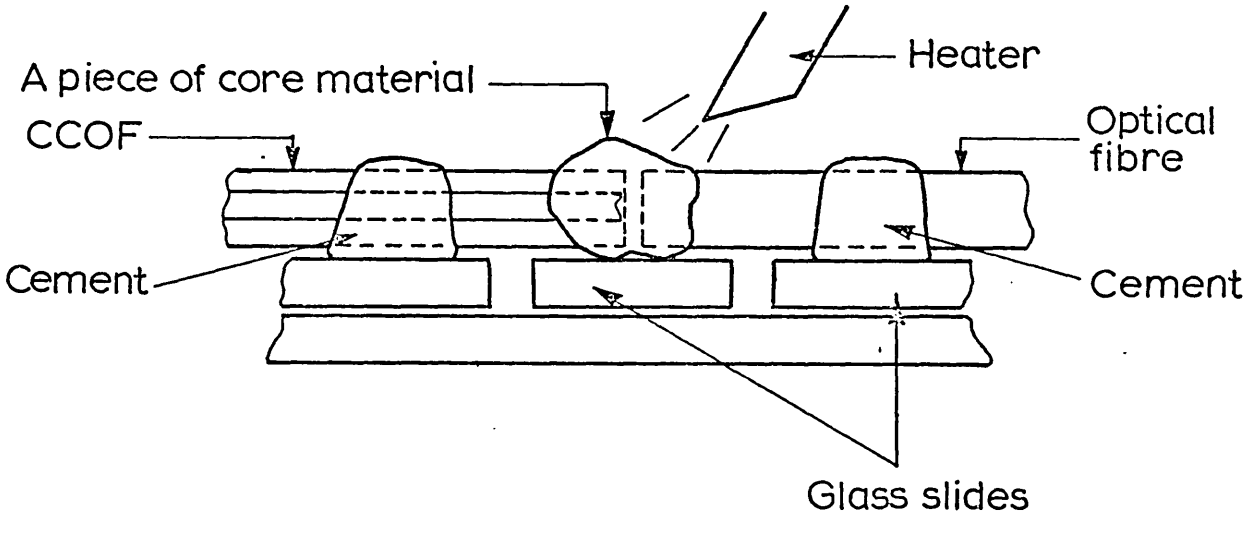

Fig. 4.6. Illustration of the method used for connecting a CCOF to a glass fibre.

of three pieces of glass slide shown in Fig. 4.6 was utilized in order to prevent flow of the liquid on the slide along the fibre due to surface tension. Both of the methods described above benefitted from the fact that in the materials used the melt could be supercooled to room temperature without spontaneous nucleation.

The method above described is proposed for manufacture of permanent optical fibre - CCOF joints. In this way the problems involved with organic materials such as deterioration of faces in the air, and their interaction with index-matching liquids could be solved.

4.3 Applications of CCOF in Non-linear Optics.

In integrated optics confined propagation of light in non-linear crystals is achieved by fabrication of slab waveguides. With the demonstration of light propagation in CCOF, another means of light guidance in such media is created. Hence it is both logical and important to consider the use of CCOF for related applications which are already established in integrated optics.

The advantages of performing non-linear optics in optical waveguides were established in Chapter 2. This matter has been the subject of many theoretical (Boyd 1972) and experimental investigations (Usugi and Kimura, 1976) and high interaction efficiencies have been reported.

For performing non-linear optics in a waveguide different modes of the guide are employed for propagation of different interacting waves so that the phase matching condition is satisfied (Section 2.3). Hence theoretically, infinitely

long coherence lengths should be expected regardless of the dispersion and birefringence of the material used. However, in practice this is handicapped by variation of the parameters of the waveguide (thickness in particular) which are inherited from the fabrication techniques employed (Goell, 1974). It has been shown that obtaining coherence lengths ≥ 1 mm (corresponding to a thickness variation of 2%) is difficult (Tien, 1971).

A similar phase matching technique is applicable for optical fibres. In this case, however, parameters of the guide can more easily be kept constant and hence longer coherence lengths can be obtained. Stolen et al. (1974) reported obtaining a coherence length of 10 cm within a silica fibre (diameter variation was 0.3%) for three wave mixing using the non-linear properties of the glass.

In a void-free CCOF the perfection of the fibre mainly depends on the hollow glass fibres used and this in turn depends on the precision of the original preform and of the drawing technique used. Hence, in principle, preparation of short lengths of void-free CCOF, similar to glass optical fibres in perfection, should be possible, and as a result long coherence lengths (i.e. $\simeq 1$ cm) could then be expected for non-linear interactions carried out in a CCOF.

Thus, in summary, CCOF has the following advantages over the thin film waveguides from the view point of non-linear optics:

(a) Optical fibre compatibility.

(b) Higher efficiency and easier technique of launching.

(c) Lower attenuation.

(d) Longer coherence length.

However, for non-linear optic applications, low moded ($V \lesssim 10$; the fibre used by Stolen et al. (1974) had a V value of ~9) CCOF has to be made, simply because in a highly moded fibre it is difficult to maintain the optical power as launched in a particular mode only, which is a preliminary to the phase matching technique described. It follows from Eq. (1.2.3) that this requires decreasing both the core diameter and the core-cladding index difference. For a benzil-Pyrex CCOF, $V < 10$ is satisfied if the core diameter is smaller than ~4 μm (at λ =1.0 μm) but, according to the results presented in Chapter 3, preparation of CCOF in this diameter range is difficult (at least in the materials studied). However using a diff erent glass so that $n_1 - n_2 = 0.01$, the core diameter range would be < 18 μm, which is easily obtainable by the method described in Section 3.5.

Regarding fibre-optic communication systems, performing non-linear optics in CCOF would provide the possibility for an experimental study of the parametric amplification of light within fibres. This has been theoretically considered by Yariv (1976,II), showing that by having short lengths of a non-linear crystal within a fibre transmission line both parametric amplification and modal phase compensation (compensation for multimode dispersion, see Section 1.5) can be achieved. This clearly points to a wider scope for future studies on CCOF.

Non-linear optics in CCOF clearly could in itself be the subject of lengthy theoretical and experimental studies. As a pilot experiment, however, the following observation was made at an early stage of the work.

Three sections of mDNB-Pyrex CCOF each with a length of 1.5 cm were cut and cemented to the edge of a glass slide as shown in Fig. 4.7. Crystals were of good quality but some voids between core and cladding were present since at that stage, the growth of void-free CCOF had not been achieved. For similar reasons the quality of the fibre ends were poor. The approximate core diameters were 30, 40 & 50 μm, respectively.

Each fibre was positioned at the centre of a 1 MW (peak power) pulsed Nd-glass laser beam using conventional techniques. With this arrangement, the power launched into the core was estimated to be of the order of 100 W. On pulsing, green light (second harmonic of invisible 1.06 μm) was observed radiating out from the sides of the fibre as shown in Fig. 4.7. A comparison between the brilliance of the green light observed and that obtained from a powder test of mDNB (see, Kurtz and Perry, 1968) indicated an enhancement of the SHG within CCOF. The brilliance increased with core diameter. The radiation pattern was sharply peaked in the forward direction so that it was virtually invisible when the direction of observation was perpendicular to the fibre axis. Similar behaviour has been reported (Rawson, 1972) for scattered radiation from optical fibres. This similarity indicated the importance of the coupling to radiation modes in the effect observed. More recent theoretical studies (private communication with B.K. Nayar) have revealed that the most probable mechanism assisting the SHG in the conditions of the above experiment is the coupling of the light generated to the radiation modes of the guide,

which should be enhanced by the irregularities of the CCOFs used.

Thus, it appears that no conclusion about the waveguide phase matching in CCOF can be drawn from the above observation. For this purpose a CCOF of V< 10 must be employed and one of the parameters of the experiment be varied (e.g. varying n_1 by changing the temperature, or tuning the fundamental frequency) for the phase matching between certain guided modes to occur (Anderson and Boyd, 1971). Clearly, further investigation of this aspect is indicated.

4.4 Optical Fibre Compatible Electro-Optic Phase-Modulator

A schematic diagram of the device proposed for phase modulation of light is shown in Fig. 4.8. It comprises a 2 cm length of mNA filled CCOF with an internal diameter of 20 μm, and it is assumed that the c-axis of the crystal is aligned perpendicular to the fibre axis or nearly so (considering the results presented in Section 3.8 regarding the orientation control in mDNB and mDHB, preparation of such a CCOF no longer seems impractical). The CCOF is connected to optical fibres using the technique described in Section 4.2, and electrodes have been painted on the sides of the cladding (using e.g. silver dag). The light launched into the CCOF is polarized parallel to the crystal c-axis.

The HE_{11} mode of the guide according to Section 1.8.2 will "see" a core refractive index (n_1) equal to n_z of mNA. Also, considering Fig. 1.3, n_{ef} for a mode of the guide is a function of V, but when $V>>V_c$ (where V_c is the cut off V

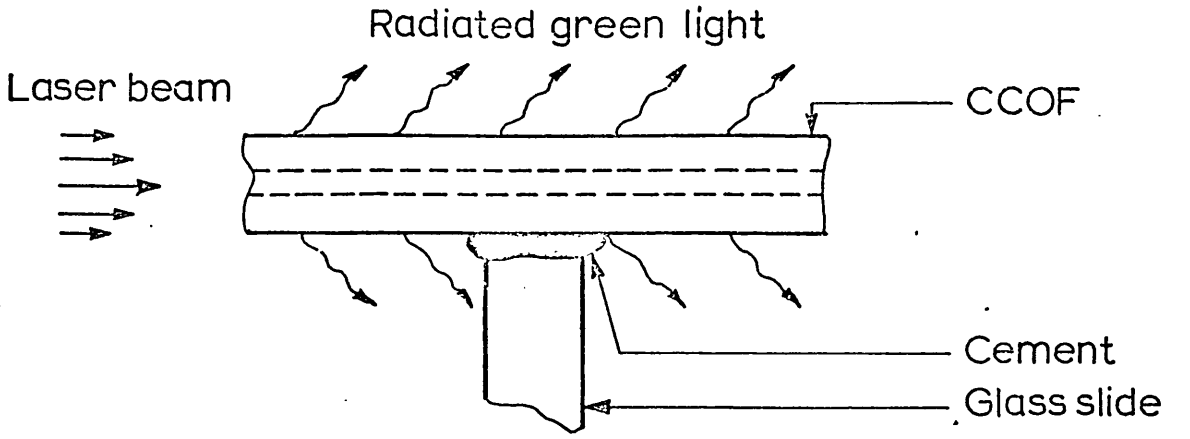

Fig. 4.7. Illustration of the observed mode of SHG in mDNB-Pyrex CCOF.

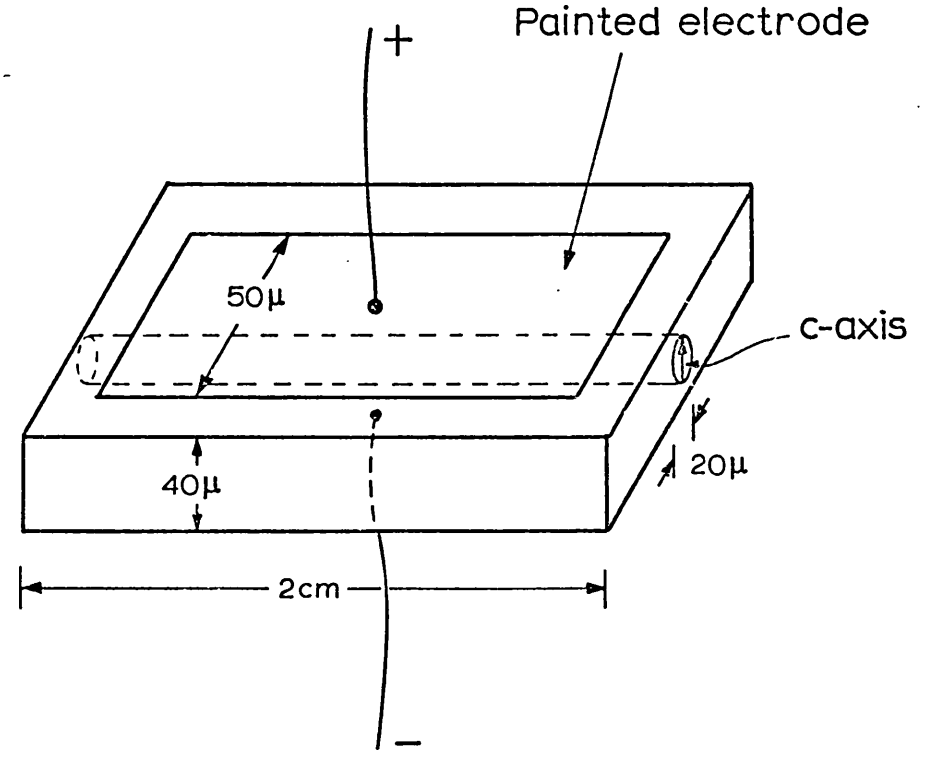

Fig. 4.8. Schematic diagram of a phase-modulator utilizing mNA-Pyrex CCOF.

value for the mode in question) $n_{ef} \simeq n_1$. Hence in a fibre of $V \gtrsim 6$, n_{ef} for the HE_{11} mode is practically eqaul to the effective core index.

By application of a voltage (v) between the electrodes, n_z would change by n_z, where (section 2.5)

$$\Delta n_z = \frac{n_z^3 r_{33} v}{2d}$$

and d is the distance between electrodes. The change in optical path, then, is $\Delta n_z . l$, where l is the length of the device. Thus a phase shift of $\pm \lambda/4$ (resulting a dynamic range of $\lambda/2$ for the modulator) would result on applying a voltage given by

$$v = \pm \frac{\lambda d}{2 n_z^3 r_{33} l}$$

Both r_{33} and n_z of mNA have been given by Stevenson (1973,II):

$$r_{33} = 16.7 \times 10^{-12}\ mv^{-1} \quad \text{and} \quad n_z = 1.675 \pm 0.01 \text{ at } 633 \text{ nm}$$

Also from Fig. 4.8: d = 40 μm and l = 2 cm. Substituting the numerical values results in v = 8.1 v.

A measured value of 4.6 for ε_{33} of mNA has been given by Ayers et al. (1972). Assuming a cladding glass with a permittivity near to this value (e.g. ε for Pyrex is 5.7), the input capacity of the device would be

$$c \simeq \frac{5.\varepsilon_o A}{d}$$

where A is the area of the electrodes used. Substituting the

numerical values results in $C = 1.1$ pF; limiting the band width of the device to ~5.0 GHz (a 50 Ω connection line is assumed).

For detection of a phase-modulated signal, however, a local oscillator is needed, to allow comparison with the received signal. In fibre-optic communication links using phase-modulation, practically demonstrated by Davies and Kingsley (1975), a reference fibre is used for this purpose.

In the above discussion only one mode was considered (single mode propagation was assumed). If for instance, two modes were present, the amount of phase shift for them would be different and at the receiver end the signal could be extracted using the interference between these modes. By increasing the number of modes, however, the efficiency would decrease due to the complexity of a multimode diffraction pattern.

The practical use of a phase-modulator in optical communication links has been demonstrated by Davies and Kingsley (1975). The modulation is achieved by dynamic mechanical stressing of the fibre using a transducer (Davies & Kingsley, 1974). This causes a refractive index change in a short length of the fibre and hence phase-modulates the propagating light. The modulator used, having an interaction length of 10 cm, needs a driving voltage of 35 V to provide a $\lambda/2$ phase shift and the band width of the device is limited to 10-20% of the modulation frequency.

A comparison between the CCOF phase-modulator described above and the latter clearly indicates its advantages for communication links such as those demonstrated experimentally by Davies and Kingsley.

The electro-optic modulators available for integrated optics (see e.g. Taylor and Yariv, 1974) are also basically phase-modulators; intensity modulation is subsequently achieved by diffraction or interference. The CCOF phase-modulator described has the clear advantage of fibre compatibility and lower attenuation.

Direct electro-optic amplitude modulation has been achieved by utilization of voltage induced waveguides in crystal slices (Soref et al., 1976). These however suffer from high attenuation owing to their mismatch with optical fibres; recent progress on this aspect has brought attenuation levels down to ~10dB (McMahon and Nelson, 1977).

For a demonstration of the multimode phase-modulation described, the following experiment was carried out at an early stage of the work using Kerr liquid filled fibres. On application of an electric field, the refractive index of a Kerr fluid varies, and a beam of light passing through the liquid undergoes a phase retardation given by (see e.g. Kruger et al., 1973).

$$\phi = 2\pi BLE^2 \qquad (4.4.1)$$

where B is the Kerr coefficient of the liquid used and L is the length of the device. Thus assuming a distance d between the electrodes, the voltage required for a π radian phase retardation is given by

$$V = \frac{d}{\sqrt{2BL}} \qquad (4.4.2)$$

Nitrobenzene ($B = 4.5 \times 10^{-12}$ mV^{-2}, $n = 1.548$) was used as the Kerr liquid. A Pyrex fibre of 30 μm i.d. and 7 cm length was filled and placed between two 5 cm long electrodes ~0.1 mm apart positioned on a three dimensional micromanipulator. A He-Ne laser beam polarized parallel to the electric field was launched into the fibre from one end and, using the necessary lenses, a magnified image of the other end was projected on a pin hole attached to a photomultiplier by a bundle of optical fibres. By defocussing the image, the multimode radiation pattern of the fibre could be produced; different multimode patterns could be obtained by altering the launching conditions. The output of the photomultiplier, after passing through a high-pass filter was monitored on an oscilloscope. The experiment was carried out at 200 KHz to avoid the impurity effects which may decrease the effective Kerr coefficient of the liquid at low frequencies (see previous reference). A photograph of the equipment used is given in the Appendix.

The voltage needed for a Π radian retardation, according to Eq. (4.4.2) was ~150 V. However due to high permittivity of the liquid (ε=35) the electric field in the core was by a factor of ~6 less than that in the cladding ($\varepsilon_{Pyrex} = 5.7$) and practically higher voltages were necessary in order to observe the effect.

A voltage of 200 Vrms was used in the following experiment (limited by the amplifier used).

Intensity variations upto ~5% were measured. The shape of the recovered signal as explained by Eq. (4.4.1) differed from the modulating wave. The former was strongly dependent both on the position of the detector (pin hole) with respect to the diffraction pattern and on the launching conditions. Larger signals were detected when the launching conditions were adjusted to obtain simpler diffraction patterns (i.e. excitation of lesser number of modes). The signal level was not stable and varied owing to the gradual change in the shape of the diffraction pattern probably arising from mechanical or thermal agitations.

After this, efforts were directed to both the growth of benzil and alteration of the growth direction of the other materials, as described in Section 3.7, in order to repeat this experiment using a CCOF. However, success was not achieved within the time available.

A device for direct amplitude modulation of light utilizing a CCOF has been proposed by Stevenson (1977). In this device the electro-optic disturbance of the core index with a spatially periodic field causes coupling between guided and unguided modes of

the waveguide, and hence modulates the output power. Reconsideration of this device, especially after demonstration of the possibility of crystal orientation control, is of considerable importance.

CHAPTER 5

FIBRE GROWTH FOR MATERIALS PREPARATION AND ASSESSMENT

The technique of crystal growth presented in Chapter 3 has many advantages as a method of evaluation of organic crystals. For example it is usually necessary to grow large, high-quality crystals which need to be cut, lapped and polished in order to produce test specimens. Furthermore the crystallization of organic materials has not yet reached the stage of development of that for inorganic materials, and a great deal of time-consuming effort is needed to find the optimum conditions for the growth of each substance. The "fibre growth" method can provide long lengths of good quality crystals within a matter of 1.5 hr, compared with days by conventional growth techniques. In each run a stock of crystals enough for many different experiments can be obtained, and since each is enclosed in glass cladding, storage of the crystals is easy and no deterioration is expected due to hydrolysis, oxidation or sublimation. The equipment needed for fibre growth is simple, and a lesser degree of control of the growth conditions is needed compared with conventional techniques. Also it was found that the process can usually be carried out in air if the material can resist oxidation for only ~3 minutes; after this period the material is enclosed in fibres and has a negligible contact with the surrounding atmosphere.

Another advantage of the technique stems from the fact that only a small amount of the material is needed for

the process. For example, only ~0.5 g of material was used in each run of the growth experiments presented in Chapter 3, but it would be possible to decrease the amount needed by an order of magnitude, by minor modifications to the apparatus. This aspect of the method is of importance when the organic material is expensive or difficult to synthesize.

Furthermore, the method proved to be applicable for materials which had been known to be intractable by conventional methods; and since the process is fast, materials with slow decomposition rates at their melting points can also be grown. In such cases the duration of the process can be decreased to well below an hour by simple modifications.

Thus in cases where the assessment can be carried out in fibre geometry, fibre growth technique is obviously to be preferred. Under normal growth conditions one of the principal dielectric axes of the crystal is parallel with the fibre axis. However it was shown in Section 3.8 that in certain conditions it is possible to obtain crystals of other orientations. This is important for property measurement as a function of orientation.

However, not many of the conventional assessment techniques are readily applicable to fibre crystals. In this and the next Chapter examples are given to show that, not only it is possible to devise methods of evaluation suitable for fibres, but in some cases this geometry presents some advantages.

5.1 X-Ray Analysis of Fibre Grown Crystals

The preparation and mounting of small sized crystals is a necessary preliminary to recording the X-ray single crystal diffraction pattern. For organic materials, the crystals are usually grown from solution, and a specimen of suitable size, depending on the absorption coefficient of the mateiral (usually of the order of 0.1 mm), is chosen and properly shaped as a sphere or cylinder. The methods used for shaping crystals in general involve technical difficulties. Crystal "spherizer" is used for grinding the crystal specimen to a nearly spherical shape (Bond, 1951), but this cannot be successfully used for soft or easily deformable materials. Cylindrical geometry is obtained by selective dissolution of the sample using a "solvent lathe" (Paterson et al., 1960). The preference of the two geometries arises because absorption errors in the intensity data obtained can easily be corrected (e.g. see, Stout and Jensen, 1968). In fact, intensity data recorded from perfectly spherical or cylindrical samples do not need correction in many cases, but it has been shown by Jeffery and Rose (1964) that a considerable error is involved even in the case of approximate spheres or cylinders obtained by grinding. When high accuracies are desired corrections are needed even in the case of the ideal geometries, especially when the absorption coefficient of the material is high, but the correction factors are readily available (Stout and Jansen, 1968).

The use of a fibre grown specimen eliminates or simplifies many of the usual stages for single crystal

photography. Fibre growth in itself requires less time than solution growth, the geometry and alignment of the crystals obtained are suitable for X-ray examination and no mounting is needed since a segment of the crystal cored fibre can be positioned on the goniometer head within the camera, so that the fibre is aligned with the axis of the camera. In practice the process proved to be so simple that it could be carried out by an untrained operator.

These are also advantages in cases where the material is too soft or deteriorates rapidly in air, since the glass cladding provides protection. Also, the use of a fibre sample allows X-ray studies to be made at temperatures near to the melting point of the material, which simplifies the study of temperature-sensitive structure changes in organic materials.

If not taken into account, scattering from the glass cladding can cause a considerable error in intensity measurements. This can be avoided to a large extent by placing an empty glass fibre in the camera and measuring the diffuse scattering. These values are subtracted from the corresponding intensity data recorded for the crystal cored fibre. Even in the conventional method, there is some diffuse scattering due to the glass fibre and adhesive used for mounting, which although small, is difficult to estimate precisely.

X-ray examinations were carried out on both mDNB and benzil filled fibres (Chapter 3). Samples of different diameters and core to cladding ratios were used without difficulty. Zero and first level Weissenberg patterns obtained from a mDNB filled fibre are shown in Fig. 5.1.

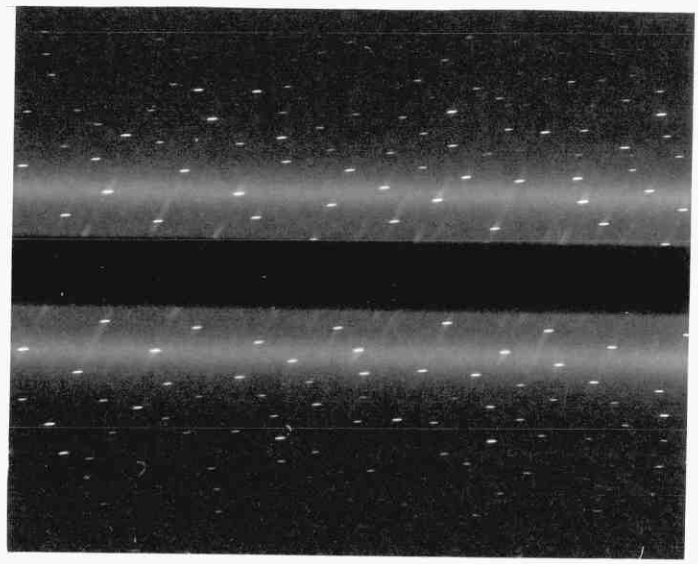

(a)

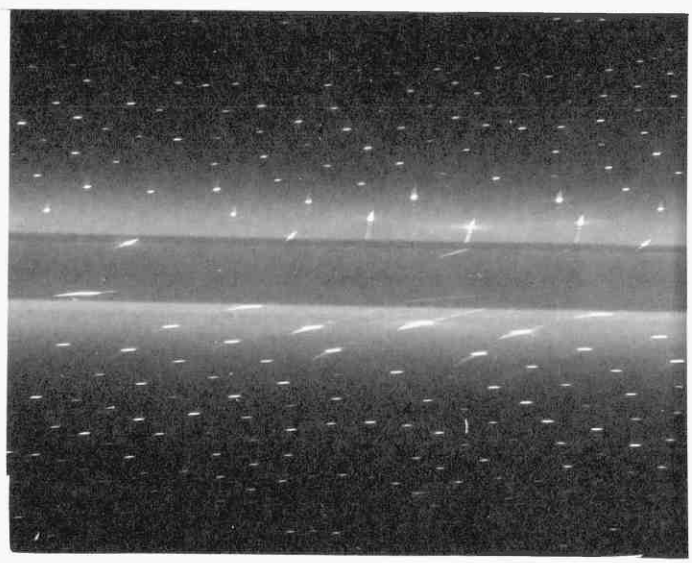

(b)

Fig. 5.1. Zero (a) and first (b) level Weissenberg photographs of a fibre grown mDNB crystal.

The diffuse parallel lines near the centre are due to the glass cladding.

5.2 Evaluation of the Optical Properties

5.2.1 Refractive indices, Electro-optic and Electro-chromic effects

The measurement of refractive indices of organic crystals, using fibre samples, is discussed in detail in the next Chapter. Also, based on the experimental results obtained, potentially accurate methods for the measurement of electro-optic and electro-chromic coefficients are proposed.

5.2.2 Absorption spectrum

Many optical materials have low absorption coefficients and for accurate determination of the absorption spectra long lengths of good quality crystals are needed. Hence long fibre-grown crystals present an advantage in this respect. The proposed experimental arrangement is shown in Fig. 5.2 where white light is launched into a length of crystal cored fibre after passing through a monochromator. The fibre is embedded in a liquid with a refractive index higher than that of cladding to eliminate light launched into the cladding. The intensity of the transmitted light is then measured as a function of wavelength.

This arrangement obviously, inherits the problems encountered with a single beam spectrophotometer, and measures must be taken to minimize the corresponding errors. If the

measurement is carried out within a wavelength range where the cladding glass attenuation is large, this also must be taken into account, otherwise the effect should be negligible since CCOFs are usually of large V values (see Section 4.1) and hence the optical power in the cladding is small.

The measurement of the absolute value of the absorption coefficient was found to be difficult with this technique (Section 4.1), since the experiment should be repeated for fibres of different lengths and it was difficult to maintain the same launching conditions in each case.

5.3 Microzone Refining

For conventional purification and crystal growth of organic materials, a quantity of ~100 g is usually required. If only small amounts of a material are available, as is often the case for materials which are difficult to synthesise, the fibre preparations can also be used for purification. Zone refining (Pfann, 1968) of organic materials within fibres proved to be simple, quick and effective. This was carried out for FNPH and BNA both of which were found to be intractible by conventional zone refining technique since their decomposition rate exceeded the rate of the process.

The apparatus used for fibre zone melting was a modified version of the miniature furnace described in Section 3.3, a schematic diagram of which is shown in Fig.5.3. A short melted zone was produced by adjusting the electric current and air flow; the zone was then progressively moved along the fibre, say from A to B in Fig. 5.3, by manually controlled pulling at a rate of ~5 mm / min.

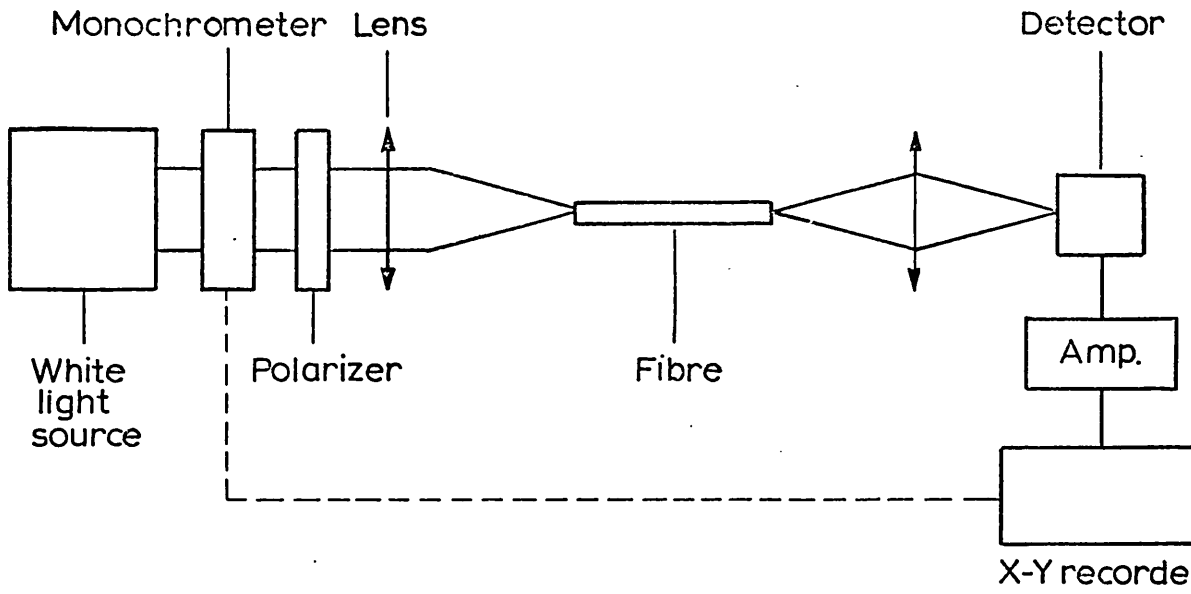

Fig. 5.2. Experimental arrangement for recording transmission spectrum, using a fibre grown crystal.

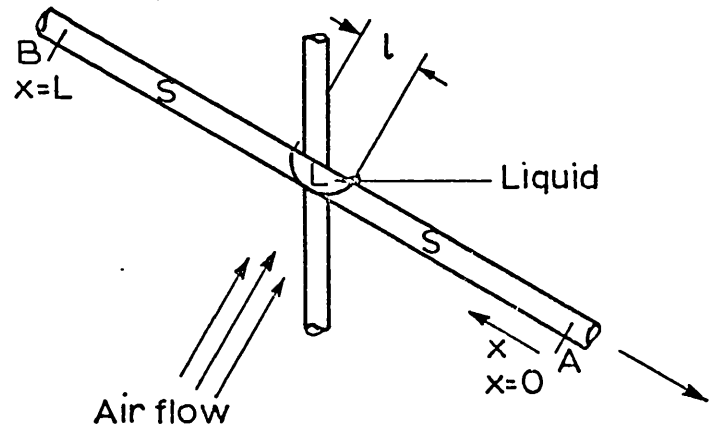

Fig. 5.3. Schematic diagram of the apparatus used for microzone refining.

After reaching B, the heater was switched off and the fibre returned to the original position and the operation repeated. The process was carried out under continuous observation as described in Section 3.3.

Considering the ultimate distribution of an impurity with equilibrium distribution constant k (the ratio of the equilibrium activity of the impurity in the solid to that in the liquid, $k = a_{s(eq)}/a_{l(eq)}$) when $k<1$ (i.e. the impurity tends to move in the direction of the zone passage), after a large number of zone passes, the ratio of the impurity concentration at $x = 0$, C_u, (Fig. 5.5) to the impurity concentration before zone refining, C_o may be written as

$$\frac{C_u}{C_o} = k^s \qquad (5.1)$$

It has been found empirically that (Pfann, 1968)

$$s = \frac{fL}{\ell} \qquad (5.2)$$

where L and ℓ are the total length of the change and the zone length respectively, and f is a constant of value ~1. Thus it follows that the degree of purification achieved by zone refining is a strong function of L/ℓ.

In conventional zone refining apparatus for organic materials, the length of the zone obtained is about 5 mm and that of the charge about 20 cm i.e. $L/\ell = 40$. In the case of the microzone refiner described here ℓ is of the order of the internal diameter of the fibre, say 40 μm,

and L in our experiments was about 2 cm, limited only by the apparatus used; this gives L/ℓ = 500. Hence the purity obtained is much higher than for the conventional case. Furthermore, in conventional zone refining the material is usually polycrystalline and purification can be hindered by the concentration of the impurities in grain boundaries. In microzone refining, however, the material grows as single crystal and hence the problem is eliminated.

In practice, high pulling rates could be employed (~ 5 mm min^{-1}) for microzone refining and consequently the process completed within about an hour, compared to weeks for conventional zone refining, which allows materials such as FNPH and BNA to be zone refined without excessive decomposition.

Fibres of suitable length can be filled with only ~10mg of the material, since 10cm of a filled 40 μm fibre contains not more than 0.2 mg (the densities of most organic solids fall within the range of 0.9-1.7 g cm^{-3}). For small amounts of material, the filling process was carried out by melting the material on a glass slide to form a droplet; the ends of the empty fibres, lying on the slide, were carefully dipped into the droplet and filling occurred by capillary attraction. Purification was carried out by the above technique. Then, one end of the fibre was cut and the zone refined material within the fibre was remelted and recrystalized carefully, using the miniature furnace. Recrystalization is desirable because the void density in a crystal obtained from the zone refining process was high, since in this case, unlike the growth methods presented in Chapter 3, the volume contraction on freezing cannot be

compensated for by liquid flow. The product was a crystal cored fibre suitable for X-ray studies and property evaluation, as presented in this and the next Chapter.

CHAPTER 6

A NEW METHOD FOR THE MEASUREMENT OF REFRACTIVE INDICES IN ORGANIC SOLIDS.

Accurate measurement of refractive indices and dispersion of crystalline substances is afforded using various methods based on the light deflection by prisms made from the material in question (see e.g. Zernike, 1964). These methods, however require growth of large, quality crystals, shaping them into prisms and preparation of optical quality faces. These stages of work are usually more difficult in organic crystals, since apart from crystal growth problems, they are generally soft and hence difficult for shaping.

In an alternative technique, immersion method, small fragments of crystal are immersed in series of liquids of known refractive index for minimization of the difference in refractive index between the crystal and the liquid, which is infered from the relief of the crystal within the liquid. Accuracies of upto $\pm$ 0.002 are obtainable (Bloss, 1961), but this depends, to a great extent, on the visual judgement and experience of the experimenter. Furthermore organic materials present difficulties due to their solubility in the immersion liquids used.

Thus a method whereby the measurement of the above-mentioned properties in organic crystals are facilitated is of importance.

A dielectric object irradiated by plane light waves, scatters the light in various directions; the scattered light, obviously contains information about the geometry and

refractive index of the object. It has been shown (van de Hulst, 1957) that, given the necessary data about the object, in general it is possible to predict the scattering behaviour, using numerical methods. However, to proceed in the opposite direction, i.e. to extract information on the properties and physical dimensions of the object from the characteristics of the scattered light, is by no means easy. An example of particular interest is scattering from glass fibres when irradiated by a laser beam directed perpendicular to its axis (Fig. 6.1). The scattered light flux as a function of angle in the plane perpendicular to the fibre axis (to be called "scattering pattern" hereafter) has been shown to afford valuable information about the fibre (Presby, 1973).

The exact theory of the scattering from a dielectric cylinder (unclad fibre, Fig. 6.2a) has been given by van de Hulst (1957) which showes that an analytical description of the scattering pattern is not possible. Also, an exact solution for the problem of scattering from concentric dielectric cylinders (clad fibre, Fig. 6.2b) has been given by Kerker and Matijevic (1961); finally Marcuse and Presby (1975) studied the theory of scattering from fibres with arbitrary refractive index distributions. All of the theoretically generated patterns are in excellent agreement with the experimental observations. However the complexity of the exact solutions does not allow extraction of the fibre properties from the experimentally obtained patterns. Of course, it is possible to generate many patterns and search for the best fit to the experimentally recorded one, but considering the complexity of the necessary calculations the method is costly.

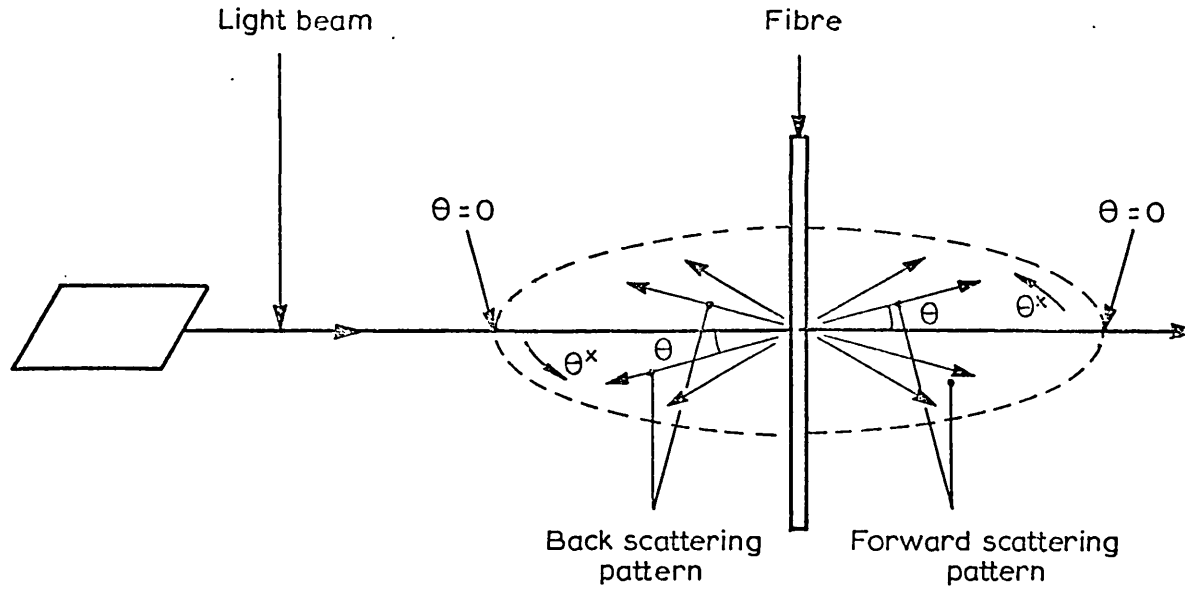

Fig. 6.1. Illustration of scattering from a laterally illuminated fibre.

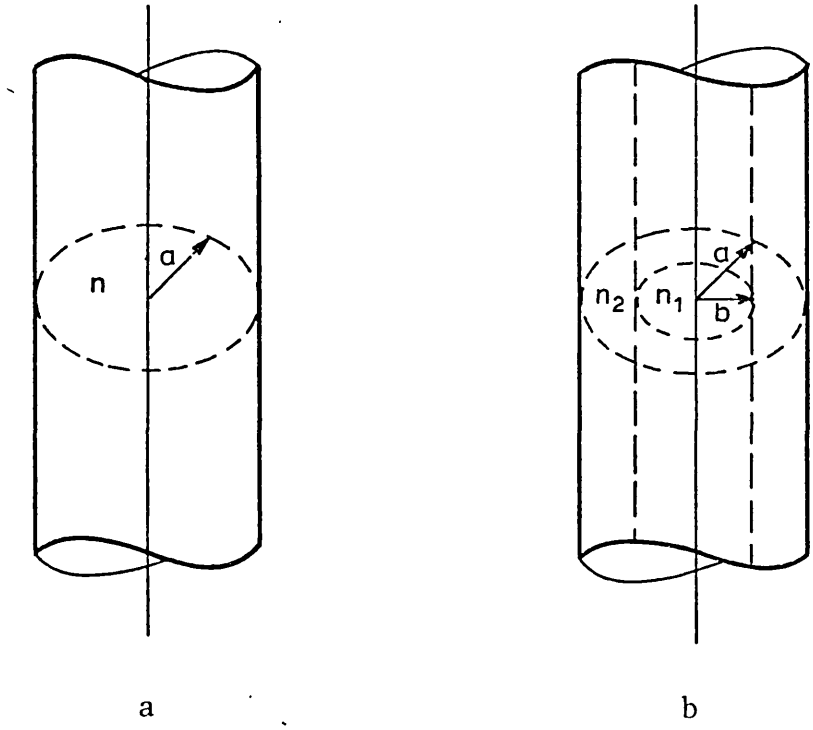

Fig. 6.2. Schematic of, (a) unclad fibre, (b) clad fibre.

Geometric optics serves better in this respect. It provides approximate analytical solutions for some regions of the scattering pattern, which makes it possible to attribute a specific feature of the pattern (e.g. peaks or cut-off locations) to a particular parameter of the fibre, and by examining that specific feature in the experimentally obtained pattern, to identify the fibre parameter responsible.

The experimental method for the production of these scattering patterns is simple in principle; a schematic diagram of the basic experimental arrangement is shown in Fig. 6.1. A beam of light strikes the fibre, and the scattered light is observable around the fibre over 360^{o}. In Fig. 6.1 the scattering pattern is divided into two sections: back-scattering and forward-scattering. The origin ($\theta = 0$) from which the angular positions are measured is chosen differently for these two sections in order to simplify the calculations. The $\theta = 0$ positions for both sections of the pattern are also shown in Fig. 6.1.

In this Chapter the main features of the scattering patterns obtained from different kinds of dielectric fibres, using ray theory, are studied. Then it is shown that the refractive indices of concentric dielectric cylinders can be obtained from recorded scattering patterns. This in turn has been shown to afford a method for the measurement of refractive indices of organic solids.

6.1 Back-Scattering

6.1.1 Unclad fibre.

A cross-section of an unclad fibre with refractive index n and radius a is shown in Fig. 6.3, where a collimated mono-chromatic beam of light polarized parallel to the fibre axis (to be called parallel polarization hereafter), is assumed to be incident upon it. The intensity of the beam is considered to be constant throughout the diameter of the fibre. In the geometrical-optics approximation when a ray hits the fibre it undergoes reflection and refraction, which alter the direction of the ray in accordance with the law of reflection and Snell's law. Here the aim is to consider only the rays which finally emerge from the fibre backwards (see Fig. 6.1) neglecting the ones which undergo more than one internal reflection, due to their low irradiance. Two types of rays fulfil these requirements both of which are traced in Fig. 6.3 and are designated as "ray I" and "reflected ray" respectively.

Ray I, as shown in Fig. 6.3, is incident upon the fibre with an angle i, undergoes a refraction and enters the fibre and after one internal reflection and another refraction emerges from the fibre making an angle Φ_I with its original direction. It follows directly from geometrical considerations of Fig. 6.3 that:

$$\Phi_I = 4 \text{ Arc sin } (\frac{\sin i}{n}) - 2i \qquad (6.1.1)$$

The angle of incidence is related to the distance of the ray from the centre of the beam (from the ray passing through the centre of the cross-section), d, by:

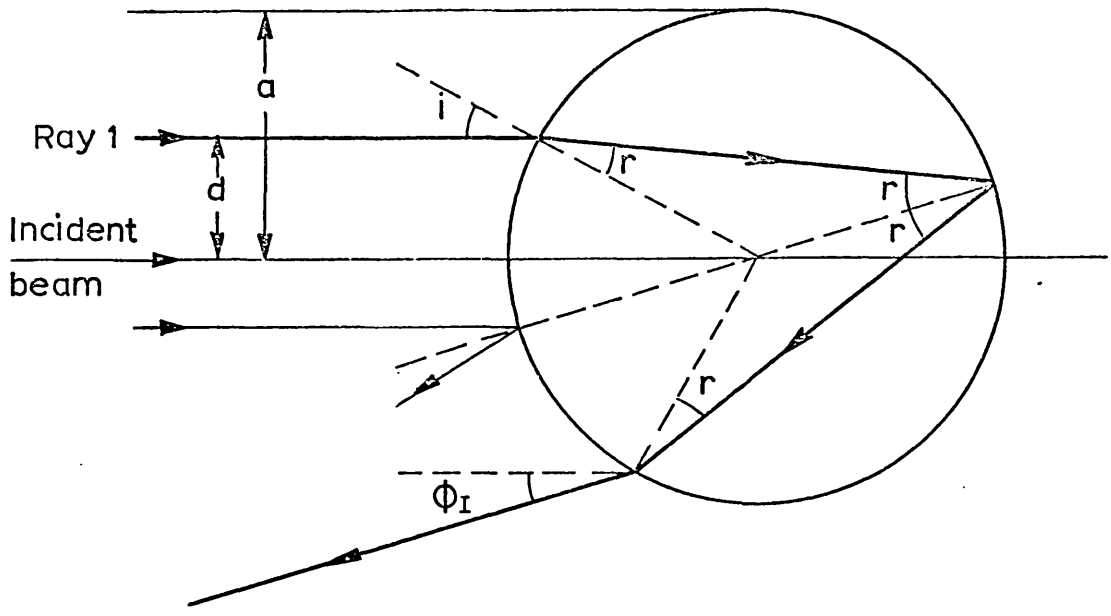

Fig. 6.3. Cross-section of an unclad fibre, showing paths of the major back scattered rays.

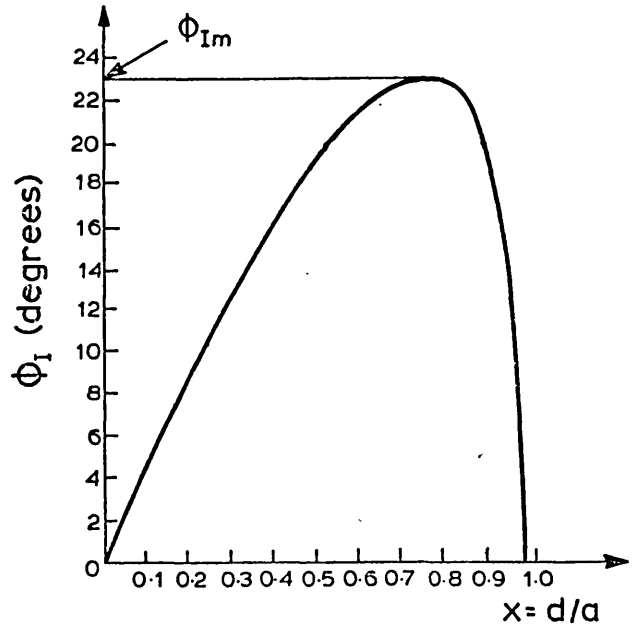

Fig. 6.4. Plot of Φ_I vs. d/a for an unclad fibre of n=1.50 (after Presby, 1973).

$$i = \text{Arc sin } \frac{d}{a} \qquad (6.1.2)$$

then

$$\Phi_I = 4 \text{ Arc sin } \frac{d}{na} - 2 \text{ Arc sin } \frac{d}{a} \qquad (6.1.3)$$

Φ_I is plotted against d/a in Fig. 6.4 for a fibre of n = 1.5, which shows that the deviation suffered by the ray, Φ_I, first increases with d, i.e. with moving the point of incidence clockwise in the upper half, and then decreases after passing through a maximum. The situation can better be understood from Fig. 6.5 in which many rays have been traced. The maximum deviation angle Φ_{Im} can be obtained by setting

$$\frac{d\Phi_I}{d(d/a)} = 0 \quad (\text{or } \frac{d\Phi_I}{di} = 0),$$

resulting in:

$$\Phi_{Im} = 4 \text{ Arc sin}\left[\frac{2}{n\sqrt{3}}(1-\frac{n^2}{4})^{\frac{1}{2}}\right] - 2 \text{ Arc sin}\left[\frac{2}{\sqrt{3}}(1-\frac{n^2}{4})^{\frac{1}{2}}\right]. \qquad (6.1.4)$$

The important point is that Φ_{Im} depends only on the refractive index of the fibre.

Beyond Φ_{Im}, ray I ceases to exist, so a cut off in the irradiance of the scattering pattern at Φ_{Im} is expected. Furthermore, the irradiance of the pattern is proportional to $1/\frac{d\Phi_I}{d(d/a)}$ (Marcuse, 1975) which is a measure of the concentration of I rays at a point in the pattern corresponding to a deviation angle Φ_I. Then, it follows from examination of Fig. 6.4 that the maximum irradiance in the pattern is expected to occur at Φ_{Im}. This could also be understood from the congestion of the emerging I rays

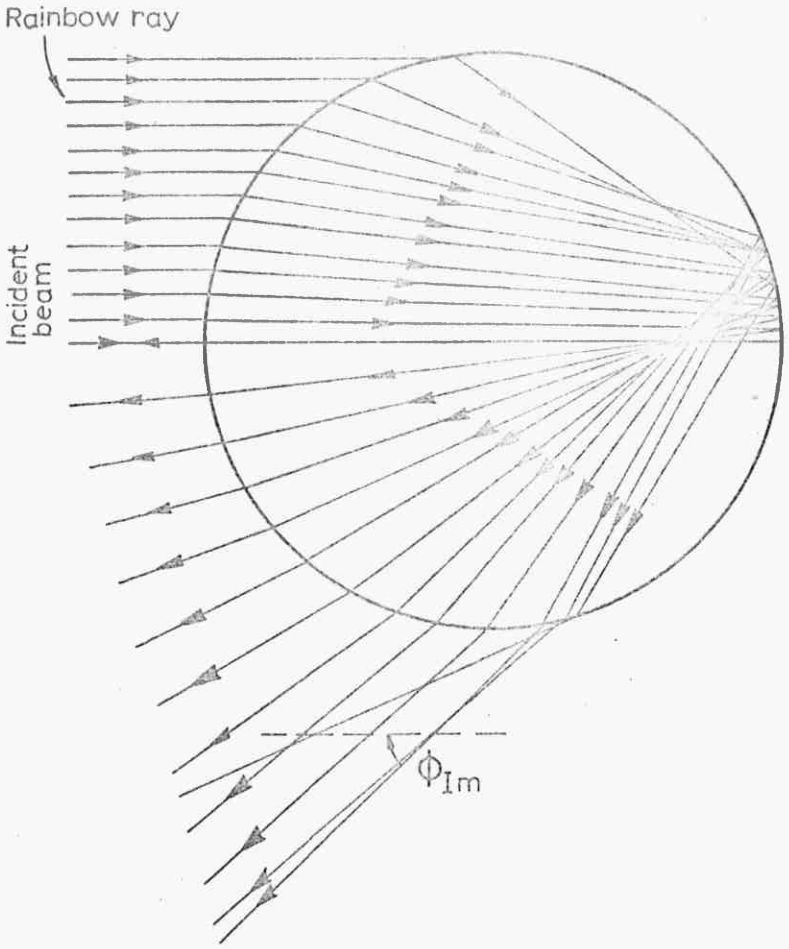

Fig. 6.5. Cross-section of an unclad fibre, showing variation of the ray path and scattering angle with the point of incidence.

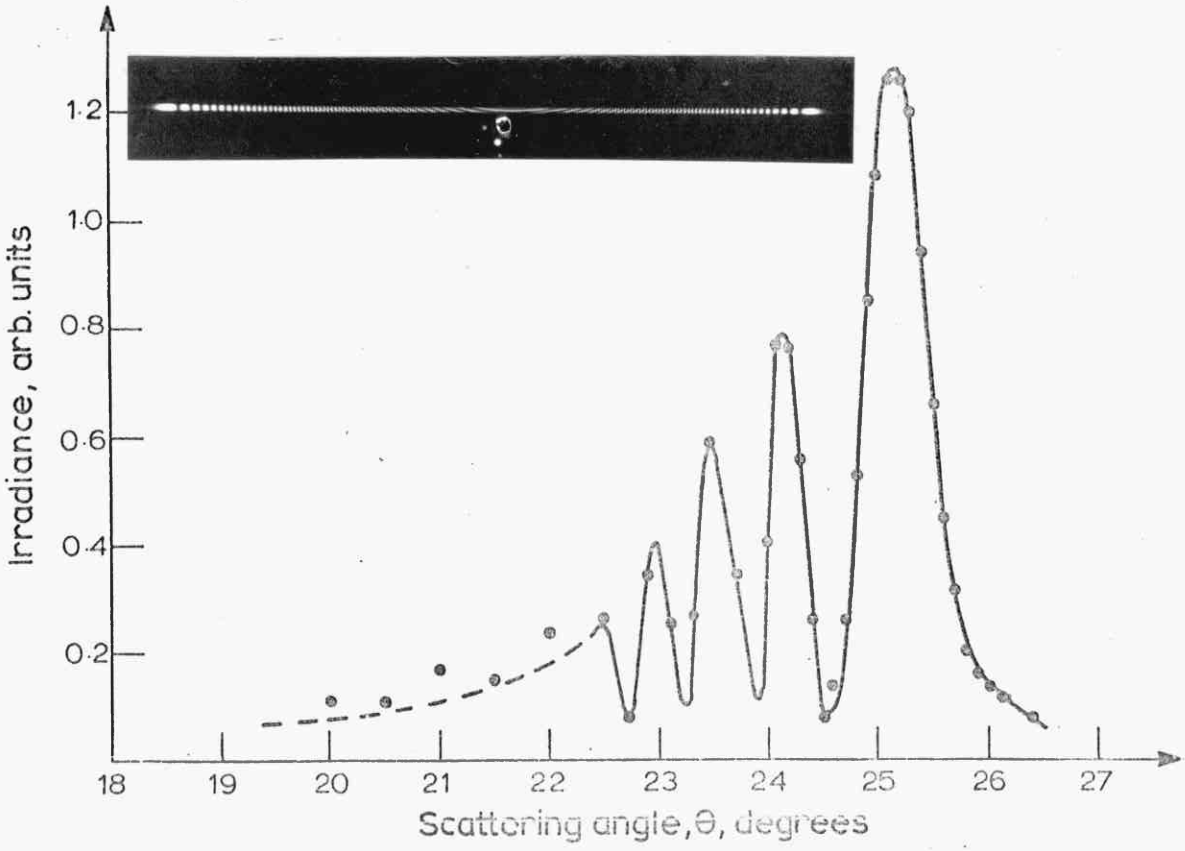

Fig. 6.6. Photograph and the irradiance vs. angle plot of back scattering from an unclad fibre (n = 1.471).

at about Φ_{Im} in Fig. 6.5. So, in summary, in the back scattering pattern a point of maximum irradiance immediately followed by a cut off is expected which corresponds to Φ_{Im} and this obviously facilitates the recognition and measurement of Φ_{Im} in the pattern. A photograph and the corresponding intensity vs. angle plot of the back scattering pattern obtained from a glass fibre in our experiments (the experimental procedure is discussed in section 6.7) is shown in Fig. 6.6 which obviously exhibits the predicted features.

Presby has measured the refractive index (Presby, 1973) and dispersion (Presby, 1974) of unclad glass fibres with respective accuracies of $\pm$ 2 x 10^{-3} and $\pm$ 2 x 10^{-4}, by measurement of Φ_{Im}. The above calculations, although recently remade for fibres, are by no means new concepts. Descart and Newton in the seventeenth century carried out similar calculations in order to show that the angle at which a rainbow is observed (rainbow angle) is independent from the size of the rain droplets. The Φ_{Im} obtained here, corresponds to their rainbow angle.

The light intensity in the pattern was related directly to $1/\frac{d\Phi_I}{d(d/a)}$, but since $\frac{d\Phi_I}{d(d/a)} = 0$ at Φ_{Im}, this predicts an infinite intensity at Φ_{Im}. As it was later pointed out by Chu (1976) and Holoubeck (1976), the intensity distribution about the rainbow angle (Φ_{Im}) is more precisely described by an Airy function which shows that Φ_{Im} must be read off from an angular position corresponding to the decrease in intensity from the maximum, I_m, to 0.4408 I_m in the obtained pattern.

Upto here the "reflected rays" were neglected. Fig. 6.3 shows that these rays contain no significant information about the refractive index of the fibre; simply because they do not enter the fibre. However in a range of pattern corresponding to $0 < \Phi < \Phi_{Im}$ they interfere with the I rays and cause the spatial oscillation of the intensity in this range, which is apparent in Fig. 6.6. The optical path difference between these two types of rays can easily be related to the diamter of the fibre (Fig.6.3), and so the angular distance between the two subsequent peaks in the pattern gives a measurement of the diamter of the fibre (Presby, 1973). This analysis was completed by Holoubek (1976), showing that accuracies of about 5% can be expected in the corresponding measurements. Diameter measurement is not of concern here and will not be discussed further.

6.1.2 Clad fibre (step index variation)

A cross-section of a step index optical fibre is shown in Fig. 6.7a, where the refractive index and the radius of the core and cladding are n_1 and b, and n_2 and a respectively. Let a parallel-polarized ray of light be incident upon the fibre perpendicular to the fibre axis at an incidence angle α_i. It undergoes refraction and enters the cladding by an angle α_1; then strikes the core at α_2 where it is refracted and enters the core by α_3. As it follows from the geometry of Fig. 6.7a, the ray emerges from the core into cladding by α_2; it is then reflected by the cladding-air interface and after crossing the core and the cladding finally emerges from the fibre with a deviation angle Φ_{II}. Such a ray will be

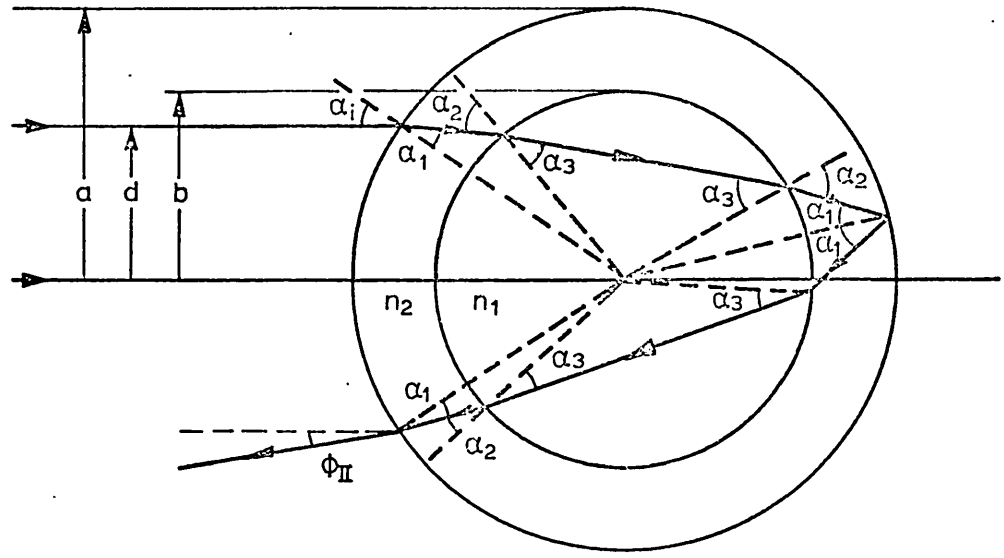

(a)

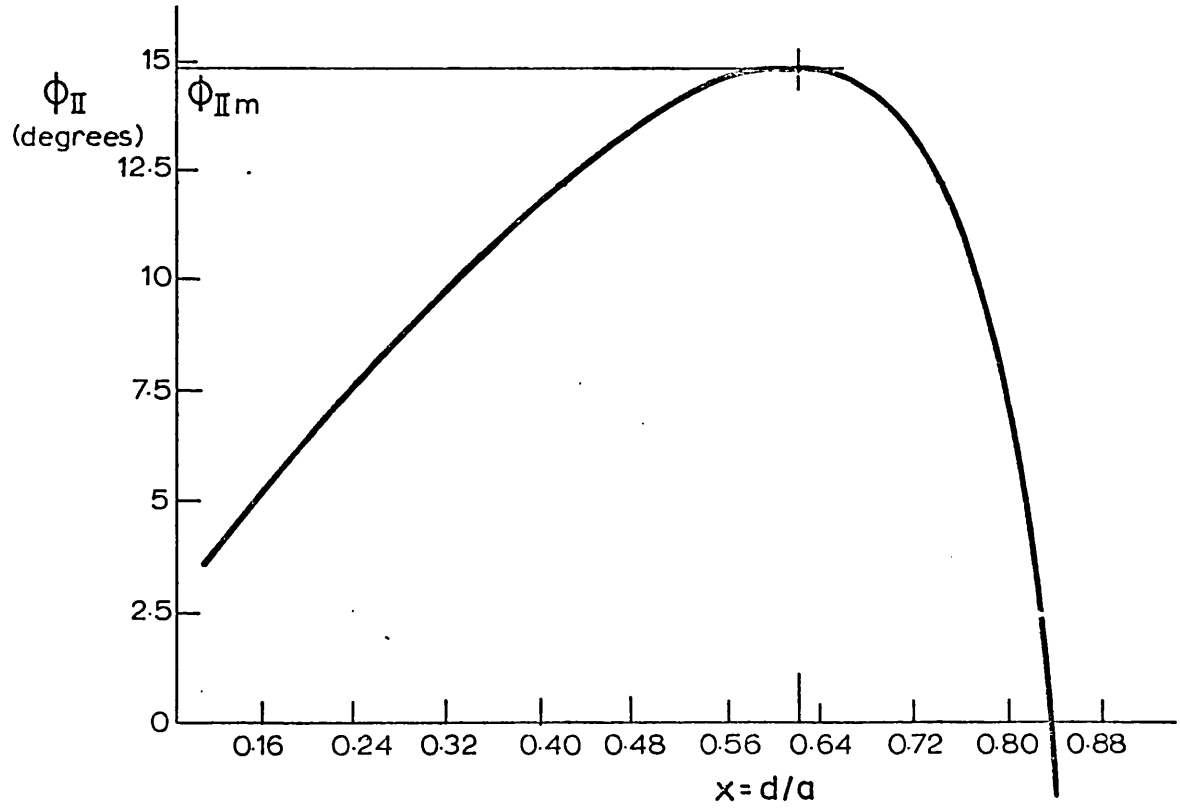

(b)

Fig. 6.7. (a) cross-section of a clad fibre showing the path for a back scattered ray. (b) plot of Φ_{II} vs. d/a for a fibre of n_1=1.520, n_2=1.457 and R=0.600.

referred to as ray II hereafter. The deviation angle follows from the geometry of Fig. 6.7a:

$$\Phi_{II} = 4(\alpha_3 - \alpha_2 + \alpha_1) - 2\alpha_i \qquad (6.1.5)$$

with

$$\alpha_i = \text{Arc sin } (\frac{d}{a}) \quad , \quad \alpha_1 = \text{Arc sin}(\frac{d}{n_2 a})$$

$$\alpha_2 = \text{Arc sin } (\frac{d}{n_2 b}) \text{and } \alpha_3 = \text{Arc sin } (\frac{d}{n_1 b}) \ ,$$

where d is the distance of the incident ray from the centre of the fibre. Taking

$$\frac{b}{a} = R \quad \text{and} \quad \frac{d}{a} = x$$

results in

$$\alpha_i = \text{Arc sin } x \quad , \quad \alpha_1 = \text{Arc sin } (\frac{x}{n_2})$$

$$\alpha_2 = \text{Arc sin } (\frac{x}{n_2 R}) \text{ and } \alpha_3 = \text{Arc sin } (\frac{x}{n_1 R}) \ . \qquad (6.1.6)$$

A plot of Φ_{II} vs. x for given values of n_1, n_2 and R is shown in Fig. 6.7b indicating that Φ_{II}, as Φ_I, passes through a maximum. Unfortunately in this case Φ_{IIm} (maximum value of Φ_{II}) cannot be related to the fibre parameters through an analytical function, but as shown later in this Chapter, computer determined plots can give its dependence on n_1, n_2 and R.

Similarly to the case of ray I, the intensity in the pattern due to ray II can be related to $1/\frac{d\Phi_{II}}{dx}$. By a similar argument and with regard to Fig. 6.7b, it follows that a point in the scattering pattern corresponding to Φ_{IIm} is of the highest intensity followed by a cut-off. This facilitates the identification and measurement of Φ_{IIm} from

the experimentally recorded patterns, which would afford calculation of one of the fibre parameters (n_1, n_2 and R) knowing the other two. The example of particular interest here is the measurement of n_1 when n_2 and R are known. Measurements of Φ_{IIm} for various fibres and preforms were carried out by Presby and Marcuse (1974); they obtained values which were in good agreement with those calculated.

In Fig. 6.7a only the rays which traverse the core were considered. Of course, there are rays which travel through the cladding only, similar to I rays discussed in the previous section. Thus the back scattering pattern for a clad fibre contains some or all (depending on the geometry of the fibre) of the features related to I rays as if the fibre was unclad with refractive index n_2, and also shows features due to rays II in addition. Photographs of three back-scattering patterns obtained from clad fibres together with an intensity vs. angle plot are shown in Fig. 6.8, all exhibiting the maxima corresponding to Φ_{Im} and Φ_{IIm}. The core refractive index has been increased from Fig. 6.8b to d keeping the other parameters (n_2 and R) constant, in order to demonstrate the dependence of Φ_{IIm} on n_1.

6.2 Forward Scattering (clad fibre)

The approximate range of the scattering pattern to be studied in this section is shown in Fig. 6.1. A cross-section of the fibre is shown in Fig. 6.9, in which the three significant rays taking part in the construction of the pattern at a scattering angle Θ are traced. Ray I is

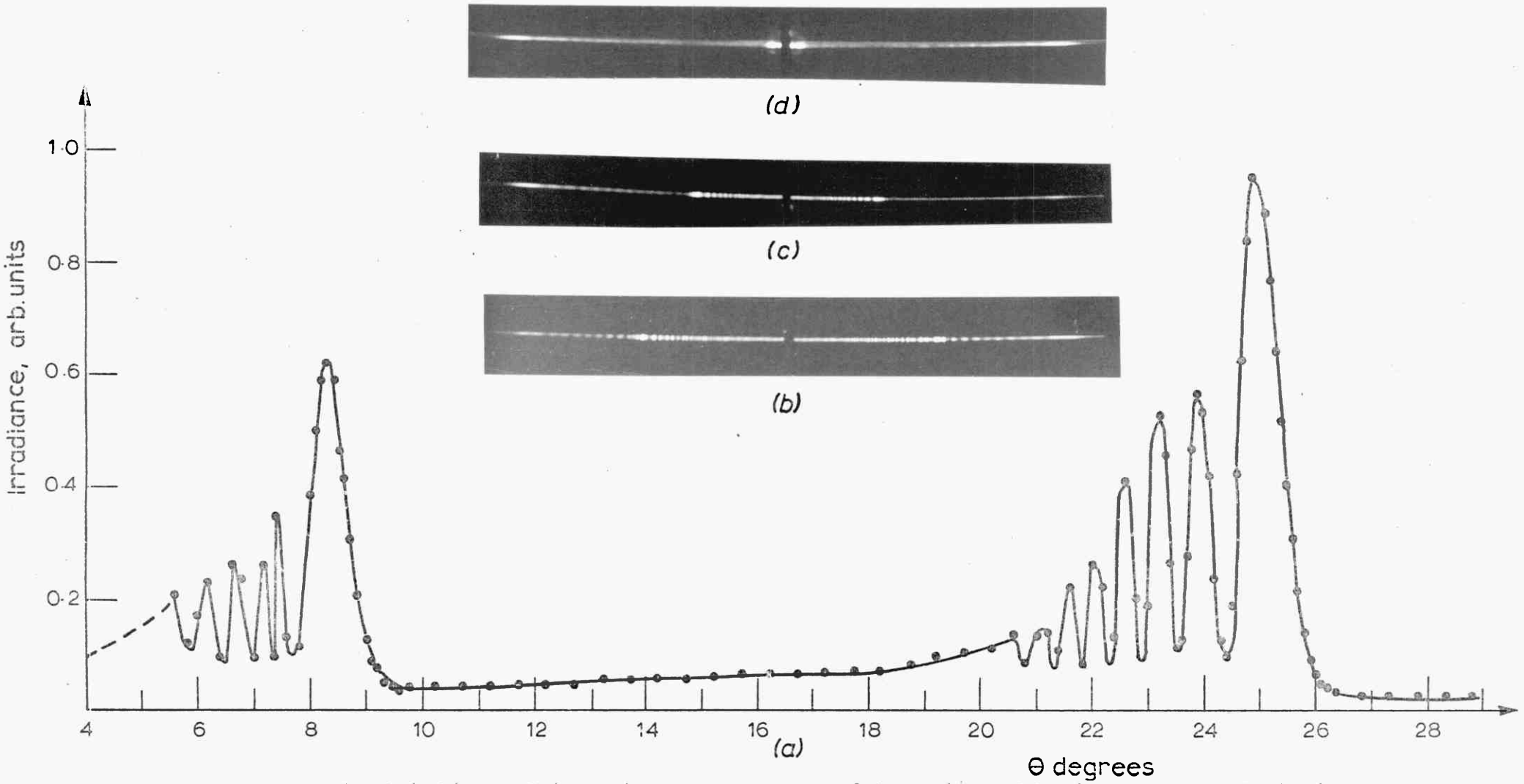

Fig. 6.8. (a) Observed variation of irradiance vs. angle for back scattering from a clad fibre (n_1=1.554, n_2=1.471 and R=0.535). (b-d) Photographs of the back scattering pattern, core refractive index has increased from b to d.

directly reflected from the cladding-air interface, ray 2 is refracted through the cladding, and ray 3 is refracted through both the cladding and the core.

It follows from the geometry of Fig.6.9 that the deviation angles, θ, of ray 2 and 3 constantly increase with d/a, and that of ray 1 constantly decreases with d/a. This indicates that a significant point for measurement, similar to Φ_{Im} or Φ_{IIm} in back scattering pattern, can not be expected to appear in the forward scattering pattern. However, it can be deduced from Fig. 6.10 that there are regions in the pattern where either ray 2 or ray 3 cannot occur. There is no ray 2 in the range of $\theta_c > \theta > 0$ and no ray 3 in the range of $\theta > \theta_u$, where the angles θ_c and θ_u follow from Fig. 6.10:

$$\theta_c = 2\left[\text{Arc sin}\left(\frac{bn_2}{a}\right) - \text{Arc sin}\left(\frac{b}{a}\right)\right] \qquad (6.2.1)$$

and

$$\theta_u = 2\left[\frac{\pi}{2} + \text{Arc sin}\left(\frac{bn_2}{a}\right) - \text{Arc sin}\left(\frac{b}{a}\right) - \text{Arc sin}\left(\frac{n_2}{n_1}\right)\right] \qquad (6.2.2)$$

Thus ray 2 and 3 co-exist within the range of $\theta_c < \theta < \theta_u$, and therefore some distinguishable features would be expected to occur in this range due to their interference. This could make the measurement of θ_c and θ_u possible from the pattern, which would afford fibre parameter measurements using Eqs. (6.2.1 and 2). An experimentally recorded forward scattering pattern (after Watkins, 1974) is shown in Fig. 6.11a, where also the calculated values for θ_c and θ_u are indicated. Fig. 6.11b shows the interference fringes predicted by geometrical optics accounting for the interference between refracted

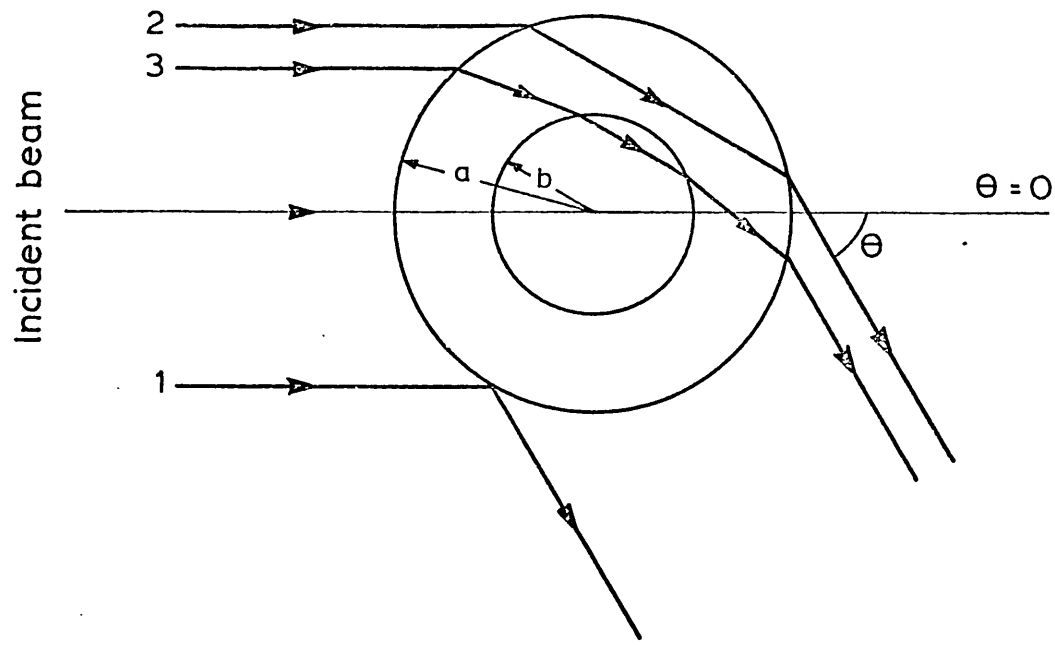

Fig. 6.9. Cross-section of fibre, showing paths of refracted and reflected rays.

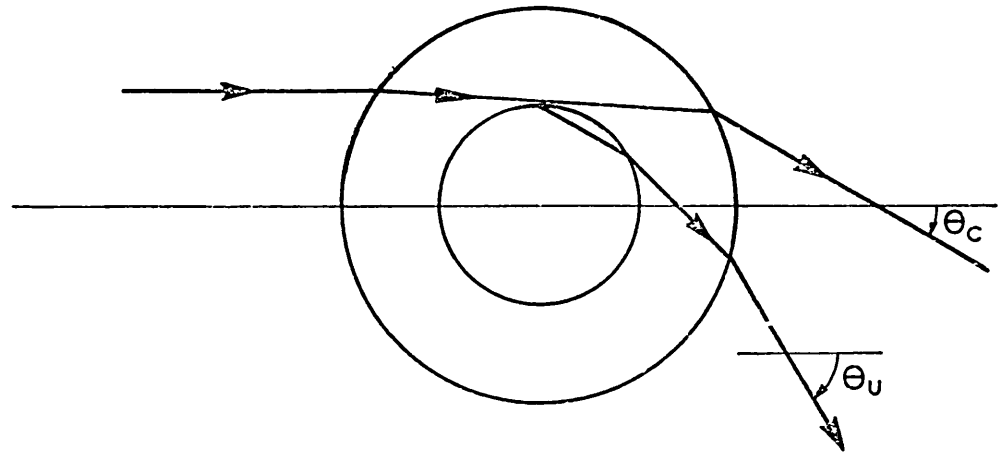

Fig. 6.10. Cross-section of fibre, showing paths of rays corresponding to scattering angles Θ_c and Θ_u.

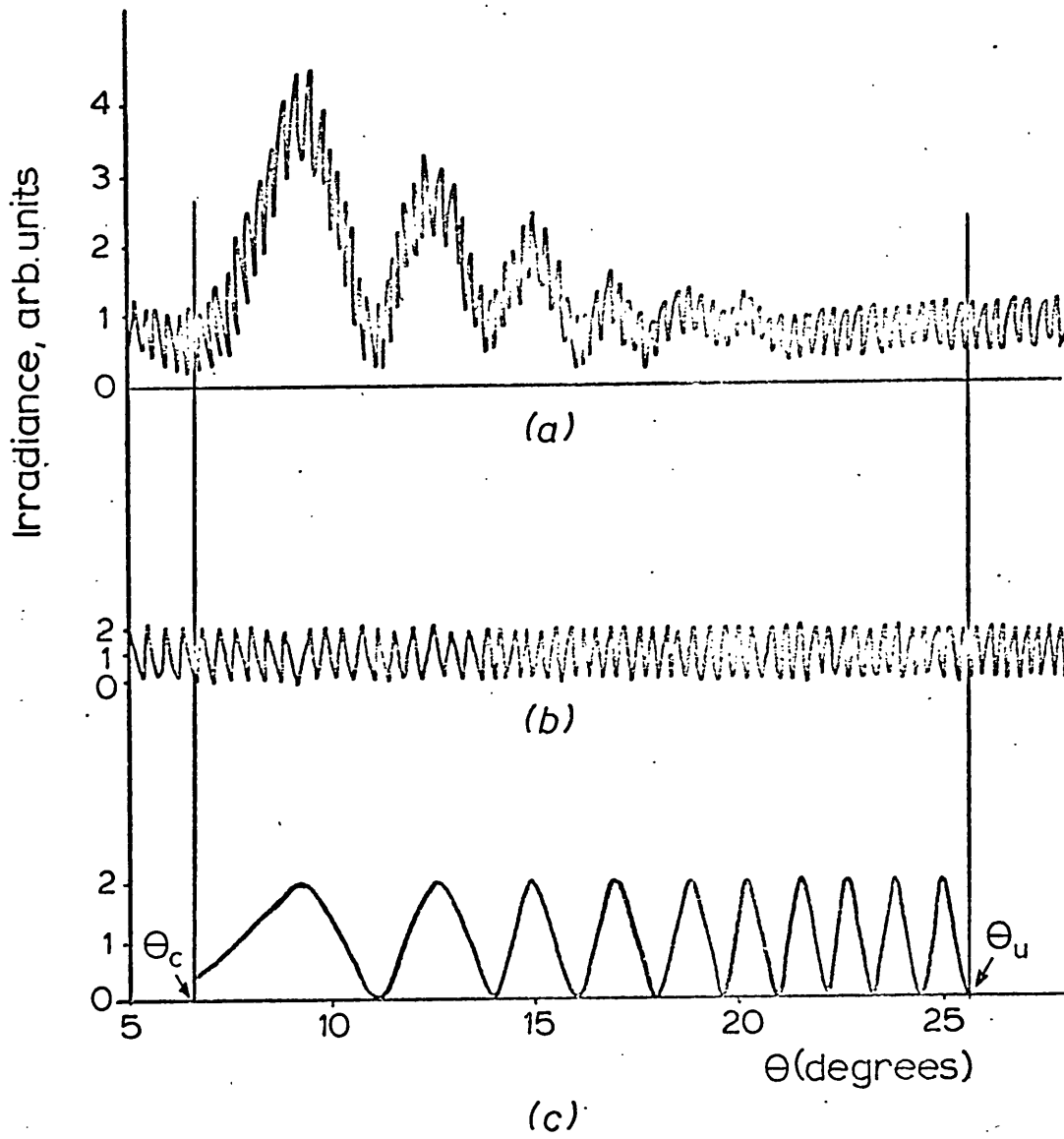

Fig. 6.11. Graphs showing (a) recorded irradiance vs. angle, (b) fringes due to interference between refracted and reflected rays, (c) modulation found due to interference between two different refracted rays (forward scattering).

and reflected rays, and Fig. 6.11c is the intensity modulation found by considering the interference between the two refracted rays. Apart from the region corresponding to $0<\theta<5^{o}$ the agreement is good, but Fig. 6.11a clearly indicates that an accurate measurement of θ_c and θ_u from the pattern is not possible.

Watkins (1974) used the approximate values measured as starting data to obtain the theoretical fit to the pattern by trial and error, and finally obtained the core refractive index with an accuracy of ± 0.003.

6.3 Measurement of Core Refractive Index: Isotropic Core.

The evaluation of the parameters of an optical fibre from the scattering pattern was discussed in the previous sections. In our specific case the fibres to be studied are not necessarily made for light guidance; so unlike optical fibres the core-cladding refractive index difference can be high (in optical fibres usually $n_1-n_2 \lesssim 0.03$). In addition, since these fibres are made only in order to measure the refractive index of the material in the core, there is more freedom in choosing of the geometry of the fibre and the cladding material. In this section it is assumed that the material to be studied (core of the fibre) is isotropic.

The choice of one from the methods described (sections 6.1.2 and 6.2) seemed obvious, since the forward scattering method was eliminated due to the complexities involved in the related trial and error calculations. In addition, the measurement of Φ_{IIm} from the back scattering pattern seemed to offer a quick and easy method for the measurement of n_1.

Plots of Φ_{II} vs. x = d/a for different values of n_1 are given in Figs. 6.12 and 6.13. Silica cladding (n_2=1.457) is assumed in both cases, and the ratios of inner to outer radii, R, are 0.4 and 0.6 in Fig. 6.12 and 6.13 respectively. The curves were ploted by computer using Eqs. (6.1.5) and (6.1.6). It is apparent from the curves that Φ_{II} passes through a maximum (Φ_{IIm}) only if $n_1 > n_2$, indicating that the cladding refractive index is the lower limit for the measurable core refractive indices using this method. As n_1 increases the curves tend to flatten around the maximum, which indicates a higher intensity at about Φ_{IIm} and hence an easier measurement. Plots of Φ_{IIm} vs. n_1 are shown in Fig. 6.14; these were obtained by calculation of the maximum value of Eq. (6.15) for each set of fibre parameters by computer. In practice, measurements in the range of $-3^o < \theta < 3^o$ proved to be difficult because the detector used blocked the incident beam. Therefore Fig. 6.14 shows that core indices higher than a certain limit (about 1.57 and 1.65 for fibres of R = 0.4 and 0.6 respectively) cannot be measured with this method. Moreover, the slope of the curves decreases with increasing n_1, i.e. the sensitivity of the Φ_{IIm} to n_1 and with it the accuracy of the measurements diminishes.

The refractive indices of organic crystals are usually in the range 1.45-1.90. Thus the lower limit (equal to n_2) is acceptable when silica or pyrex is used as cladding which impose lower limits of 1.457 and about 1.47 respectively, but the upper limits quoted above are by no means satisfactory. Considering Fig.6.14, it may appear that this range can be extended by using fibres of higher R, but for the following reasons this idea proved to be impractical: The making of

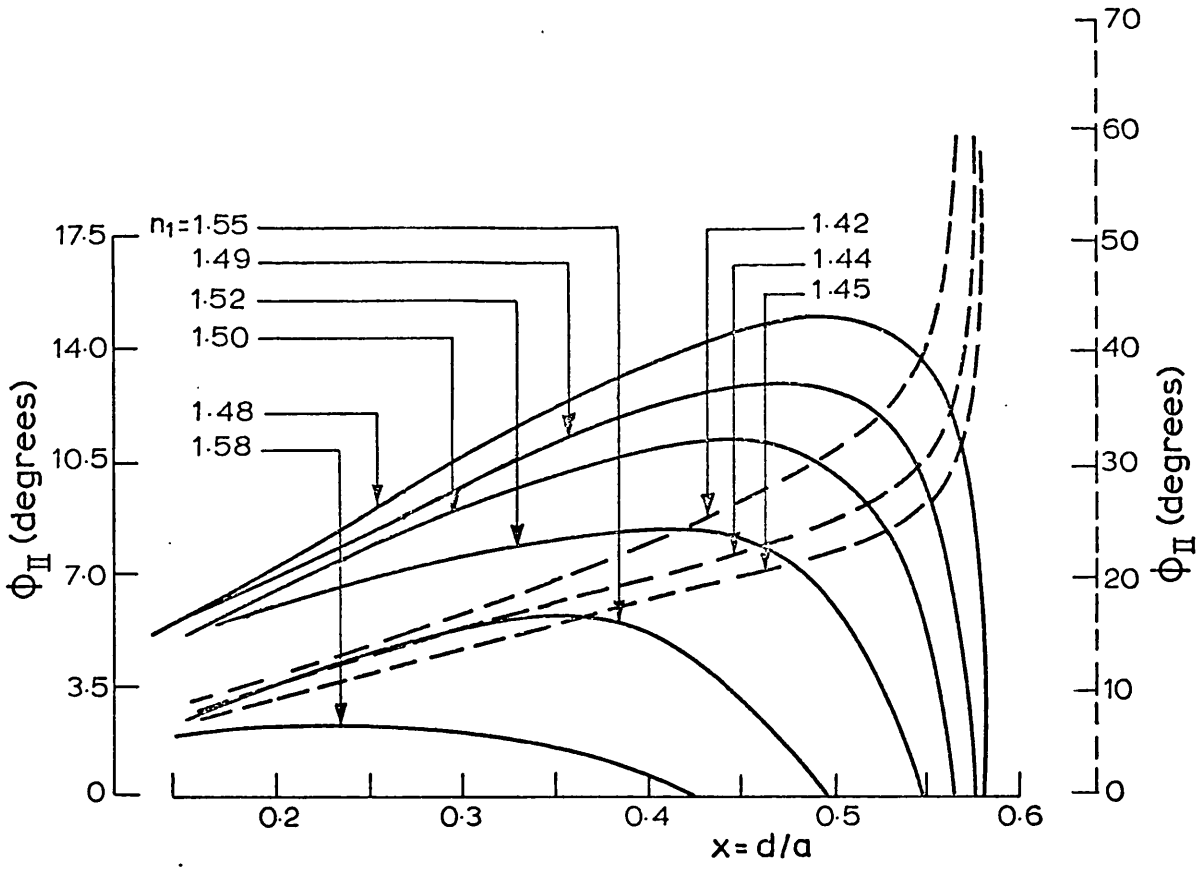

Fig. 6.12. Plots of Φ_{II} vs d/a for different values of n_1 (n_2=1.457 and R = 0.4).

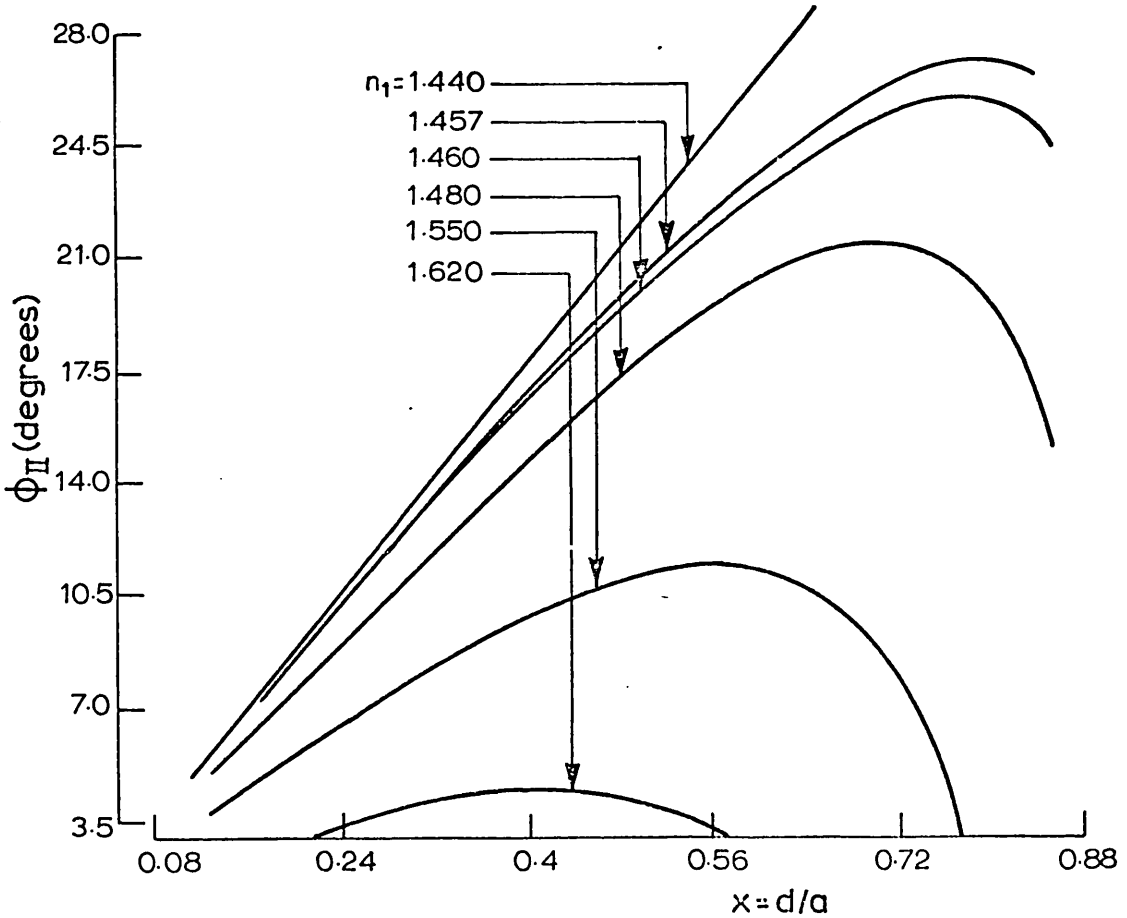

Fig. 6.13. Plots of Φ_{II} vs. d/a for different values of n_1 (n_2=1.457 and R = 0.6).

hollow fibres of acceptable perfection proved to be increasingly difficult beyond R = 0.6 and, as shown later in this chapter, imperfections in the geometry of the fibre can reduce the accuracy of the measurement. Moreover, by increasing R, the slope of the Φ_{IIm} vs. n_1 curve, especially at the higher end of the index range decreases and hence the accuracy of the measurement falls. Furthermore, as shown later in section 6.6.2, fibres of $R>0.5$ introduce specific problems when measurements are to be carried out on anisotropic cores.

In summary, the method described above affords the measurement of core refractive indices within the approximate range of 1.46 - 1.60.

To cover the full refractive index range of organic crystals, then, it was necessary to find another method of measurement applicable in the approximate range of 1.60-1.90. In this respect, it was thought that there may exist features in the pattern which are of undetectable intensity in the scattering pattern obtained from an ordinary optical fibre (having usually n_1-n_2 of the order of 0.01), and they may become pronounced and detectable when n_1-n_2 is large. It was logical to think that if such features (or feature) existed an obvious cause for them would be the rays which in their journey within the fibre cross-section undergo a reflection at the core - cladding boundary. Such a ray would be of very low irradiance in cases where $n_1 - n_2 \simeq 0.01$, but appreciable when $n_1-n_2 \gtrsim 0.1$.

In the first attempt to analyse this case, two rays were considered. Both of these are traced in Fig. 6.15. One is refracted into the cladding, reflected from the core-

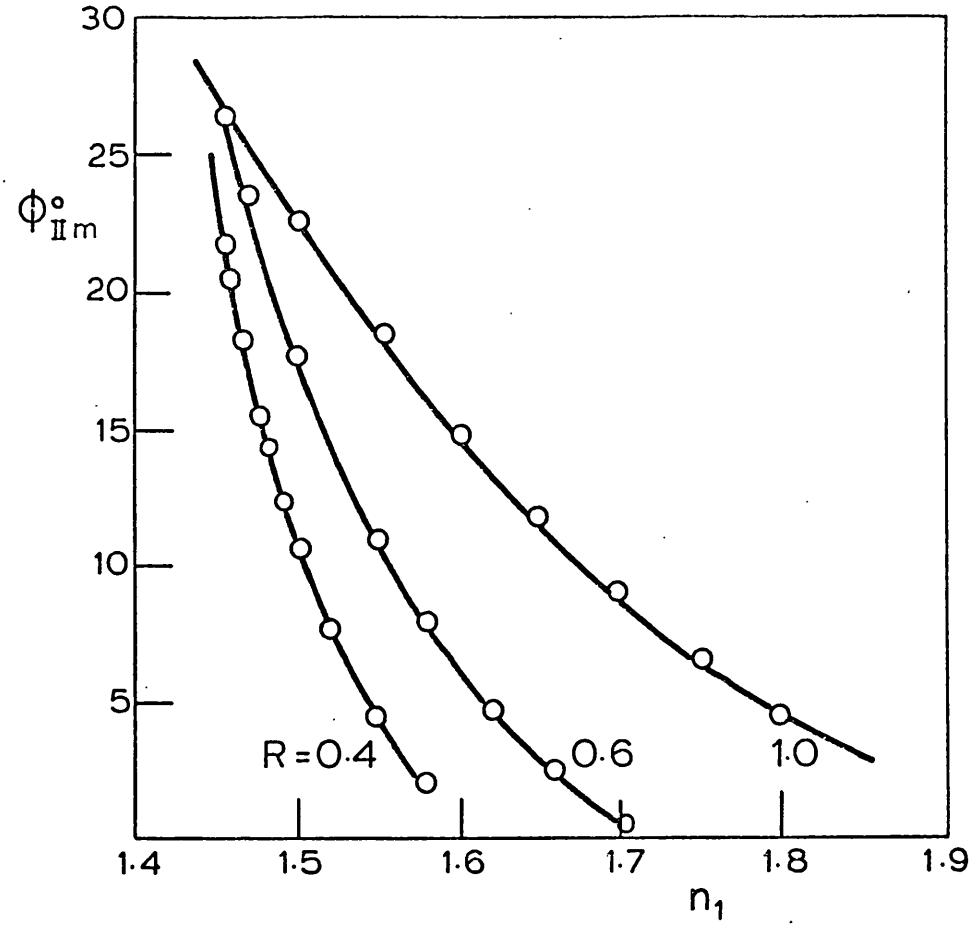

Fig. 6.14. Plots of Φ_{IIm} vs. n_1 (n_2=1.457).

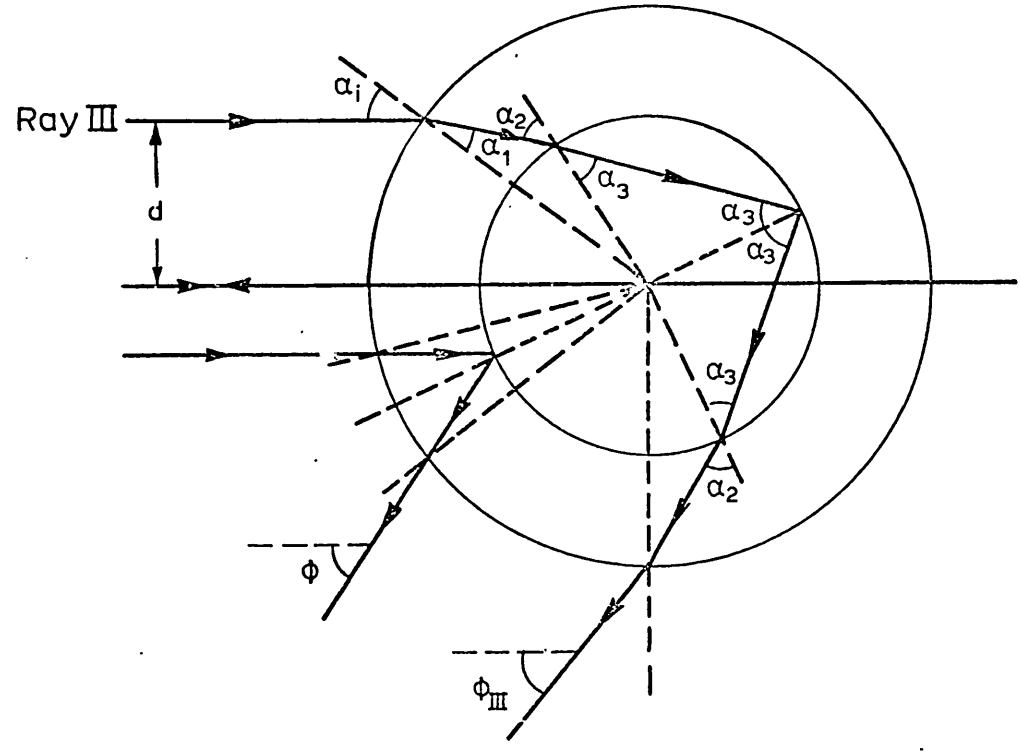

Fig. 6.15. Cross-section of fibre, showing paths of back scattered rays undergone a reflection at core-cladding boundary.

cladding boundary back into the cladding and finally emerges from the fibre after refraction at the cladding-air interface. The other (ray III) is refracted into the cladding and the core, reflected by the core-cladding boundary, travels through core and cladding again, and finally emerges from the fibre with a deviation angle Φ_{III}. The behaviour of the first ray was studied by calculating its deviation angle from the geometry of Fig. 6.15, and it was concluded that no significant features can be expected to be caused by this type of ray. Its behaviour was like the reflection rays considered in the previous sections. However, a study of the ray III showed that it exhibits interesting features:

As in the previous cases, a parallel-polarized monochromatic and collimated beam of light, is assumed to be incident upon the fibre. The deviation angle for ray III (Φ_{III}) follows from the geometry of Fig. 6.15:

$$\Phi_{III} = 4\alpha_3 - 2(\alpha_2 + \alpha_i - \alpha_1) \qquad (6.3.1)$$

with

$$\alpha_i = \text{Arc sin } x \quad , \quad \alpha_1 = \text{Arc sin } \left(\frac{x}{n_2}\right)$$

$$\alpha_2 = \text{Arc sin } \left(\frac{x}{n_2 R}\right) \text{ and } \alpha_3 = \text{Arc sin } \left(\frac{x}{n_1 R}\right)$$

where

$$R = \frac{b}{a} \quad \text{and} \quad x = \frac{d}{a} \quad ;$$

a, b, n_1, n_2 and d are the same as defined in the previous sections.

Plots of Φ_{III} vs. x for various values of n_1 are given in Figs. 6.16 and 6.17. These were plotted by computer

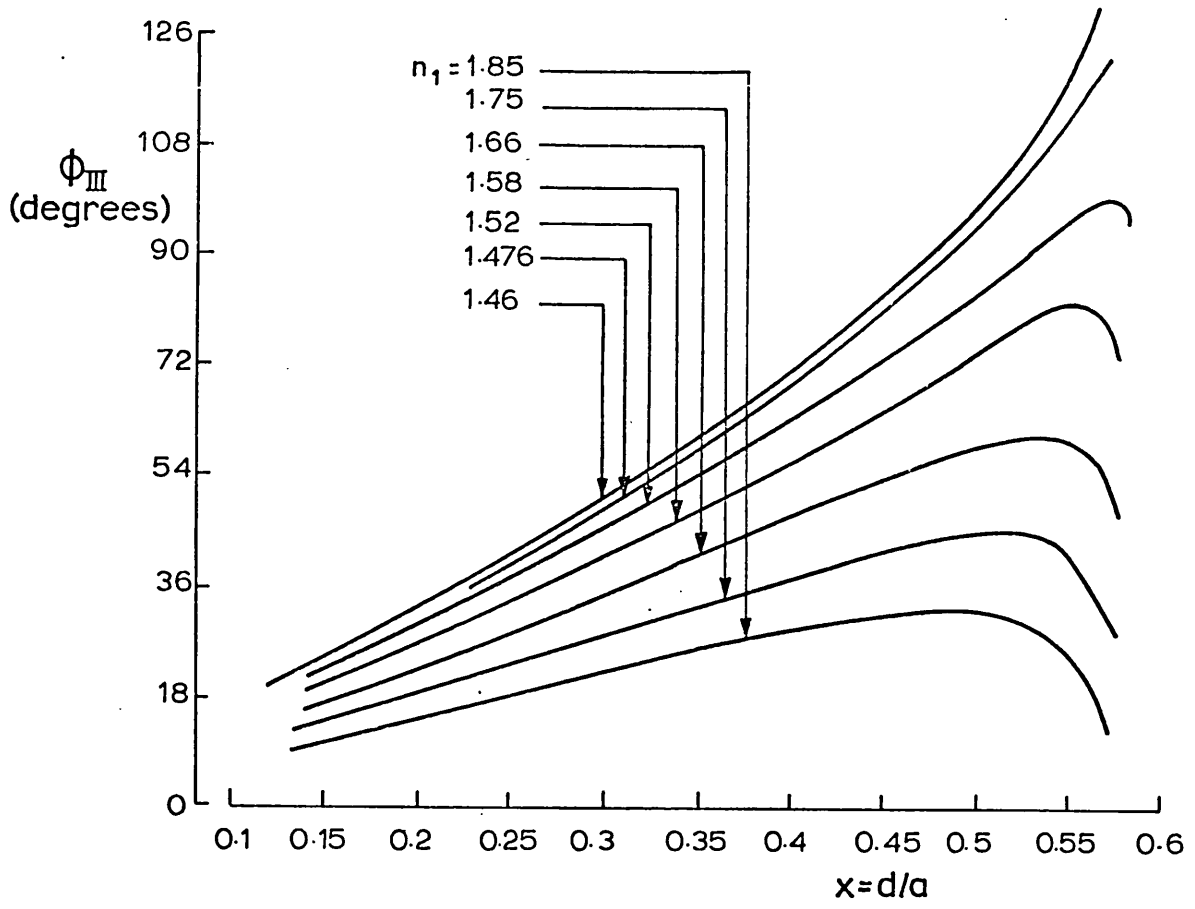

Fig. 6.16. Plots of Φ_{III} vs. d/a for different values of n_1 (n_2=1.457 and R = 0.4).

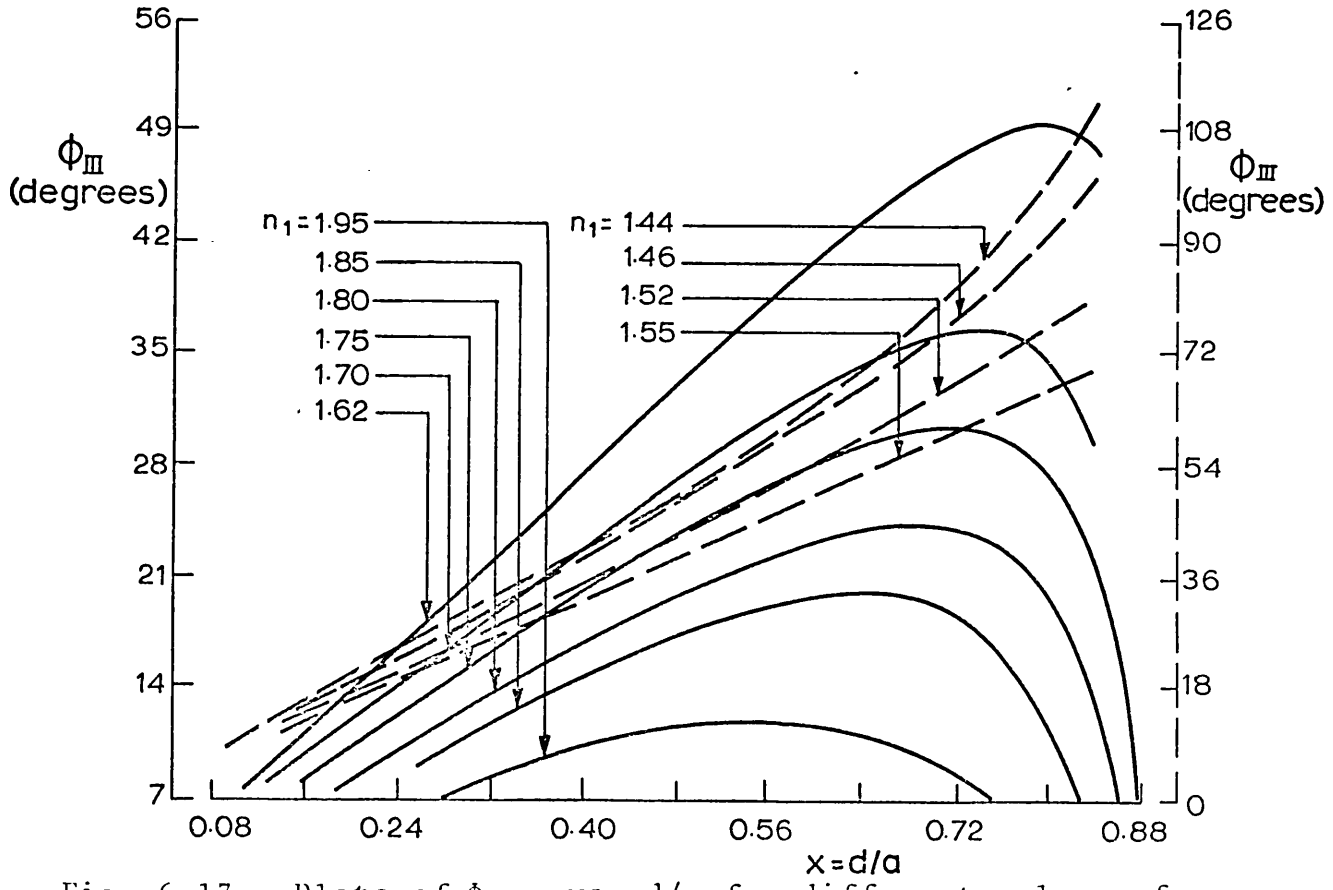

Fig. 6.17. Plots of Φ_{III} vs. d/a for different values of n_1 (n_2=1.457 and R = 0.6).

using Eq. (6.3.1). The cladding is assumed to be silica (n_2 = 1.457) and R is 0.4 and 0.6 in Figs. 6.16 and 17 respectively. It is apparent from these curves that ray III has a behaviour very similar to ray II, with the difference that the maximum of its deviation angle (Φ_{IIIm}) occurs at much larger angles. The intensity of the pattern can be related to $1/\frac{d\Phi_{III}}{dx}$, which, similarly to the case of ray I and ray II, predicts a maximum intensity at Φ_{IIIm} followed by a cut off due to the fact that there is no ray III beyond this angle. For a deviation angle Φ_{III}, Fig. 6.16 and (6.17) predicts the existence of two different III rays. Due to the interference between these two rays the intensity of the pattern before Φ_{IIIm} is expected to be spatially modulated. The study of the intensity variation may result in valuable information about the geometry of the fibre. However, this is not the main concern here and the analysis is left for the future. The specifications of the pattern in the region of Φ_{IIIm} theoretically predicted here were all later experimentally verified. A plot of intensity against angular position at about Φ_{IIIm} recorded experimentally is shown in Fig. 6.18.

The significance of this feature of the back scattering pattern in the refractive index measurement can be understood from Fig. 6.19 where Φ_{IIIm} is plotted against the core refractive index. The plots were made by computer by numerical calculation of the maximum values of Eq. (6.3.1). It can be deduced from Fig. 6.19 that by measurement of Φ_{IIIm} from the back scattering pattern of a fibre of R = 0.4, core refractive indices from about 1.52 to 2.0 can be measured. This range decreases to about 1.60-2.0 in the case of R = 0.6. It immediately follows that the discovered

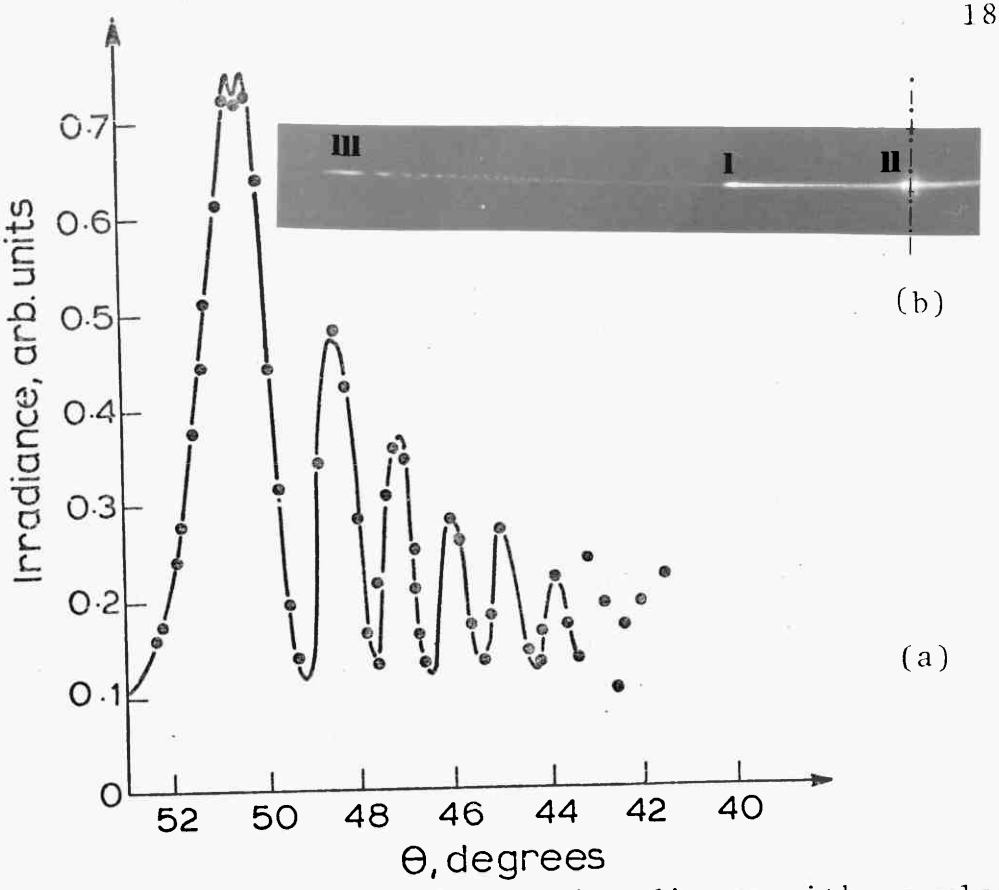

Fig.6.18. (a) Observed variation of irradiance with angular position at about Φ_{IIIm} for a fibre of n_1=1.651, n_2=1.471 and R=0.535. (b) Photograph of a back scattering pattern, showing features at Φ_{Im}, Φ_{IIm} and Φ_{IIIm}.

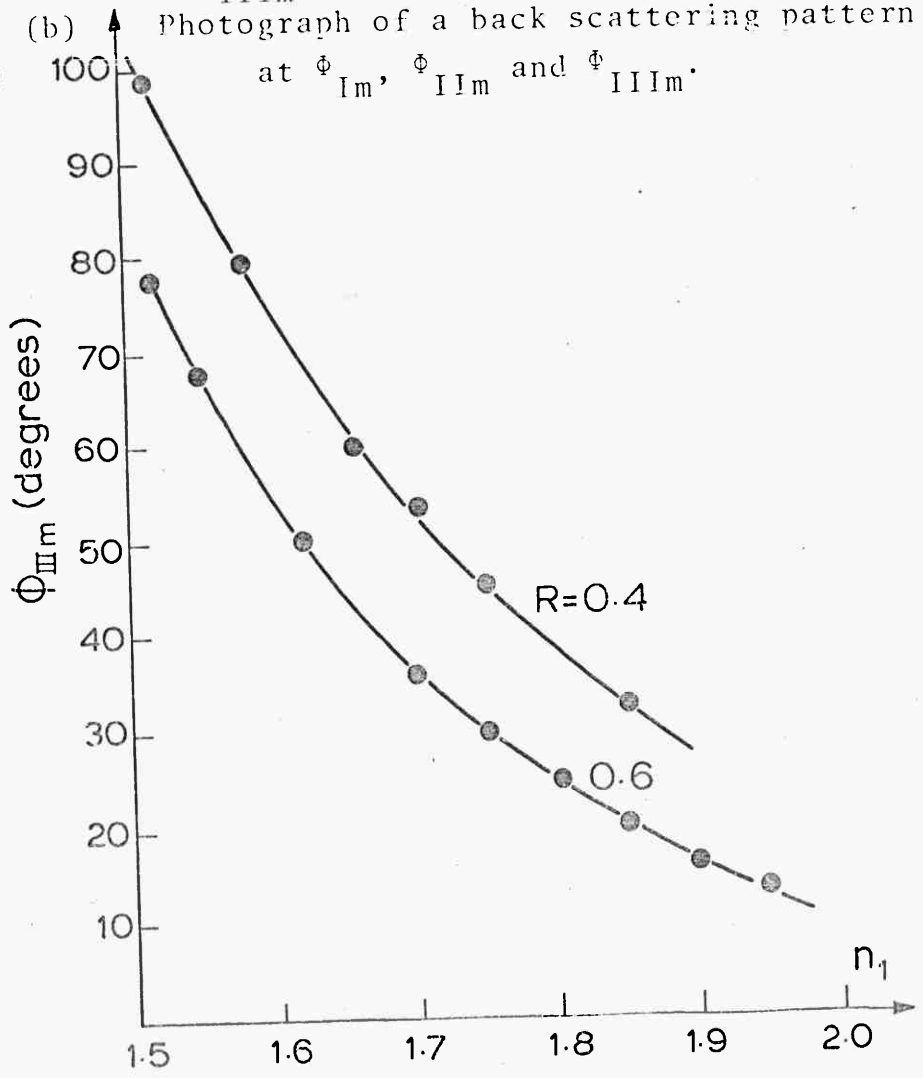

Fig. 6.19. Plots of Φ_{IIIm} vs. n_1 (n_2 = 1.457).

feature of the back scattering pattern (at Φ_{IIIm}) is an ideal complement for that occurring at Φ_{IIm}, and allows refractive index measurements for the full range of organic crystals.

6.4 The Accuracy of Measurements: Isotropic Core

It was shown in the previous section that the refractive index of the core can be obtained by measurement of either Φ_{IIm}, for indices within the approximate range of 1.46-1.60, or Φ_{IIIm}, for those in the approximate range of 1.60-1.90. It follows from Figs. 6.14 and 6.19 that an accuracy of 0.1 in the measurement of Φ_{IIm} of Φ_{IIIm} corresponds to an accuracy better than 1 part in 10^3 in indices measured in the middle of the ranges mentioned. The accuracy is higher at lower end of the index range and in both cases, decreases towards the higher end of the range. The measurement of both Φ_{IIm} and Φ_{IIIm} becomes difficult when they occur near to Φ_{Im} (about 27^o and 26^o for silica and pyrex cladding, respectively). The problem could easily be overcome by using a fibre of different R when the feature to be measured occurred between 20^o - 30^o; this, as follows from Figs. 6.14 and 6.19, shifts the angular positions.

Refractive indices corresponding to the angular data measured depend on both the geometry of the fibre and the refractive index of the cladding and hence the accuracy of index measurement also depends on the accuracy with which these factors are known. This matter is discussed in detail below. In this discussion the cladding refractive index, n_2, is assumed to be about 1.471 which was the measured value for

the fibres used in our experimental work. Also, for similar reasons R is assumed to be about 0.500. All curves given are plotted by computer using the appropriate equations presented previously in this Chapter.

(a) A plot of Φ_{IIm} vs. R for a fibre of $n_1 = 1.500$ and $n_2 = 1.471$ is shown in Fig. 6.20. It can be deduced from the slope of the curve at about R = 0.500 that an error of 0.001 in the measurement of R will cause an error of 0.03^o in the value obtained for Φ_{IIm}. Similarly, Fig. 6.21 shows a plot of Φ_{IIIm} vs. R for a fibre of $n_1 = 1.700$ and $n_2 = 1.471$. In this case the error in the measurement of Φ_{IIIm}, corresponding to an error equal to 0.001 in the measurement of R is 0.1^o; indicating that Φ_{IIIm} is much more sensitive to the geometry of the fibre than Φ_{IIm}.

(b) In Fig. 6.22, Φ_{IIm} is plotted against n_2 for a fibre of $n_1 = 1.520$ and R = 0.500. The slope of the curve shows that an error of 0.001 in cladding refractive index, n_2, presents an error of 0.11^o in the measurement of Φ_{IIm}. Similar considerations of a plot of Φ_{IIIm} vs. n_2 for a fibre of $n_1 = 1.650$ and R = 0.500 (Fig. 6.23) reveal that an error of 0.001 in n_2 causes an error equal to 0.16^o in the measurement of Φ_{IIIm}.

(c) In all of the theoretical reasoning presented in this Chapter, fibres were assumed to be perfectly circular. A departure from circularity will also cause an error in the measurements of Φ_{IIm} and Φ_{IIIm}. A major imperfection of this kind is the ellipticity of the fibre, usually introduced during the pulling process or inherited from the original preform. An elliptical fibre produces, in general, an asymmetric back scattering pattern where locations of the

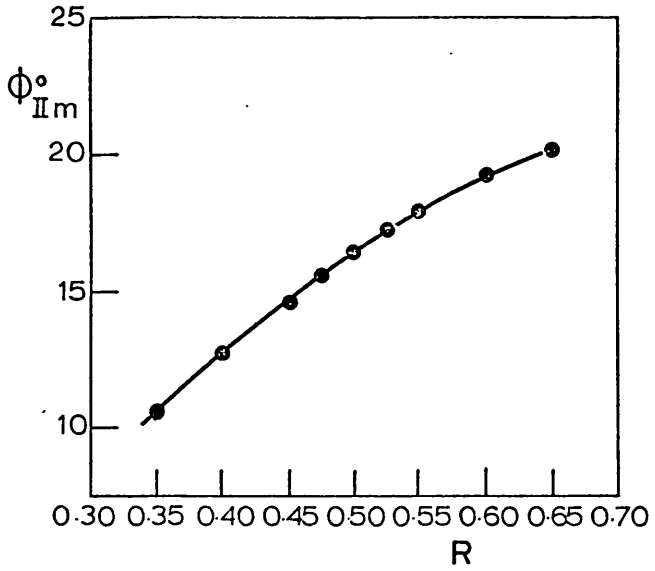

Fig. 6.20. Plot of Φ_{IIm} vs. R (n_1 = 1.500 and n_2 = 1.471).

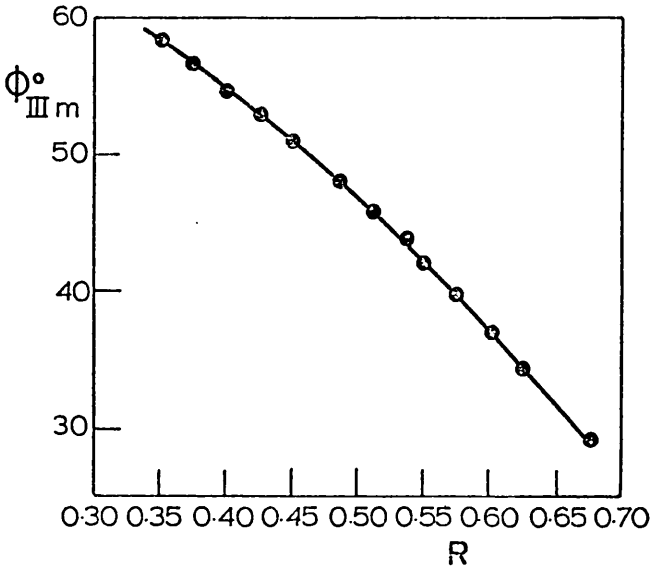

Fig. 21. Plot of Φ_{IIIm} vs. R (n_1 = 1.700 and n_2 = 1.471).

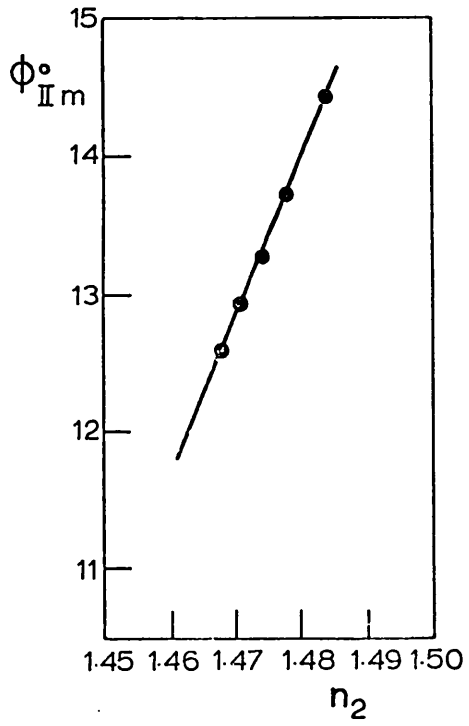

Fig. 6.22. Plot of Φ_{IIm} vs. n_2 (n_1 = 1.520 and R = 0.50)

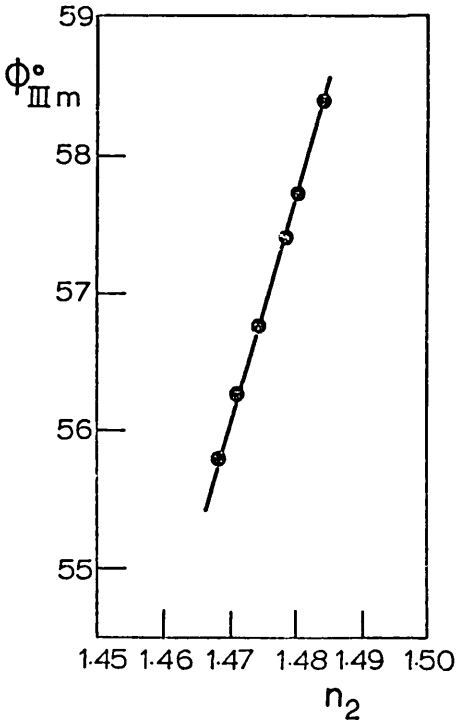

Fig. 6.23. Plot of Φ_{IIIm} vs. n_2 (n_1 = 1.65 and R = 0.50).

features discussed depend on the relative position of the axes of the ellipse to the direction of the incident beam; for example values of Φ_{Im} measured on the two sides of $\theta = 0$ (see Fig. 6.1), Φ^{+}_{Im} and Φ^{-}_{Im} respectively, will not be equal. Presby (1976) employed this effect for the ellipticity measurement of optical fibres. It can be deduced from his calculations and experimental results reported, that a 1% ellipticity ($a'/a = 0.99$, Fig. 6.24a) can cause a maximum error of about 0.6^{o} in the measurement of Φ_{Im}. Even higher levels of error are to be expected in the case of Φ_{IIIm} due to its greater sensitivity to the geometry of the fibre. Such an error would totally dominate the refractive index measurements described in the previous section, especially in our experiments where a crude method of pulling had been used for making the hollow glass fibres. The solution of the problem was, again, deduced from the data published by Presby. Fig. 6.24b, shows that the change in the angular location of the feature related to Φ_{Im} by rotation of an elliptical fibre around its axis is symmetrical about that expected for a perfect circular fibre (the dashed line in Fig. 6.24b). Thus the error due to the ellipticity of the fibre would be avoided if the maximum and minimum values of Φ_{Im}, measured in the course of the rotation of the fibre around its axis, were averaged to obtain the corresponding value for a circular fibre; this can be done in both sides of $\theta = 0$:

$$\Phi_{Im} = \frac{(\Phi^{+}_{Im})_{max.} + (\Phi^{+}_{Im})_{min.}}{2}$$

or

$$\Phi_{Im} = \frac{(\Phi^{-}_{Im})_{max.} + (\Phi^{-}_{Im})_{min.}}{2}$$

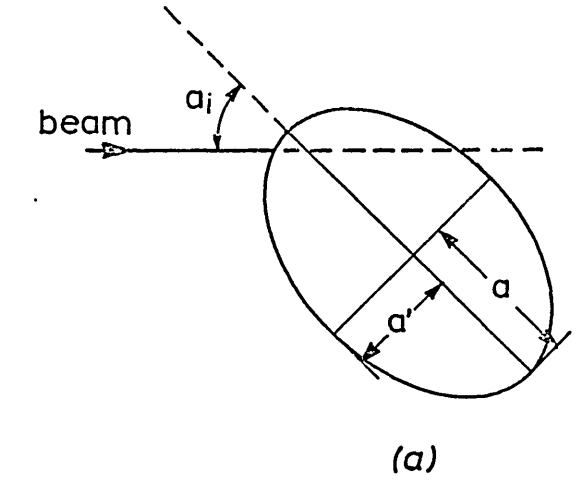

(a)

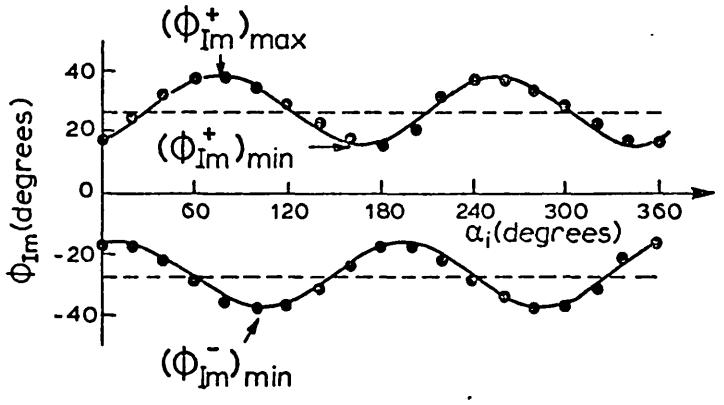

(b)

Fig. 6.24. Graphs, showing the variation of Φ_{Im} for an elliptical fibre with α_i(b); α_i is related to the position of the fibre in front of the beam as shown in (a).

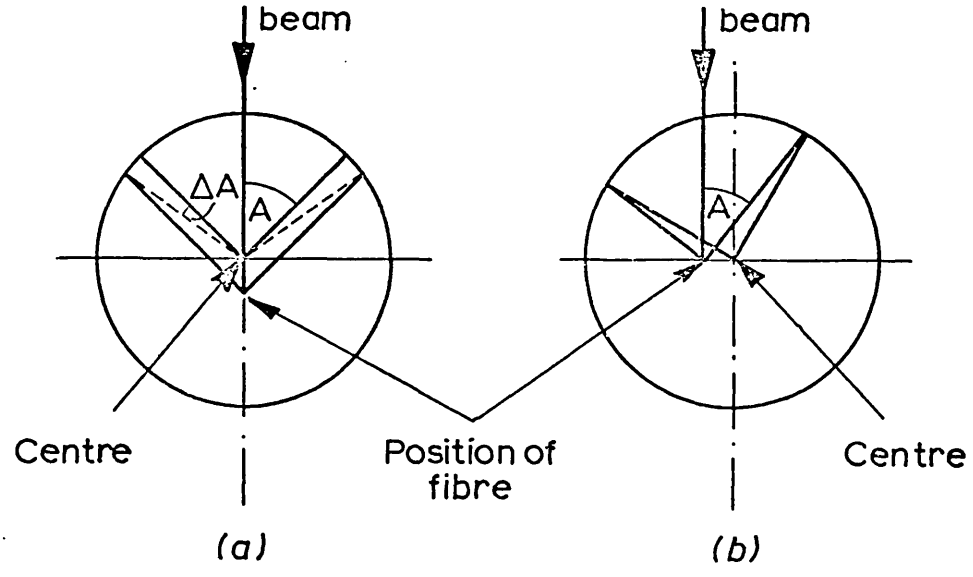

Fig. 6.25. Diagrams, showing errors caused by departure fo the fibre from centre of the detector rotation, (a) parallel to the beam, (b) perpendicular to the beam.

Only the effect of ellipticity on Φ_{Im} was discussed here, but due to the geometrical similarities between rays I, II and III, Φ_{IIm} and Φ_{IIIm} would also behave in a similar manner when the ellipticity is introduced. In our experimental work, all measurements were carried out as described above, to avoid the ellipticity errors.

Other types of departure from the ideal configuration would also introduce errors in the measurements. Another case,for instance,is the non-concentricity of the core with respect to the outer cladding periphery. The mathematical study of this error proved to be difficult but it was thought that with the method of measurement described, this type of error would also be reduced until negligible.

(d) In the measurement of the angular locations of the features of the pattern, of course, the fibre must be located at the cnetre of the rotation of the detector. An off-centred fibre causes errors in the measurements. The effect of this eccentricity, in two different directions has been shown in Fig. 6.25a and b.

It follows from the geometry of Fig. 6.25a that a displacement from the centre equal to d in the direction of the incident beam causes an error in the measurement of the location of a feature occuring at $\theta = A^{o}$, given by

$$|\Delta A| = \frac{180\ d \sin A}{\Pi\ R} \quad \text{(degrees)} \qquad (6.4.1)$$

where R is the length of the detector arm. For $A = 50^{o}$ (about the middle of the Φ_{IIIm} range) and using a 0.5 metre detector arm an error of 0.09^{o} is predicted for a displacement of 1 mm. For $A = 10^{o}$ (about the middle of the Φ_{IIm} range) in similar conditions the predicted error is 0.02^{o}.

It can be concluded from the geometry of Fig.6.2 that, to a first order approximation, the error corresponding to displacement in the direction perpendicular to the incident beam is zero.

In a systematic refractive index measurement by the techinque presented here, errors quoted in a, b, c and d can, in principle, be reduced to any required level. A stock of hollow fibres enough for thousands of measurements can be drawn from a few centimeters of carefully constructed preform. With a controlled pulling technique the diameter of the fibres obtained can be kept reasonably constant, and hence the value of R would be constant to a very good approximation (R is only weakly dependent on a). The value of R and n_2 for the stock of fibres can be measured by various methods to any desired accuracy. Also the source of error studied in (d) can be decreased to a very low level, by using an accurate spectroscopy table with necessary equipment for centring the fibre. Thus, the accuracy of the method will only depend on the accuracy in measurement of the angular locations of the scattering features. At the moment we are unable to predict a maximum value for this accuracy, since in our experiments the total error was dominated by those quoted in a, b and d (as described below) and more refined experiments are necessary in this respect. However, this accuracy can be enhanced by the use of a narrower slit before the detector and a longer detector arm in conjunction with modern counting equipment. This would however, decrease the signal level and thus a more sophisticated detection and amplification unit would be necessary. Also the number of measurement points would be increased and direct feeding of the measured values into a computer (to be processed and plotted)

would be beneficial. In our experiments the width of the slit was 1 mm and the detector arm about 0.5 m, resulting an accuracy of about 0.1^{o}, such an accuracy, assuming that other errors are negligible (a, b, c and d) would render an accuracy of $1x10^{-3}$ in the measurement of refractive index. It is expected that by the refinements mentioned, the accuracy could be enhanced beyond this level.

In our experiments, both R and n_2 were measured with an accuracy of ± 0.001, and the accuracy in placing the fibre at the centre of the table was ± 1 mm. These led to errors of 0.1^{o}, 0.16^{o} and 0.09^{o} in the measurement of Φ_{IIIm} respectively. The corresponding errors in Φ_{IIm} were 0.06^{o}, 0.11^{o} and 0.02^{o}. Also an error of 0.1^{o} was estimated for the location of the points in the pattern. Thus the maximum error levels were estimated to be ± 0.45^{o} and ± 0.29 for Φ_{IIIm} and Φ_{IIm} respectively, from the summation of the errors described. These correspond to errors of about ± $5x10^{-3}$ and $3x10^{-3}$ in the core refractive index measurement.

In this Section the various factors affecting the accuracy of the index measurements using a back scattering pattern were considered. This study, which has not been previously reported, would also be useful in the assessment of the optical fibre parameters.

6.5 Measurement of Refractive Index Dispersion.

The method described in Section 6.3 can similarly be applied to dispersion measurements. For this purpose a white light source in conjunction with a monochromator allows Φ_{IIm} and Φ_{IIIm} to be measured as a function of λ. Higher accuracies

are to be expected in this measurement since factors causing errors discussed in the previous Section will be constant, and the change in the pattern is only due to dispersion of refractive indices of the core and cladding. Assuming that the dispersion characteristic of the cladding glass is precisely known, the accuracy of measurement would only depend on the accuracy of the detection of the change in the pattern.

Presby (1974) measured the dispersion of unclad silica fibres by detection of the change in the location of Φ_{Im} to an accuracy of 2×10^{-4} in the variation of n. Similar accuracies would be expected when the measurement is carried out on Φ_{IIIm} or Φ_{IIm}.

6.6 Measurement of Core Refractive Index: Anisotropic Core

6.6.1 Reflection from a dielectric interface

A ray of light incident upon the interface between two dielectrics with respective permittivities of ε_1 and ε_2, undergoes reflection and refraction. The fraction of the incident power reflected is different for the two perpendicular polarizations shown in Fig. 6.26a. The reflection coefficient for a ray polarized perpendicular to the plane of incidence (i.e. parallel with the interface, Ray 1 in Fig. 6.26a) is given by (see, e.g. Jordan and Balmain,1968)

$$\frac{P_r}{P_i} = \left(\frac{\cos\theta - \sqrt{(\varepsilon_2/\varepsilon_1)-\sin^2\theta}}{\cos\theta + \sqrt{(\varepsilon_2/\varepsilon_1)-\sin^2\theta}}\right)^2 \qquad (6.6.1)$$

with

θ = angle of incidence,

P_r = reflected power, and

P_i = incident power

and the reflection coefficient for a ray polarized parallel with the plane of incidence (Ray 2 in Fig. 6.26a) is given by

$$\frac{P_r}{P_i} = \left(\frac{(\varepsilon_2/\varepsilon_1)\cos\theta - \sqrt{(\varepsilon_2/\varepsilon_1) - \sin^2\theta}}{(\varepsilon_2/\varepsilon_1)\cos\theta + \sqrt{(\varepsilon_2/\varepsilon_1) - \sin^2\theta}} \right)^2 \qquad (6.6.2)$$

Eqs. (6.6.1 and 2) can also be written in terms of the refractive indices of the two media since

$$\frac{\varepsilon_2}{\varepsilon_1} = \left(\frac{n_2}{n_1}\right)^2 .$$

Plots of Eqs. (6.6.1) and (6.6.2) are given in Fig. 6.26b for $n_1 = 1.457$ (silica) and $n_2 = 1$, which indicate their different behaviour: The reflection coefficient for ray 1 continuously increases with θ, but in the case of ray 2 it vanishes at an incidence angle called the Brewster angle. By equating Eq. (6.6.2) to zero the Brewster angle follows:

$$B = \text{Arc tan } \left(\frac{n_2}{n_1}\right) \qquad (6.6.3)$$

Thus for a ray polarized as ray 2, when the incidence angle is equal or near the Brewster angle the irradiance of the reflected ray is zero or minimal.

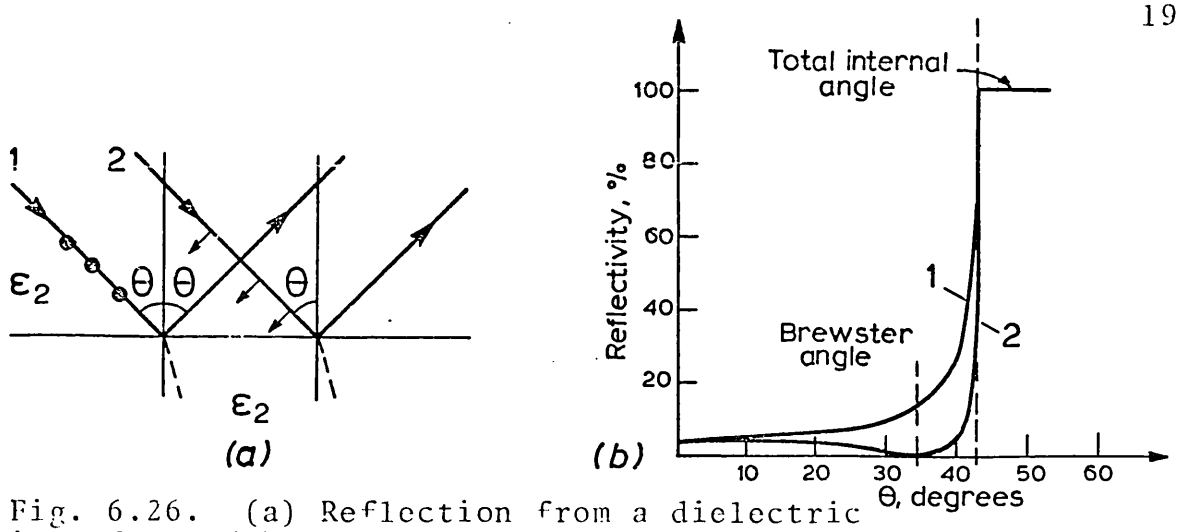

Fig. 6.26. (a) Reflection from a dielectric interface, (b) Variation of reflectivity with incidence angle for two different polarizators.

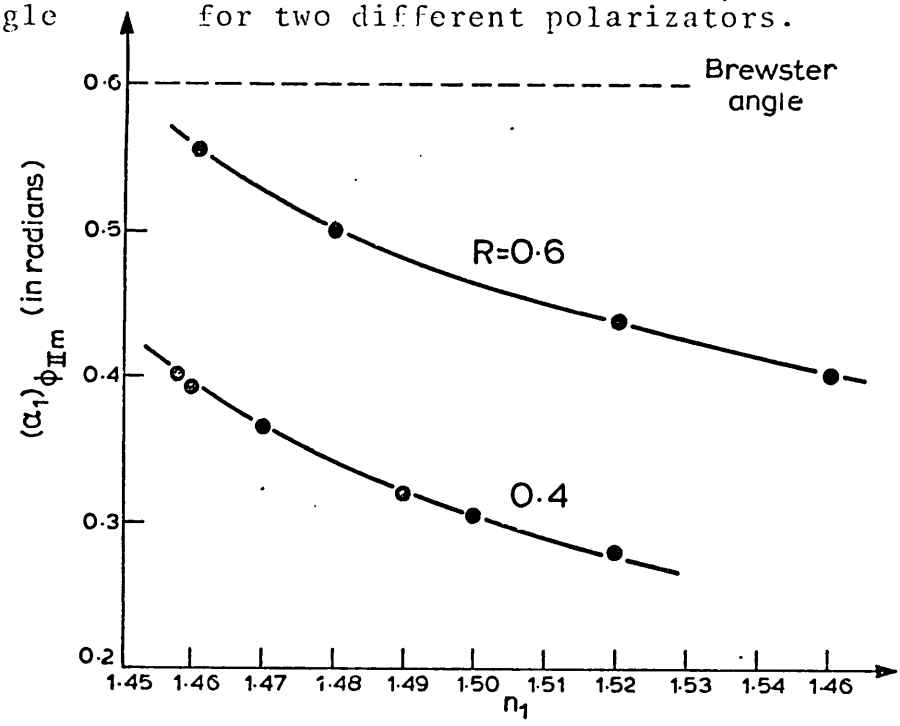

Fig. 6.27. Plots of $(\alpha_1)_{\Phi_{IIm}}$ vs. $n_1 (n_2=1.457)$, dashed line indicates the Brewster angle.

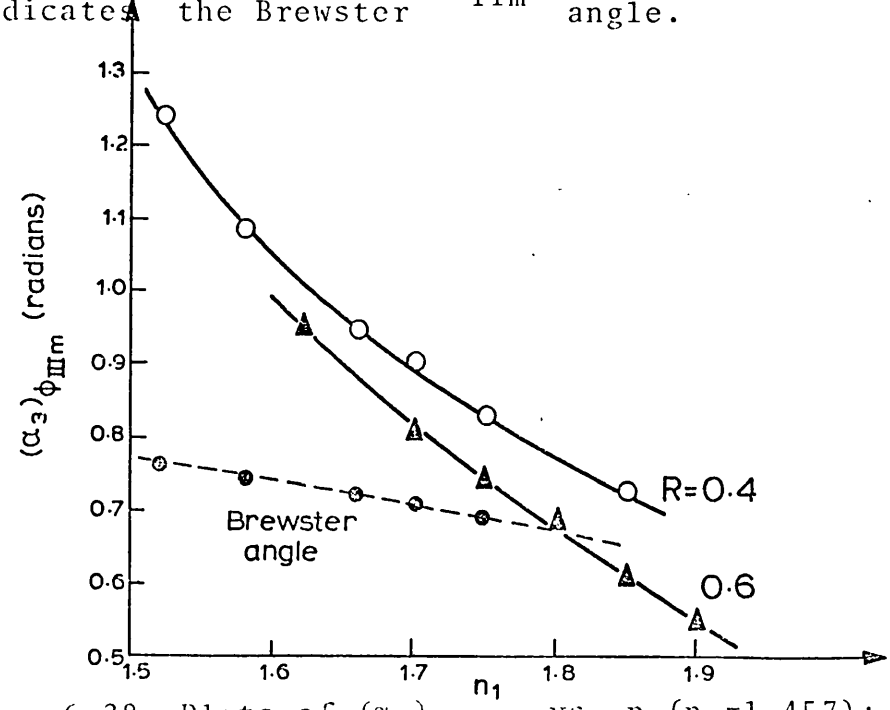

Fig. 6.28. Plots of $(\alpha_3)_{\Phi_{IIIm}}$ vs. $n_1 (n_2=1.457)$; dashed curve indicates the variation of Brewster angle with n_1.

6.6.2 Back scattering pattern with light polarized perpendicular to the fibre axis

In the various theoretical considerations of the back scattering patterns presented previously in this Chapter, incident beams polarized parallel to the fibres axes (parallel-polarized) were assumed although this factor was not made use of in the deductions made. Furthermore, in all of the work reported on various non-destructive measurements on optical fibres using scattering patterns (e.g. refractive indices of core and cladding, diameters and ellipticity measurements) parallel polarizations have been used, and the scattering pattern when the incident beam is perpendicular to the fibre axis (perpendicular polarization) has not so far been considered. The reason for this neglect is as follows:

As shown in Fig. 6.3 ray I undergoes a reflection at the fibre - air interface with an incidence angle of r, which follows from the geometry of Fig. 6.3

$$r = \text{Arc sin}\,\frac{x}{n} \qquad (6.6.4)$$

where $x = d/a$ and n is the refractive index of the fibre. For the ray which emerges from the fibre with a deviation angle equal to Φ_{Im}, then, the reflection angle is

$$(r)_{\Phi_{Im}} = \text{Arc sin}\frac{(x)_{\Phi_{Im}}}{n} \qquad (6.6.5)$$

Considering a fibre made of silica (n = 1.457), the value of $(x)_{\Phi_{Im}}$ obtained from Eq.(6.1.3) is about 0.79. This results in

$$(r)_{\Phi_{Im},\ \text{silica}} \simeq 33^{o}$$

The Brewster angle for reflection from a silica-air interface obtained from Eq. (6.6.3) is about 34^{o}. Thus rays which take part in the construction of the features of the pattern occuring at about Φ_{Im} (which has been the most useful feature of the scattering pattern in the optical fibres assessment) undergo reflection at an angle near to the Brewster angle. This will not cause problems if the ray is parallel-polarized, but will drastically decrease the intensity of the pattern near Φ_{Im} when perpendicular polarization is used. It is worth mentioning here that a similar coincidence occurs in the case of internal reflection within rain droplets, which accounts for the rainbow being highly polarized.

It is shown below that this problem in fact causes little difficulty in relation to the features of the pattern occuring at Φ_{IIm} and Φ_{IIIm} respectively.

As shown in Fig. 6.7, ray II also undergoes a reflection at the cladding-air boundary. The reflection angle follows from the geometry of Fig. 6.7:

$$\alpha_1 = \text{Arc sin } (\frac{x}{n_2}) \qquad (6.6.6)$$

where $x = d/a$ and n_2 is the cladding refractive index. For the ray emerging from the fibre with deviation angle Φ_{IIm}, then

$$(\alpha_1)_{\Phi_{IIm}} = \text{Arc sin } (\frac{(x)_{\Phi_{IIm}}}{n_2}) \ .$$

$(x)_{\Phi_{IIm}}$ depends on the refractive indices and the geometry of the fibre (R). For the case of fibres with silica cladding and with values of R equal to 0.4 and 0.6, $(x)_{\Phi_{IIm}}$ for different

core refractive indices can be obtained from Figs. 6.12 and 6.13 respectively, from which the respective $(\alpha_1)_{\Phi_{IIm}}$ can be calculated. Plots of $(\alpha_1)_{\Phi_{IIm}}$ vs. n_1 for fibres of R = 0.4 and 0.6 are given in Fig. 6.27. In this figure the dashed line shows the Brewster angle for the reflection of ray II. It is apparent from Fig. 6.27 that $(\alpha_1)_{\Phi_{IIm}}$ in both cases of R = 0.4 and 0.6, is significantly different from the Brewster angle for the whole of the refractive index range of interest. Thus the feature of the back scattering pattern corresponding to Φ_{IIm} is also readily obtained using a perpedicular-polarized incident beam. We conclude that the core index measurement can also be carried out with this mode of polarization using the method described in Section 6.3 for parallel polarization.

Fig. 6.15 shows that ray III undergoes a reflection at the core-cladding boundary. The angle of reflection follows from the geometry of Fig. 6.15:

$$\alpha_3 = \text{Arc sin } (\frac{x}{n_1 R}) \qquad (6.6.7)$$

Hence the reflection angle for the ray emerging from the fibre with a deviation angle of Φ_{IIIm} is given by:

$$(\alpha_3)_{\Phi_{IIIm}} = \text{Arc sin } (\frac{(x)_{\Phi_{IIIm}}}{n_1 R}).$$

$(x)_{\Phi_{IIIm}}$ values are obtained from Figs. 6.16 and 6.17, which in turn result in the plots of $(\alpha_3)_{\Phi_{IIIm}}$ vs. n_1 shown in Fig. 6.28. It is important to notice that in this case, since reflection takes place at the core-cladding boundary, the Brewster angle

of the reflecting interface varies with n_1 (unlike the previous case). In Fig. 6.28 the dashed curve shows the variation of the Brewster angle of the core-cladding interface (n_2 = 1.457), with n_1. It is apparent from Fig. 6.28 that in the case of R = 0.4 the reflection and Brewster angles remain distinct from each other for nearly the full range of n_1, but for R = 0.6 they intersect at about n_1 = 1.8. This implies that using a silica fibre of R = 0.6, measurement of core indices of about 1.8 (approximate range of 1.75 - 1.83) is difficult, because the feature of the pattern at Φ_{IIIm} will be of minimal intensity. If this problem arises, it can be solved by using a fibre of smaller R, as follows from Fig. 6.28. (This effect occurs at lower core indices if pyrex fibres are used; and a sharp fall in the intensity of the pattern at Φ_{IIIm} was observed for certain values of n_1, in good agreement with calculations.)

As a conclusion: In the case of perpendicular polarization both features at Φ_{IIm} and Φ_{IIIm} occur in the same manner and have the same significance as in the case of parallel polarization, and perpendicular-polarized beams can also be used for core index measurements using the method described in Section 6.3. This was also experimentally verified by measurement of n_1 for an isotropic fibre using two different polarizations; the results were equal within experimental error.

6.6.3 Uniaxial crystal core

In this Section the method of refractive index measurement described in Section 6.4 is extended to cover the

measurement of both n_e and n_o (extraordinary and ordinary refractive indices) of a uniaxial crystal core. It is assumed that the optic axis of the crystal is parallel with the fibre axis. This assumption is consistent with our growth experiments on the uniaxial crystal benzil and also the results reported on the growth of another uniaxial crystal, acetamide (S. Al Shookri, Private Communication).

If the incident light is parallel-polarized, according to the above mentioned assumption, it "sees" a core of refractive index n_e. Thus the measurement of n_e can be made directly from one of the features occuring at Φ_{IIm} or Φ_{IIIm}, as described in Section 6.3. On the other hand a perpendicular-polarized beam sees the fibre as having a core of refractive index n_o, and thus n_o can be measured from the features of the scattering pattern obtained. These measurements were carried out for benzil, and the experimental procedure together with the results obtained are given in Section 6.7.

It was assumed above that the optic axis of the crystal was parallel to the fibre axis, but as shown in Chapter 3, this is not always exactly true, and usually these two directions diverge by a few degrees. This divergence varies from one sample to another and it is preferable to choose one in which this angle is virtually zero for refractive index measurements. However, this selection is usually made using a polarizing microscope for which the accuracy of the crystal orientation detection is less than $\pm 1^o$. As a result when a sample is chosen for refractive index measurements, there is an uncertainty of about $\pm 1^o$ with respect to the orientation of the crystal core. Thus it is important

to study the potential errors in the measurments of n_e and n_o due to this problem.

The cross-section of the index ellipsoid of the crystal perpendicular to the incident beam is shown in Fig. 6.29. If the optic axis of the crystal is parallel to the fibre axis, using a parallel-polarized incident beam n_e will be measured, but if it was "tilted" with an angle ΔA, the measured value in the same conditions would be n'_e (Fig. 6.29). It follows from the geometry of Fig. 6.29 that

$$n_e'^2 = n_o^2 \sin \Delta A + n_e^2 \text{Cos}^2 \Delta A.$$

ΔA is an angle of the order of 1^o; employing the relevant approximations

$$n'_e = n_e - \frac{\Delta A^2 (n_e^2 - n_o^2)}{2n_e}$$

or

$$|n'_e - n_e| = 0.5 \, \Delta A^2 \, \frac{n_e^2 - n_o^2}{n_e} \qquad (6.6.7)$$

Eq. (6.6.7) gives the magnitude of the error in the measurement of n_e due to misalignment of the crystal within the fibre. For a typical case of $\Delta A = 1^o$, $n_e = 1.60$, $n_o = 1.55$,

$|n'_e - n_e| = 1.5 \times 10^{-5}$

which is two orders of magnitude smaller than the errors discussed in Section 7.5. Even an error corresponding to a misalign ment of 3^o will not detract from the overall accuracy of the method. Similarly, the error in the measurement of n_o with a perpendicular-polarized beam is

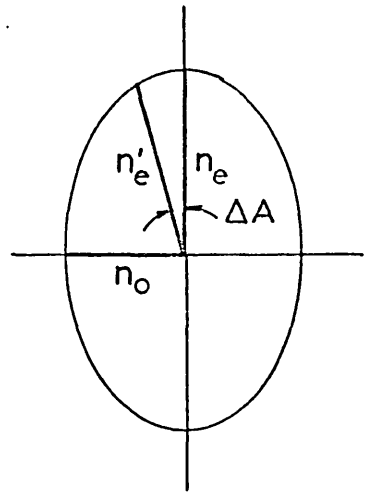

Fig. 6.29. Diagram, showing errors in index measurements caused by a ΔA^o misalignment of the crystal.

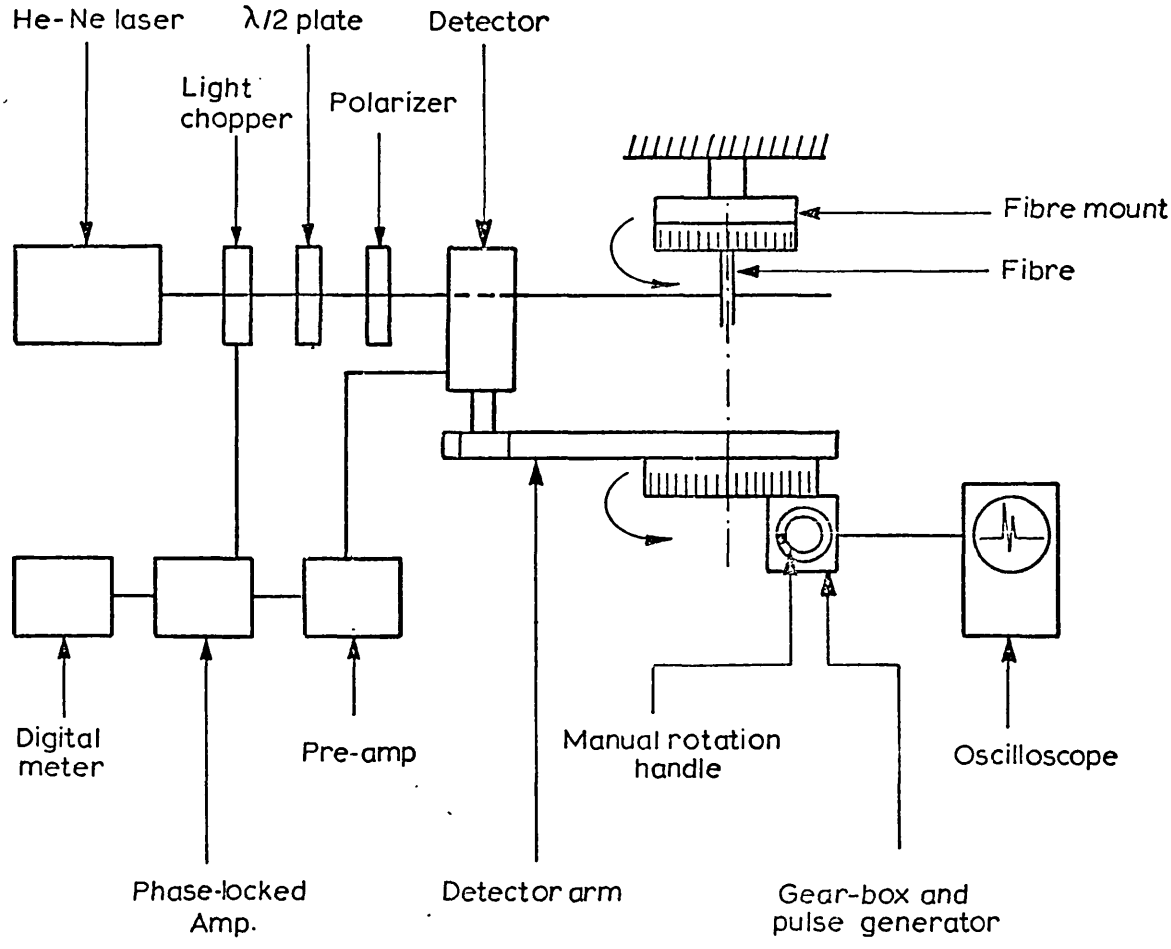

Fig. 6.30. Experimental setup to measure the core refractive index.

$$|n_o' - n_o| = 0.5\,\Delta A^2\,\frac{n_e^2 - n_o^2}{n_o} \qquad (6.6.8)$$

which is not appreciably different from Eq. (6.6.7).

Thus it has been shown in this Section that both n_e and n_o values of a uniaxial crystal can be measured on one piece of crystal cored fibre without difficulty. n_e is obtained when the incident beam is parallel-polarized, and the measurement of n_o immediately follows by rotation of the polarization by 90^o. It was also shown that the accuracies obtained were essentially the same as those discussed in section 6.4 for the case of an isotropic core.

The dispersion of both n_e and n_o can also be measured as described in Section 6.5.

6.6.4 Biaxial crystal core

The growth of several biaxial crystals within glass fibres was discussed in Chapter 3, and it was shown that they generally grow with one of their principal dielectric axes parallel to the fibre axis. The two other dielectric axes, then, are perpendicular to the fibre axis. The measurement of the refractive index in the direction parallel to the axis of the fibre, say n_z for the sake or argument, can be carried out as described in the previous Section, i.e. by using a parallel-polarized incident beam. However measurements of n_x and n_y are not so simple: A perpendicular-polarized beam "sees" a core refractive index which is a weighted average of n_x and n_y, which depends on the position of the fibre cross-section with respect to the incident beam. The refractive index "seen", then, varies with rotation of

the fibre around its axis, and so the pattern features corresponding to Φ_{IIm} and Φ_{IIIm} also change their positions with rotation of the fibre. The situation is very much like that for an elliptical fibre, in which both Φ_{IIIm} and Φ_{IIm} pass through minima and maxima by rotation of the fibre. It is reasonable to think that by observation of this change of position for say Φ_{IIIm}, and especially the measurement of $(\Phi_{IIIm})_{MAX}$ and $(\Phi_{IIIm})_{MIN}$, the two refractive indices (n_y and n_x) can be obtained. However a theoretical study of this relationship proved to be difficult and a solution was not possible within the time available. The difficulty arises from the fact that a ray, entering the core in these conditions, no longer obeys Snell's law and its path is predictable by graphical methods (see e.g., Bloss, 1961). Thus, the calculations presented in Sections 6.1.2 and 6.3 must be reconsidered, accounting for this departure from Snell's law. Furthermore, the change in the locations of the pattern features by rotation of the fibre is due both to the change in core refractive index seen, and to the ellipticity of the fibre. The separation of these effects provides a further complication. However later a method was found by which these two effects could be separated with a reasonable accuracy; this will not be discussed here. The problem would be resolved if fibres of low ellipticity (<0.01%) were available.

In summary, further theoretical work is needed to obtain a more precise relation between the change in the locations of the pattern features due to rotation of the fibre and the transverse indices of the crystal.

6.7 Experimental

A schematic diagram of the experimental arrangement is shown in Fig. 6.30. A 5 mW C.W. polarized He-Ne laser beam was chopped at a frequency of 420 Hz and passed through a $\lambda/2$ plate and a polarizer by which its direction of polarization was controlled, and finally was laterally incident upon the fibre to be examined. The fibre placed vertically in a mount at the centre of the rotation of a long arm holding the detector. The detector arm could be rotated around the fibre manually with the help of a gear-box, and the angular position of the detector was measurable with an accuracy of 0.05^{o} using a simple opto-electronic arrangement which produced an electric impulse at each 0.05^{o} rotation of the arm. These were monitored on an oscilloscope to measure fine displacements of the arm. The light detector was a large area photodiode, in front of which slits of different width could be placed. The detected voltage was fed to a phase-locked amplifier (Brookdeal 9501D + Pre. Amp.5001) and measured after amplification. A photograph of the equipment used is presented in the Appendix.

Hollow fibres were drawn from pyrex capillary tubes. The pulling process was carried out manually using a simple furnace. For experimental verification of the index measurement method presented in this Chapter, fibres of different core refractive indices were needed. These were obtained by filling the hollow fibres with different liquids. The refractive indices of these liquids at 0.633 μm were measured by an Abbe refractometer before introduction into the fibres. The refractive index of the cladding glass was also measured

by the mentioned aparatus using lapped and polished samples from the original preforms. The accuracies of these measurements were ± 0.001.

Fibres of larger cross-sections were preferred in these experiments since the corresponding scattering patterns were of higher intensities. The fibres used had external diameters in the range of 100 - 400 μm. The diameter of the laser beam was about 2 mm, so in all cases the intensity of the beam could be assumed constant throughout the fibre cross-section. The inner to outer diameter ratios (R) of the fibres were measured both by travelling microscope and high-magnification photography of the cross-sections. The accuracy of the values obtained was estimated to be not better than ± 0.007, which was unacceptable for the refractive index measurement (see Section 6.4). For this reason, the scattering method itself was employed for an accurate measurement of R (see below).

6.7.1 Experimental procedure

The optical bench and the laser beam were adjusted to be horizontal using conventional methods. In order for the fibre to stand vertical in the mount it was adjusted so that the scattering pattern observed around the full 360^{o} (on the walls of the laboratory) was aligned in a horizontal plane. The method used for centring the fibre was rather crude and its accuracy was not better than ± 1 mm. The position of the detector was so that the centre of the slit was aligned with the scattering plane. The length of

the detector arm was adjustable; it was in the range of 30-50 cm in different experiments.

The features of the back-scattering pattern corresponding to Φ_{Im}, Φ_{IIm} and Φ_{IIIm} were readily observable by the naked eye (unless they did not exist or were of very low intensity, as predicted in the previous section for special circumstances). In order to measure Φ_{IIm} or Φ_{IIIm}, the variation of intensity about ($\sim \pm 1^{o}$) the corresponding feature was measured and plotted against the angular position. The values of both Φ_{IIm} and Φ_{IIIm} were, then, read off from the angular positions corresponding to 0.44 I_m, where I_m is the maximum intensity measured.

Due to the ellipticity of the fibres the location of each feature moved slightly on rotation of the fibre. To avoid the related errors, each feature was measured at its maximum and minimum angular positions and the average value taken. Using the method presented by Presby (1976) the ellipticity of the fibres used was estimated: In all cases the ellipticity was below 1%.

All measurements were carried out for both sides of the back scattering pattern (left and right hand side of $\theta = 0$), and averaged to decrease the errors originating from misplacement of the fibre.

Values of R for fibres used, apart from microscopic measurements, were measured by filling them with a liquid of known refractive index and measurement of the location of Φ_{IIIm}. The value of R, then, followed from plots similar to the one given in Fig. 6.21. Only Φ_{IIIm} was employed for this purpose since as shown in Section 6.4 it is about 3 times more sensitive than Φ_{IIm} in this respect.

6.7.2 Results

(a) Isotropic core: Φ_{IIm} and Φ_{IIIm} were measured for several filled fibres, using both parallel and perpendicular polarizations. All of the measurements were in agreement with the calculated values within the estimated errors of the experiments (Section 6.4). Results are summarized in Table 6.1. In the case of Fibre 10, when perpendicular polarization was used the feature obtained at Φ_{IIIm} was of low intensity and not measurable. This was due to the effect discussed in Section 6.6.2 (see Fig. 6.28).

(b) Anisotropic core: Φ_{IIIm} corresponding to n_e and n_o of the uniaxial crystal benzil were measured using parallel and perpendicular polarization respectively. Only 2 mm (the diameter of the beam) of void free crystal cored fibre was needed for these measurements, which were, as shown in Chapter 3, easy to obtain. The z-axis of the crystal in the sample used was parallel with the fibre axis as examined with a polarizing microscope. The results obtained are given in Table 6.1.

The n_z of the biaxial crystal m-dihydroxybenzene was obtained by measurement of Φ_{IIm} using parallel polarization. The examination of the sample under the polarizing microscope had shown that one of the principal dielectric axis of the crystal was parallel to the fibre axis. The measurement described here, identified this axis as the c-axis of the crystal. The result of the measurement is given in Table 6.1. Also the n_z of the biaxial crystal m-dinitrobenzene was measured in a similar way. However the accuracy of the

TABLE 6.1. Results of refractive index measurements

Exp. No.	Core material	n_1^* (λ=633nm)	n_2 (λ=633nm)	R	Polarization	Φ^o_{IIm} calculated	Φ^σ_{IIm} measured	Φ^o_{IIIm} calculated	Φ^o_{IIIm} measured
3	liqu.	1.527	1.471	0.377	∥	7.54	7.5±0.3	-	-
6	liqu.	1.527	1.471	0.535	∥	13.04	13.2±0.3	-	-
7	liqu.	1.554	1.471	0.535	∥	9.59	9.5±0.3	-	-
8	liqu.	1.650	1.471	0.535	∥	1.94	~1.5$^+$	52.57	52.7±0.4
9A	liqu.	1.611	1.471	0.534	∥	4.35	~5.0$^+$	61.50	61.2±0.4
9B	liqu.	1.611	1.471	0.534	⊥	4.35	~5.0$^+$	61.50	61.3±0.4
10A	liqu.	1.731	1.471	0.534	∥	-	-	38.90	39.4±0.4
16A	benzil	1.674	1.471	0.475	∥	-	-	53.9^{++}	53.7±0.4
16B	benzil	1.651	1.471	0.475	⊥	-	-	58.7^{++}	58.4±0.4
14A	mDHB	1.62	1.471	0.662	∥	6.6^{++}	6.7±0.3	-	-

* Measured by Abbe refractometer in the case of liquids; extracted from literature in the case of crystals.

\+ Estimated by distance measurement when the pattern was projected on a screen.

++ Extracted from related curves.

measurement was low since the core and cladding refractive indices were close to each other (see Section 6.3).

In the cases of the biaxial crystals examined when perpendicular polrization was used, the features of the patterns shifted in position on the rotation of the fibre. The prediction of this effect has already been recorded in Section 6.6.4. An attempt to obtain the values of n_x and n_y from this behaviour failed probably since at that stage of the work the separation of this effect from that due to the ellipticity of the fibre had not been achieved. Further theoretical and experimental work is needed to clarify the position regarding this aspect of the work.

6.8 A Proposed Method for the Measurement of Electro-optic and Electrochromic Coefficients in Organic Solids

The steepness of the irradiance vs. angle curves at about Φ_{IIm} and Φ_{IIIm} provides a highly sensitive means for the measurement of changes in core refractive index (n_1), especially if the change is oscillatory at a predetermined frequency.

It can be deduced from a discussion carried out in Section 6.4 that a change as much as ± 0.0005 in n_1 shifts the position of the irradiance vs. angle plot by ~± 0.05^o. A typical plot obtained at about Φ_{IIIm} is given in Fig. 6.31. If a detector was located at point D, as follows from Fig. 6.31, it would detect a change of ± 20% in the irradiance due to the shift mentioned.

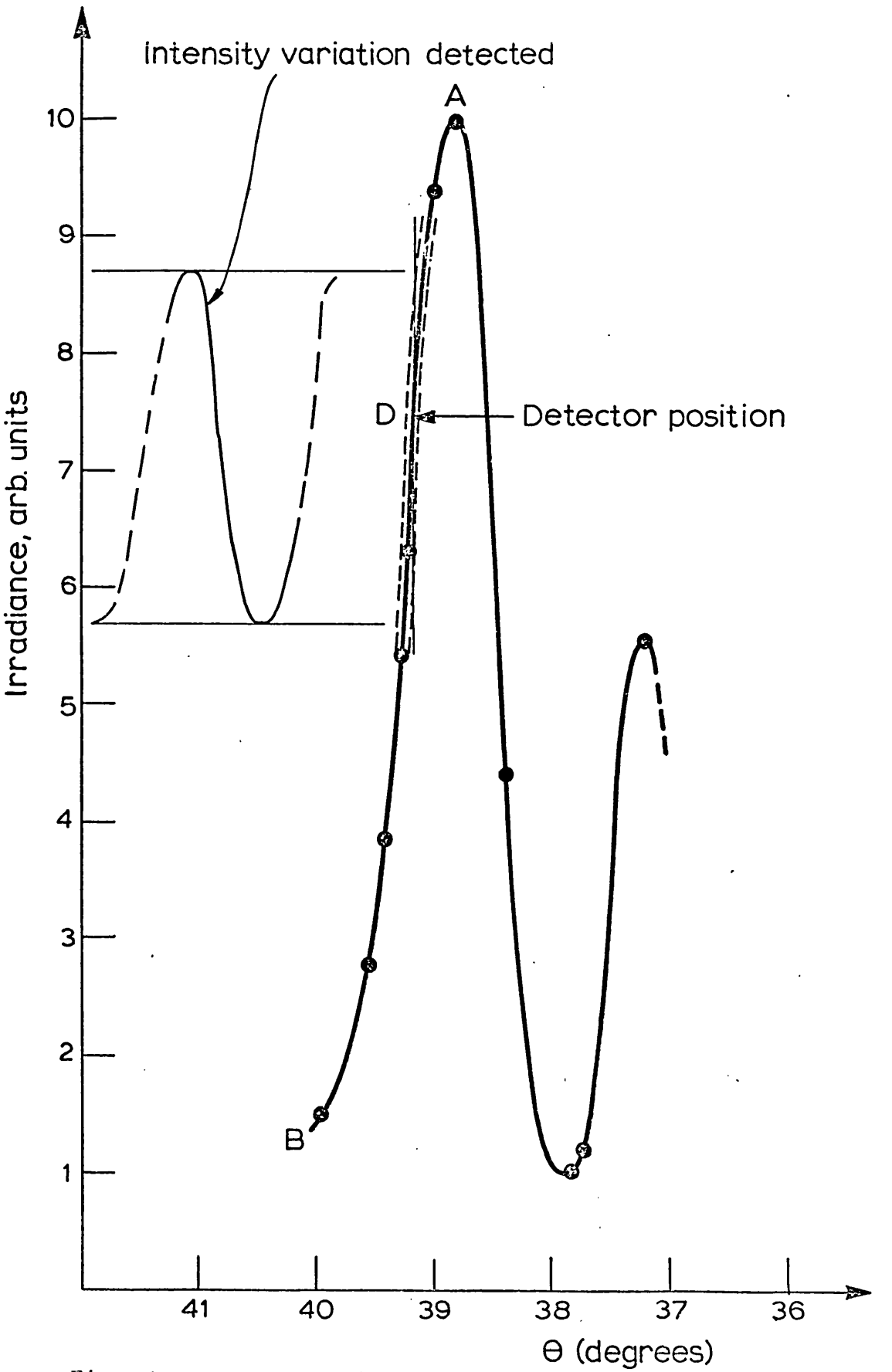

Fig. 6.31. Plot of irradiance vs. angular position (at about Φ_{IIIm}) and its shift due to a $\pm$ 0.0005 change in core index (n_1 = 1.731, n_2 = 1.471 and R = 0.534).

Now, let the core be an electro-optic crystal so that its refractive index will vary with an alternating electric field applied to the fibre. Changes of the order of 10^{-5} in the refractive index of electro-optic materials are obtainable with applied fields. Hence the detector would "see" a ~0.4% modulation in the irradiance of the point D. The detection and amplification of such a signal level is readily made using a phase sensitive unit; an 0.4% variation is equivalent to ~ -48 dB signal to background ratio, while common phase sensitive detectors can recover signals 100 dB below background, and hence even higher sensitivities can be expected.

By measurement of the signal, the magnitude of the index change due to the applied field and hence the related electro-optic coefficient can be calculated. Different coefficients should be obtainable by altering the direction of the field and polarization of the incident beam with respect to the fibre.

It has been shown by Stevenson (1973) that the maximum light transmission modulation due to an electrochromic effect results when $\alpha t = 1$, where α is the absorption coefficient of the crystal and t is the thickness of the sample traversed by the light. Since this effect is measured near the absorption band edge, α is large and hence a thin slice of the crystal is required (e.g. the optimum thickness in Stevenson's experiments was ~0.3 mm).

Considering Figs. 6.7a and 6.15, rays forming the scattering features around Φ_{IIm} and Φ_{IIIm} traverse the core twice, i.e. the passage of light through the crystal is equivalent to that in a crystal slice of thickness ~2b, where b is the core diameter; e.g. using a fibre of 150 μm i.d. is

equivalent to a sample of ~0.3 mm thickness.

Now, let a wide-area detector be positioned in the pattern so that it covers the area between A and B (Fig.6.31), and an alternating field be applied to the fibre in the correct orientation. Due to the electro-chromic effect, the absorption coefficient of the crystal and hence the irradiance at Φ_{IIIm} or Φ_{IIm} will change. Such variation in intensity which is of the order of 1% for an applied field of ~1 k v mm^{-1} (mNA) can be detected without difficulty.

Alterations in the position of the related scattering feature due to electro-optic effect (discussed above) should not interfere with this measurement as the whole area from A to B is covered by the detector. Similarly, the electro-optic measurements described above should preferably be carried out at wavelengths far from the absorption band to prevent the electro-chromic effects from influencing the measurement.

CONCLUSION

The main concern at the outset of the work was the problems encountered with the preparation of CCOF's. These problems were identified and the effects of various factors, either related to the material or to the growth conditions, were studied. It was shown that by optimizing the growth conditions and the choice of appropriate materials, problems such as void formation and unfavourable crystal orientation are soluble. As examples long lengths of good quality void-free fibre grown crystals of benzil and mDNB were obtained. The preparation has progressed to the state which would allow the start of systematic device application studies.

Regarding the fibre-optic applications of the specimens, pilot experiments were carried out in which it was shown that void-free fibres guide the light without major scattering, and with an acceptable level of attenuation. Some solutions for the major practical difficulties involved with utilization of the CCOF for system applications such as end preparatio n and connection were given. Device applications of CCOF were discussed and it was shown that apart from their use in optical communication, CCOF's present attractive features in the field of non-linear optics.

The importance of the fibre growth technique in preparation and assessment of organic materials was demonstrated and various examples given to prove its practicality in this respect. Considering the very large number of possible organic materials such quick methods of assessment are clearly of some importance.

It seems logical at this stage, to abstract the technique of crystal growth presented in Chapter 3 (Fibre Growth) from the concept of CCOF and to consider it solely as a powerful method of micro-crystal growth for organic materials. It may well find applications in other branches of science and technology; the fact that most of the applications considered here were related to the field of optics stemmed solely from the interests of the author. For example there are no obvious reasons why it should not be applied to the growth of inorganic crystals (e.g. semiconductors) of suitable melting points, compatible with the fibre composition. The advantage of such a micro-technique for growth of rare or toxic materials can easily be seen.

REFERENCES

Amoros J.L., Canut M.L. and Neira (1965), Proc. Roy. Soc. A., 285, 370.

Anderson D.B. and Boyd J.T. (1971), Appl. Phys. Letters, 19, 266.

Ayers S., Faktor M.M., Marr D. and Stevenson J.L., J. Mater. Sci., 7, 31.

Bloembergen N. (1965), Nonlinear-optics, Benjamin (N.Y.) (1961),

Bloss F.D. (1961), An Introduction to the Methods of Optical Crystallography, Holt, Rinehart and Winston (N.Y.).

Bond, W.L. (1951), Rev. Sci. Instr. 22, 344.

Born M. and Wolf E. (1975), Principals of Optics, Pergamon Press (Oxford).

Boyd J.T. (1972), IEEE J. Quantum Electron., QE-8, 788.

Burrus C.A., Stone J. and Dental A.G., Electron. Letters, 12, 600.

Chandrasekhar S. (1954), Proc. Indian Acad. Sci. Section A, 39, 243.

Chu P.L. (1976), Electron. Letters, 12, 14

Cozens J.R. (1976), Electron. Letters, 12, 413.

Davies D.E.N. and Kingsley S.A. (1974), Electron. Letters, 10, 21.

Davies D.E.N. and Kingsley S.A. (1975), IEE International Conference on optical fibre communications, 165.

Dyott R.B., Stern J.R. (1971), Electron. Letters, 7, 82.

Everitt W.E. and Anner G.E. (1956), Communication Engineering, McGraw-Hill (London).

Franken P.A., Hill A.E., Peters C.W. and Winrich G. (1961), Phys. Rev., 7, 118.

Gloge D. (1971), Appl. Optics, 10, 2252.

Gloge D. and Marcatili (1973), B.S.T.J., 52, 1161.

Goell J.E. (1974), in Introduction to Integrated Optics ed. by Barnoski M.K., Plenum Press (London).

Gott J.R. (1971), J. Phys. B, 4, 116.

Guilland G., Le Helley M. and Mesnard G. (1970), Bull. Soc. Fr. Minearl. Cristallogr. 93, 131.

Hariguchi M. and Osanai H. (1976), Electron. Letters, 12,310.

Hazan J.P. and Bernard J.J. (1977), Electron. Letters, 13, 540.

Holoubek J. (1976), Appl. Optics, 15, 2751.

Hsieh J.J. (1977), AGARD Conference Preprint No. 219, 35-1.

Jeffery J.W. and Rose K.M. (1964), Acta Cryst., 17, 343.

Jephargnon J. (1971), IEEE J. Quantum Electron. 7, 12.

Jordan E.C. and Balmain K.G. (1968), Electromagnetic waves and Radiating Systems, Prentice-Hall (London).

Kaminow I.P. (1975), IEEE Trans. Microwave Theory Tech. MTT-23, 57.

Kapany N.S. (1967), Fibre Optics, Principles and Applications, Academic Press (N.Y.).

Kapany N.S. and Burke J.J. (1972), Optical Waveguides, Academic Press (N.Y.).

Keck D.B. (1976), in Fundamentals of Optical Fibre Communications ed. by Barnoski M.K., Academic Press (London).

Kerker M. and Matijevic E. (1961), J. Opt. Soc. Am. 51, 506.

Kogelnik H. (1975), in Integrated Optics, ed. by Tamir T., Springer (Berlin).

Koreshkov B.D. (1965), Sov. Phys. Cryst., 10, 355.

Kressel H. (1976), in Fundamentals of Optical Fibre Communications, ed. by Barnoski, M.K., Academic Press (London).

Kruger U., Pepperl R. and Schmidt U.J., Proc. IEEE, 61, 992.

Kurtz S.K. and Perry T.T. (1968), J. Appl. Phys., 39, 3798.

Kurtz S.K. and Robinson N.H. (1967), Appl. Phys. Letters, 10, 62.

Longaker P.R. and Roberts C.S. (1963), IEEE Trans. Microwave Theory Tech., MTT-11, 543.

Longhurst R.S. (1957), Geometrical and Physical Optics, Longmans (London).

Marcuse D. (1974), Theory of Dielectric Optical Waveguides, Academic Press (London).

Marcuse D. (1972), Light Transmission Optics, Princeton (N.J.).

Marcuse D. (1975), Appl. Optics, 14, 1528.

Marcuse D. and Presby H.M.(1975), J. Opt. Soc. Am., 65, 367.

Maurer R.D. (1973), in Introduction to Integrated Optics, ed. by Barnoski M.K., Plenum (London).

McMahon D.H. and Nelson A.R. ,(1977), AGARD Conference Preprint No. 219, Paper 17.

Miller S.E., Marcatili E.A.J. and Li T. (1973), Proc. IEEE, 61, 1703.

Morris P.J., Kirtisinghe D. and Strickland-Constable (1968), J. Crystal Growth 2, 97.

Nye J.F. (1957), Physical Properties of Crystals, Clarendon Press (Oxford).

Olshansky R. and Keck D.B. (1976), Appl. Optics, 15, 483.

Owen J.R. (1975), Ph.D. Thesis, University of London.

Owen J.R. and White E.A.D. (1976), J. Mater. Sci., 11, 2165.

Owen J.R. and White E.A.D. (1977), J. Mater. Sci., 12, 743.

Payne D.N. and Gambling W.A.(1975), Electron. Letters, 11, 116.

Peterson J., Steinrauf L.K., and Jensen L.H. (1960), Acta Cryst., 13, 104 .

Pfann W.G. (1968), Zone Melting, Wiley (London).

Presby H.M. (1973), J. Opt. Soc. Am., 64, 280.

Presby H.M. (1974), Appl. Phys. Letters, 24, 422.

Presby H.M. (1975), Appl. Optics., 15, 492.

Presby H.M. and Marcuse D. (1974), Appl. Optics, 13, 2682.

Rawson E.G. (1972), Appl. Optics, 11, 2477.

Robertson J.M. (1936), Proc. R. Soc. A., 157, 79.

Robertson J.M. and Ubbelohde A.R. (1936), Proc. R. Soc. A., 167, 122.

Rosenbaum F.J. (1965), IEEE J. Quntum Electron., QE-1, 367.

Rosenbaum J. and Kraus L. (1977), Appl. Optics, 16, 2204.

Snyder A.W. (1969), IEEE Trans. Microwave Theory Tech., MTT-17, 1130.

Soref R.A., McMahon D.H. and Nelson A.R. (1976), Appl. Phys. Letters, 28, 716.

Southgate P.D. and Hall D.S. (1972), J. Appl. Phys., 43, 2765.

Stevenson J.L. (1973), Ph.D. Thesis, University of London.

Stevenson J.L. (1973 II), J. Phys. D., 6, L13.

Stevenson J.L. (1977), J. Crystal Growth, 37, 116.

Stevenson J.L., Ayers S. and Faktor M.M. (1973), J. Phys. Chem. Solids, 34, 235.

Stevenson J.L. and Dyott R.B. (1974), Electron. Letters, 10, 449.

Stolen R.H., Bjorkholm J.E. and Ashkin A. (1974), Appl. Phys. Letters, 24, 308.

Stout G.H. and Jensen L.H. (1968), X-ray structure Determination, Collier-Macmillan (London).

Strickland-Constable R.F. (1968), Kinetics and Mechanism of Crystallization, Academic Press (London).

Taylor H.F. (1977), AGARD Conference Preprint No.219, Paper 1.

Taylor H.F. and Yariv A. (1974), Proc. IEEE, 62, 1044.

Tien P.K. (1971), Appl. Optics, 10, 2395.

Usugi N. and Kimura T. (1976), Appl. Phys. Letters, 29, 572.

Van de Hulst H.C. (1957), Light Scattering by Small Particles, Wiley (London).

Watkins L.S. (1974), J. Opt. Soc. Am., 64, 767.

Winchell A. (1954), Optical Properties of Organic Compounds, Academic Press (N.Y.).

Yariv A. (1976), Introduction to Optical Electronics, Holt, Rinehart and Winston (London).

Yariv A. (1976,II), Appl. Phys. Letters, 28, 88.

Zernike F. (1964), J. Opt. Soc. Am., 54, 1215.

Zernike F. and Midwinter J.E. (1973), Applied Non-linear Optics, Wiley (London).

Appendix

Photographs of some of the experimental setups:

Fig. I. Photograph of the optical bench arranged for observation of phase-modulation.

Fig. II. Photograph of the experimental setup for refractive index measurements.

Fig.III. Miniature furnace in connection,(a) with a steroscopic microscope, (b) polarizing microscope.

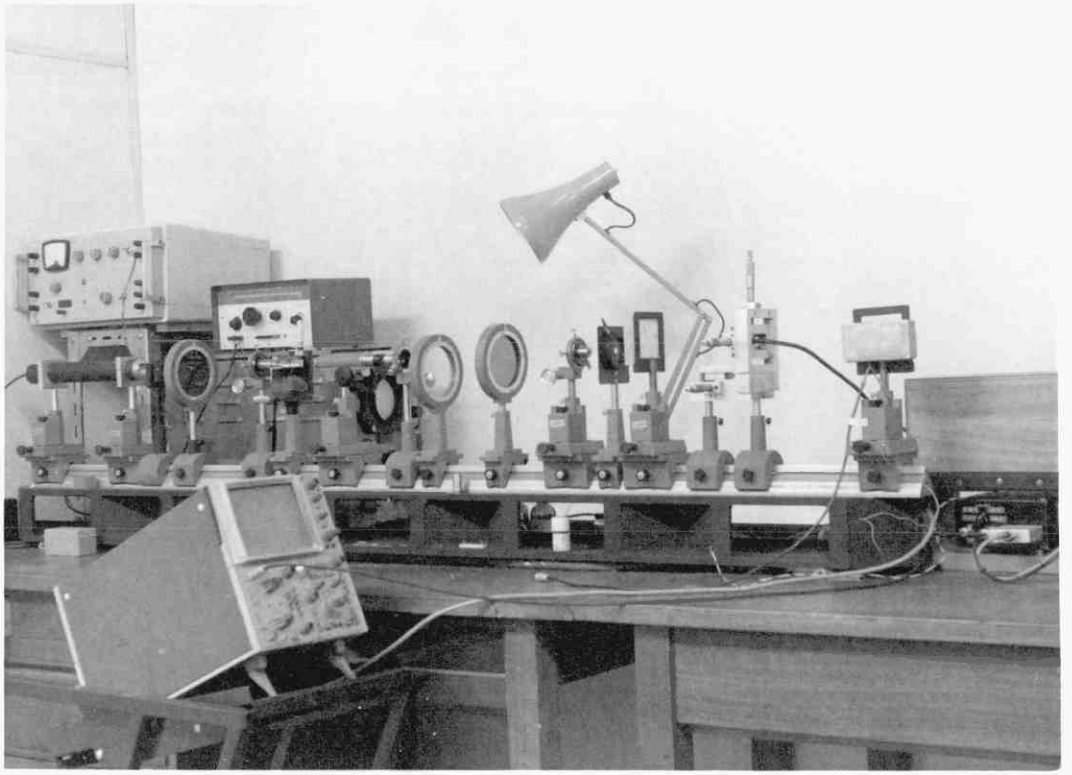

Fig.I.

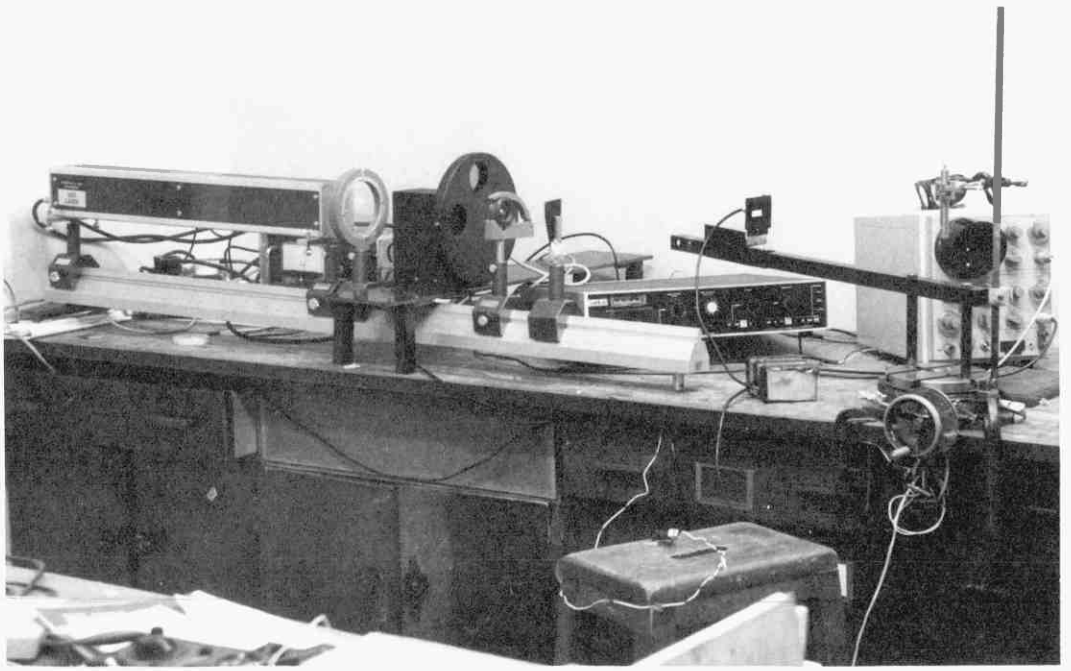

Fig.II.

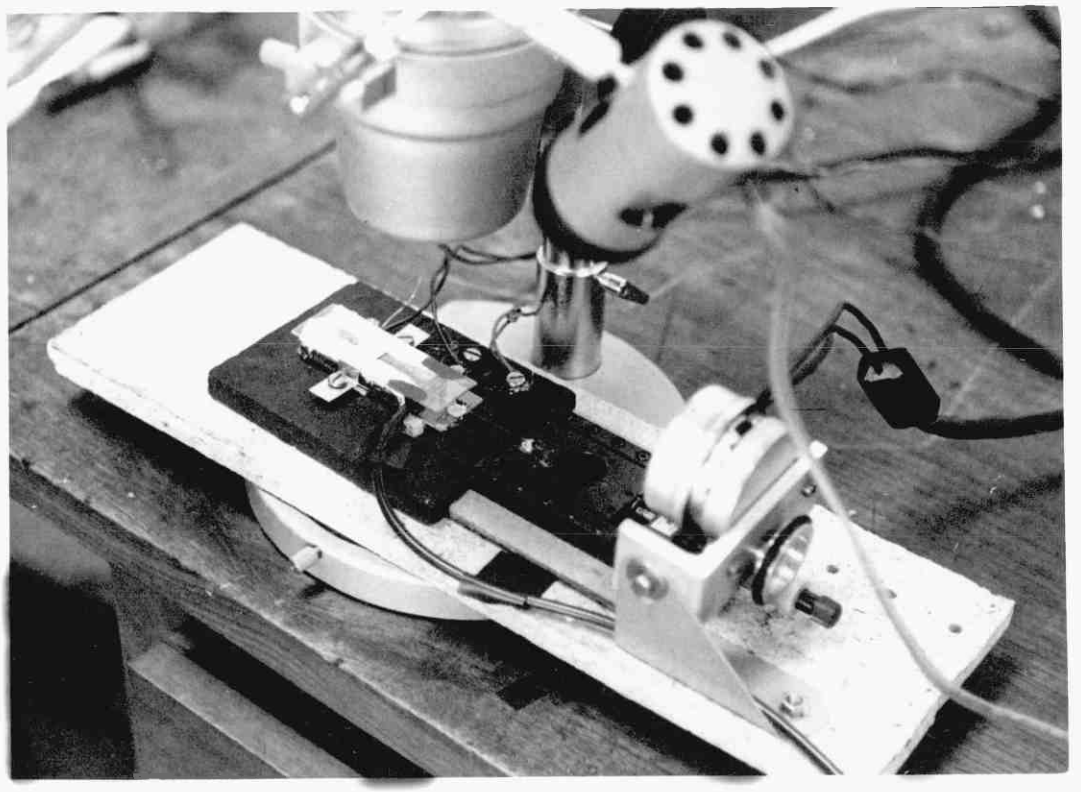

Fig. III(a)

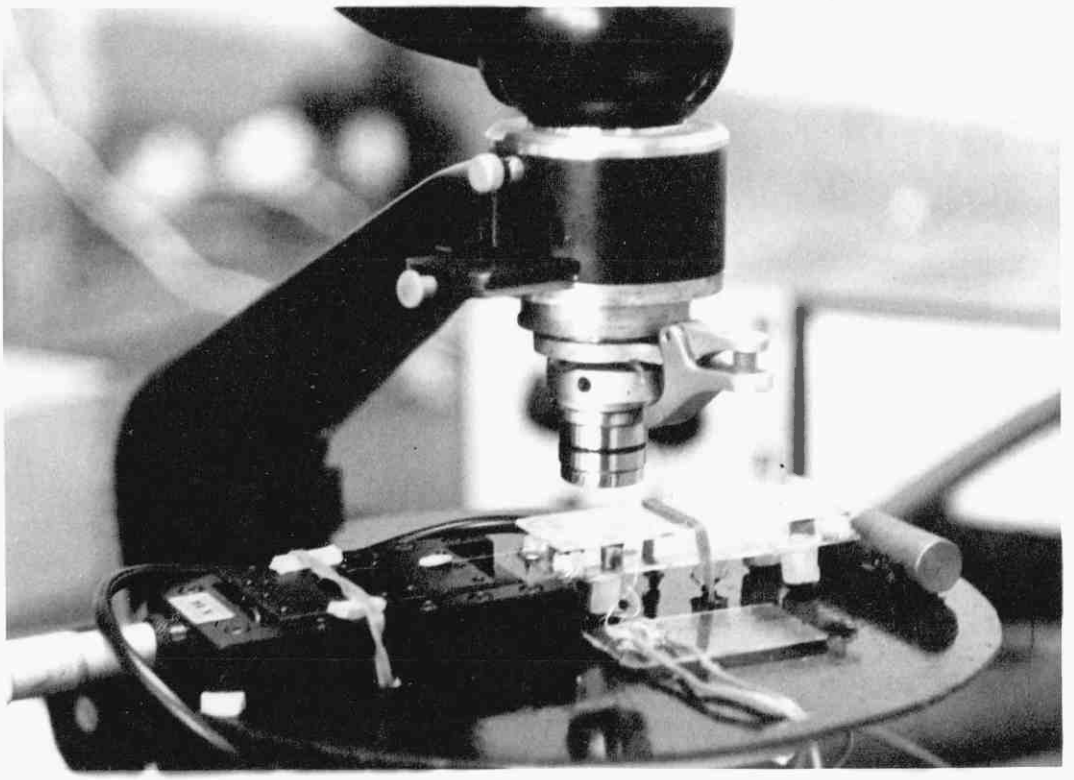

Fig. III(b)

JOURNAL OF MATERIALS SCIENCE 12 (1977) 869–872

Crystal growth of organic materials in glass capillaries

F. H. BABAI, R. B. DYOTT, E. A. D. WHITE
Department of Electrical Engineering, Imperial College, London, UK

Three potentially useful electro-optic organic materials have been grown as good optical quality single crystals of up to 30 mm length inside hollow glass fibres of 35 to 50 μm i.d. Capillary attraction was used to fill the fibres and a furnace with small cross-sectional area was designed for the recrystallization of the material inside. The crystallization process is fast and only 0.5 g purified material is needed, thus making the technique attractive for the rapid assessment of the electro-optic properties of many organic materials.

1. Introduction

Following the demonstration that organic crystals may have useful non-linear optical properties [1], the use of such materials crystallized in hollow glass fibres as active elements in a fibre waveguide system has been reported [2]. The technique of forming a single crystal within a fibre has many advantages not only for optical fibre devices, but also as a way of evaluating organic optical materials generally. For instance it is usually necessary to grow large quality crystals which have to be cut, lapped and polished in order to produce test specimens. Furthermore the crystallization of organic materials has not yet reached the stage of development of that for inorganic materials, and a great deal of time consuming effort is needed to find the optimum conditions for the growth of each substance. Hence a method whereby this aspect of the materials preparation is considerably simplified is of great interest.

To form a single crystal suitably oriented within a fibre, Stevenson and Dyott [2] used a controlled progressive freezing process analogous to Bridgeman growth. Whilst this was evidently successful for *m*-nitroaniline that they used in their experiments, we have found that other materials were less easily crystallized and concluded that a greater degree of control over the growth process was desirable. We report here on an improved apparatus which gives better control of crystal orientation and which has been used successfully in the preparation of crystals of materials found to be intractable by conventional methods.

2. Apparatus

2.1. Filling

The first problem in the growth of material in small-bore capillary tubes is in filling them with the liquid material. Two methods have been used which have given satisfactory results; in both cases capillary attraction was the primary driving force. In the preferred method a small quantity of the material (about 0.5 g) was placed at the bottom of a glass test tube and hollow fibres were introduced. The whole tube was heated in a furnace and the temperature carefully raised to the melting point when vertical filling automatically occurred. Alternatively the fibres were cemented into the perforated bottom of a small glass crucible which was filled and heated as in the previous method. In this case gravity assisted filling, although in practice it made little difference.

2.2. Recrystallization

Having filled the fibres it was necessary to recrystallize the material carefully in order to obtain single crystal regions of sufficient length for use in device studies and property measurments. Effectively growth was achieved by the Bridgman technique; that is, the material was first melted and then recrystallized progressively from one end by passing the fibre through a well defined temperature gradient such as that provided by the

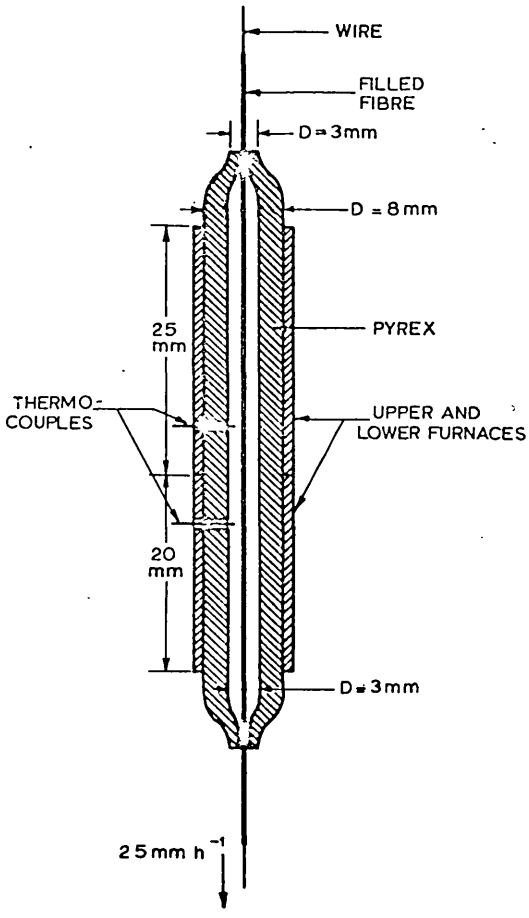

Figure 1 Apparatus for recrystallization of the filled fibres.

furnace shown in Fig. 1. The furnace had a small cross-sectional area and was made from a thick-walled glass tube pulled down at the ends to form a guide for the fibre at the entrance and exit. With symmetrical fibres of circular cross-section (see Fig. 2a) it was possible to produce single crystals about 1 mm long in materials such as *m*-dinitrobenzene. Using fibres of cross-section shown in Fig. 2b it was apparent that due to the variation in thermal capacity of the fibre cladding

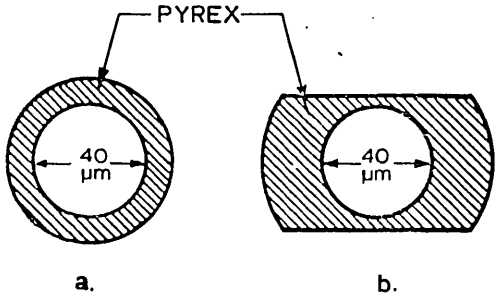

Figure 2 Cross-sectional view of the glass fibres used.

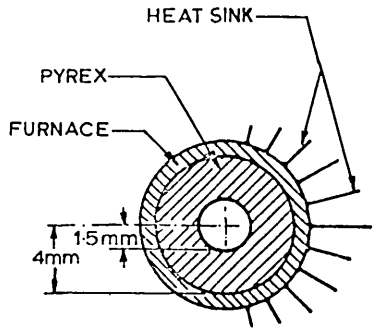

Figure 3 A modification in the furnace cross-section in order to provide a transverse temperature gradient.

in various directions, transverse temperature gradients were set up which helped to determine the alignment of the crystal in the cross-sectional plane, and hence the tendency to nucleate in a random manner was decreased. With this modification lengths (up to 30 mm) of single crystal were obtained which were long enough to be useful for experiments. However this technique was still not adequate for controlled growth, and the apparatus was further modified by the introduction of a transverse gradient in the furnace (see Fig. 3). In this way long lengths of single crystals were obtained in fibres with circular cross-section, which are preferred for some applications.

It has long been known that for materials which have a marked anisotropy in thermal conductivity, the direction of preferred growth for good quality crystallization is that in which the crystal direction of maximum thermal conductivity aligns with the direction of the steepest thermal gradient. If spontaneous nucleation is used to initiate the growth then the orientation of the crystal formed is usually in this preferred configuration (Fig. 4). It can be easily shown that since both the per-

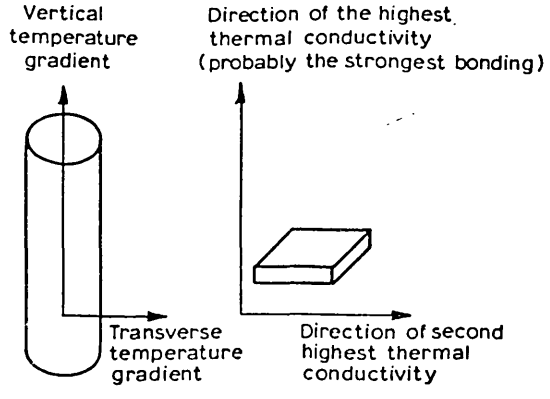

Figure 4 Schematic illustration of the crystal alignment with respect to the temperature gradients.

mitivity and the thermal conductivity can be described by second rank tensors, for crystals of orthorhombic or higher symmetry, one of the principal dielectric axes of the crystal will coincide with the direction of the highest thermal conductivity. Hence the material will crystallize with one of its principal dielectric axes aligned with the fibre axis. This condition has been achieved in the three materials grown to date.

3. Results

The results achieved with this improved furnace have been very encouraging and single crystal lengths up to 30 mm have been obtained for materials which some are known to be difficult to crystallize.

Crystallizations were carried out inside glass fibres of 35 to 50 μm bores and with effective growth rates of 25 to 50 mm h^{-1}. The results are summarized below.

3.1. *m*-Dinitrobenzene (*m*DNB)

This is one of five materials grown by Southgate and Hall [3] for non-linear optical studies on bulk single crystals. The optical quality of the samples of *m*DNB prepared by conventional methods are reported to be the poorest of the five and attempts by the authors to grow it from the melt have confirmed that it is difficult to grow as a good quality single crystal. It was chosen for fibre growth partly in order to obtain crystals of better optical quality by this technique and partly because of its suitability for making electro-optic fibre waveguide components. The material crystallized with the ⟨0 0 1⟩ direction parallel to the axis of the fibre. A section of the crystal-cored fibre is shown in Fig. 5, placed between crossed polarizers

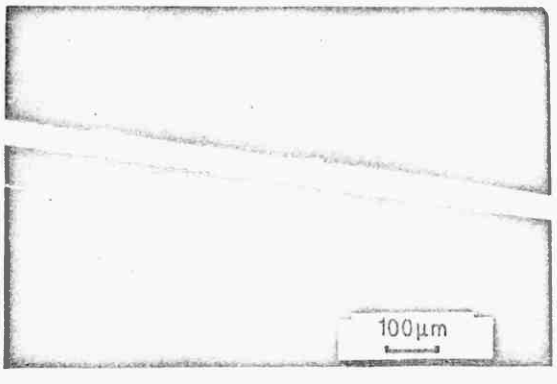

Figure 5 Crystal cored fibre between crossed polarizers, illuminated by white light.

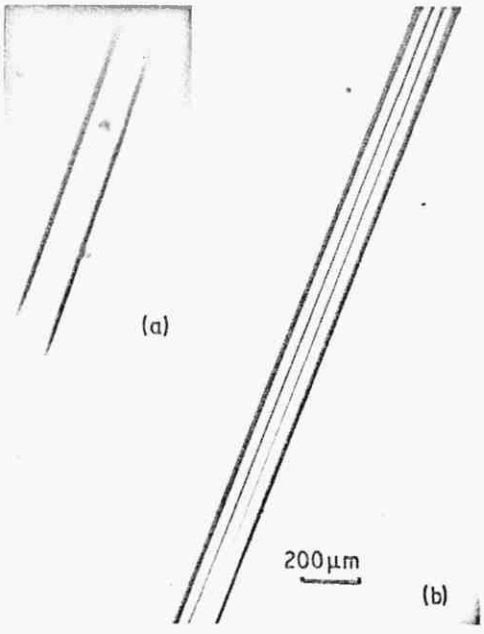

Figure 6 Fibre grown *m*DNB crystal illuminated by polarised light. The direction of polarization is (a) perpendicular to and (b) parallel with the fibre axis. A length of fibre containing a void is photographed in (b) to facilitate detection of the crystal core.

with the direction of polarization at 45° to the fibre axis and illuminated with white light. Complete extinction occurs when the light is polarized

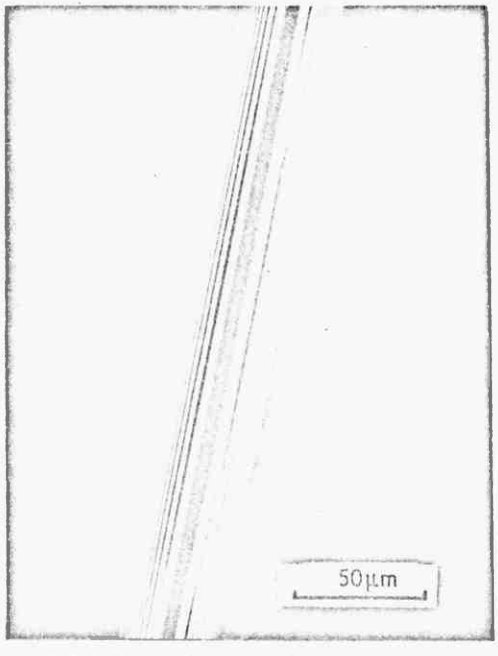

Figure 7 Birefringence of the fibre grown *m*DNB crystal at $\lambda = 589$ nm. The cladding is not visible in the photograph.

in a direction parallel to or perpendicular to the fibre axis. Fig. 6a and b show the crystal and cladding when illuminated by sodium light polarized parallel and perpendicular to the fibre axis, respectively. The principal refractive indices of *m*DNB at the sodium wavelength are: $n_x = 1.74$, $n_y = 1.71$ and $n_z = 1.49$, where as the refractive index of the cladding glass at this wavelength is $n_c = 1.478$. When the direction of polarization is parallel to the ⟨0 0 1⟩ direction of the crystal the contrast between core and cladding is lower than with other polarization directions. The birefringence of the crystal is shown in Fig. 7 using sodium light and a higher magnification. This also indicates the good optical quality of the crystals obtained.

3.2. 2-Bromo 4-nitroaniline

This material was also studied by Southgate and Hall [3]. Using the technique described above results similar to those for *m*DNB were obtained. It also crystallized so that one of its principal dielectric axes was aligned with the fibre axis.

3.3. Formyl-nitrophenyl hydrazine (FNPH)

This material has been studied by Owen and White [4], who report that it was difficult to crystallize by conventional methods due to its gradual decomposition either in solution or in the melt. However, crystallization is much faster with the fibre technique, and the material is also totally enclosed so that decomposition is less likely to occur. Although work on FNPH is in its earlier stages, short lengths of crystal of about 1 mm have been obtained. Again one of the principal dielectric orientations lies along the fibre axis.

4. Discussion

The method of preparation of single crystals in fibres has proved to be effective for a number of materials which are otherwise difficult to crystallize. The crystals within the fibres are in a convenient form for X-ray and optical examination, and also for evaluation of their performance in optical devices, e.g. by the determination of their electro-optic coefficients. The method also provides a means of preparing specimens for rapidly assessing new organic materials for optical activity without the need for elaborate and time consuming growth procedures. In addition, only comparatively small quantities of purified materials are needed, which can be an advantage for materials which are expensive or difficult to synthesize.

Acknowledgements

The authors would like to thank Dr J. R. Cozens, Dr J. L. Stevenson and Mr J. D. C. Wood for useful discussions during the course of this work.

References

1. B. L. DAVYDOV *et al.*, *Sov. Phys. J.E.T.P. Letters* **12** (1970) 16.
2. J. L. STEVENSON and R. B. DYOTT, *Electron. Letters* **10** (1974) 449.
3. P. D. SOUTHGATE and D. S. HALL, *J. Appl. Phys.* **43** (1972) 2765.
4. J. R. OWEN and E. A. D. WHITE, *J. Mater. Sci.* **11** (1976) 2165.

Received 2 September and accepted 4 October 1976.